Rochester Institute of Technology
RIT Digital Institutional Repository

Theses

12-19-2018

Development and Characterization of Novel III-V Materials for High Efficiency Photovoltaics

Zachary Shible Bittner
zsb2199@rit.edu

Follow this and additional works at: https://repository.rit.edu/theses

Recommended Citation

Bittner, Zachary Shible, "Development and Characterization of Novel III-V Materials for High Efficiency Photovoltaics" (2018). Thesis. Rochester Institute of Technology. Accessed from

This Dissertation is brought to you for free and open access by the RIT Libraries. For more information, please contact repository@rit.edu.

R·I·T

Development and Characterization of Novel III-V Materials for High Efficiency Photovoltaics

by

Zachary Shible Bittner

A dissertation submitted in partial fulfillment of the requirements for the degree of Doctor of Philosophy in Microsystems Engineering

Microsystems Engineering Program
Kate Gleason College of Engineering

Rochester Institute of Technology
Rochester, New York

December 19, 2018

Development and Characterization of Novel III-V Materials for High Efficiency Photovoltaics
by
Zachary Shible Bittner

Committee Approval:

We, the undersigned committee members, certify that we have advised and/or supervised the candidate on the work described in this dissertation. We further certify that we have reviewed the dissertation manuscript and approve it in partial fulfillment of the requirements of the degree of Doctor of Philosophy in Microsystems Engineering.

Dr. Seth M. Hubbard Date
Professor, Physics

Dr. Ryne P. Raffaelle Date
Professor, Vice President for Research, Associate Provost

Dr. Karl Hirschman Date
Professor, Electrical and Microelectronic Engineering

Dr. Parsian K. Mohseni, Date
Assistant Professor, Microsystems Engineering

Certified by:

Dr. Bruce Smith Date
Director, Department of Microsystems Engineering

ABSTRACT

Kate Gleason College of Engineering

Rochester Institute of Technology

Degree: Doctor of Philosophy **Program:** Microsystems Engineering

Author's Name: Zachary Shible Bittner

Advisor's Name: Dr. Seth M. Hubbard

Dissertation Title: Development and Characterization of Novel III-V Materials for High Efficiency Photovoltaics

Photovoltaics (PV) are an enabling technology in the field of aerospace, allowing satellites to operate far beyond the technological limitations of chemical batteries by providing a constant power source. However, launch costs and payload volume constraints result in a demand for the highest possible mass and volume specific power generation capability, a proxy for which is device power conversion efficiency. Enhancing the efficiency of III-V PV devices beyond the single-junction Shockley Queisser (SQ) limit has been a driving goal in PV development. Two competing loss mechanisms are thermalization, where photon energy in excess of the absorbing material's bandgap is lost to heat, and transmission or non-absorption, where a photon has too little energy to generate an electron-hole pair in the semiconductor. A further complication regarding the longevity of PV on satellites is damage due to exposure of high energy particle radiation limiting the operational life of the satellite via gradual degradation in efficiency.

In this work, two approaches to achieving higher power conversion efficiency are explored. The first, for devices at beginning of life, is towards the development of a prototype intermediate band solar cell (IBSC) where the spectrum is split into three optical transitions via the formation of an intermediate band between the conduction and valence bands of a wide bandgap host material. Towards this goal, an InAs/AlAsSb quantum dot solar cell (QDSC) capable of enabling sequential absorption is demonstrated via a two-step photon absorption measurement and photoreflectance is used to demonstrate the presence of intraband optical transitions. The second approach, focusing on power generation at end of life, utilizes multijunction photovoltaics where successively higher bandgap materials are stacked in series to optically split the solar spectrum to reduce both thermalization and transmission loss. The addition of InAs/GaAs QDs to a GaAs subcell and InGaAs strain balanced quantum well superlattices to inverted metamorphic multijunction (IMM) devices are explored in order to improve device current retention as material is damaged due to knock-on events displacing atoms from the crystalline lattice. A third section of this work focuses on reducing costs by demonstrating a model for performance of III-V devices grown on polycrystalline virtual substrates considering two

primary extended defects: the effects of crystal grain boundaries and the effects of antiphase boundaries induced by growing polar III-V materials on nonpolar Ge substrates.

Acknowledgments

I'd first like to thank Dr. Seth Hubbard for giving me the opportunity to work in his lab, first as an undergraduate struggling to find a co-op, and then continuing to support me through both a Masters and Doctoral programs. His office door was always open and he was always willing to discuss a problem or step into the lab to provide advice. I'm also grateful for his friendship over the past eight years. I'd also like to acknowledge the guidance of Dr. David Forbes, from whom I learned much about MOCVD and whose guidance was critical my early graduate career.

I'd also like to thank three of my early mentors. First, Dr. Christopher Bailey who got me engaged in the science behind the devices I was processing as a co-op, and then as my housemate in Cleveland while we were both working at NASA Glenn Research Center. Next, I'd like to thank Chelsea Mackos for teaching me about device processing and helping to create a sense of community within the group. Next, I'd like to thank Dr. Stephen Polly for his many years of friendship, many cups of coffee, and for teaching me most of what I know about test engineering.

To the rest of the NanoPV lab, Dr. Michael Slocum, Dr. Staffan Hellstroem, Dr. Brittany Smith, Dr. Yushuai Dai, George Nelson, and Elisabeth McClure for all your help with various projects, many fruitful discussions, and for being there to act as sounding boards for presentations, hare-brained hypotheses and many terrible jokes and puns.

Finally, I'd like to dedicate this work to my parents, Karen Shible and Stephen Bittner, for all their love and support throughout the years, and for encouraging me to follow my dreams and ambitions.

This work was funded in part by the US Department of Energy (grant: DE-EE0005325), The US Air Force Research Labs (grant: FA9453-08-C-0172), The US National Aeronautics and Space Administration (grant: NNX15CC20C), The US Office of Naval Research (grant: N00173-14-1-G011), and the National Science Foundation & Japan Society for Promotion of Science East Asia Pacific Summer Institute program.

Contents

ABSTRACT . . . . **iii**

Acknowledgments . . . . **v**

Contents . . . . **vi**

List of Tables . . . . **viii**

List of Figures . . . . **ix**

1 Introduction **1**

1.1 Motivation 1

1.2 Organization of Work 2

2 Background **4**

2.1 Solar Cell Operation and Efficiency Limits 4

2.2 Modeling Spectral Response 9

2.3 Basic Characterization techniques for Solar Cells 12

2.4 The Intermediate Band Solar Cell 16

2.5 The Multijunction Solar Cell 26

2.6 Radiation effects in QDSCs 29

3 Development of Quantum Dot Intermediate Band Solar Cells **36**

3.1 Introduction 36

3.2 Device Results 41

3.3 Probing Intermediate Transitions 45

3.3.1 Modulated Spectral Responsivity 45

3.3.2 Photoreflectance 47

3.4 Redesigned Device 49

3.4.1 Experimental 49

3.4.2 Results & Discussion 50

3.5 Conclusions 53

4 Development of Optimized QDSCs for Multijunction PV **54**

4.1 Introduction 54

4.2 Experimental 55

4.3 Results 56
4.4 QD Enhanced IMM Triple Junction Solar Cell 61
4.5 Radiation Tolerance of QD Enhanced Triple Junction Solar Cells 73
4.5.1 Modeling of Radiation Tolerance of IMM3J Solar Cells 73
4.5.2 Measurement of Radiation Tolerance of QD Enhanced IMM Triple Junction Solar Cells 77
4.6 Nanostructure Enhanced 1eV Subcell 83
4.6.1 Characterization of Test Structures and Simulation of Triple Junction Solar cells with MQW Enhanced 1 eV Subcell 83
4.6.2 Characterization of Nanostructure Enhanced 1eV Subcells 90
4.7 Conclusions 95

5 Modeling of Effects of Using Polycrystalline Substrates for Low Cost III-V Photovoltaics 97
5.1 Introduction 97
5.2 Experimental 98
5.3 Device Modeling 99
5.4 Results 102
5.5 Conclusions 108

6 Conclusions & Future Work 109
6.1 Development of Quantum Dot Intermediate Band Solar Cells 109
6.2 Development of Optimized QDSCs for Multijunction PV 113
6.3 Modeling of Effects of Using Polycrystalline Substrates for Low Cost III-V Photovoltaics 114

Bibliography 115

List of Tables

3.1 Devices included in study 41
3.2 Devices included in study 50

4.1 Devices included in study 56
4.2 Solar Cell AM0 IV Characteristics 57
4.3 Device diode characteristics. 58
4.4 Device diode characteristics. 65
4.5 Devices included in study 65
4.6 Modeled Triple Junction AM0 IV Characteristics 66

5.1 AM1.5G IV Characteristics of Devices Included in Study 104
5.2 Fit Material Parameters and Diode Characteristics of Devices Included in Study 104

List of Figures

2.1 Example diode IV curve with and without illumination (left) and example solar cell IV curve with example parameters. 5
2.2 Solar Cell equivalent circuit 6
2.3 AM0 and AM1.5G spectra compared to 6000K black body 7
2.4 Visualization of thermalization and transmission events in a solar cell. . . 8
2.5 Example detailed balance calculation made using a 6000K reference spectrum, separating out transmission and thermalization loss. 10
2.6 Diagram of TS Space Systems Solar Simulator at RIT. 13
2.7 Measured spectrum from RIT TS Space (TSS) Systems solar simulator and the ASTM AM0 reference spectrum for comparison. 14
2.8 Example EQE curve of a GaAs solar cell along with modeled carrier collection via minority carrier diffusion equations. 15
2.9 Example ideal intermediate band solar cell. 17
2.10 Detailed balance calculation for intermediate band solar cell performance under 1000x concentration under a 6000K black body spectrum with energy separation between intermediate and conduction bands on the x axis and energy separation between valence and intermediate band on y-axis. 18
2.11 Example AFM of InAs QDs grown on GaAs 20
2.12 1 sun AM0 J-V plots for baseline *pin* GaAs cell and two QD enhanced *pin* cells, one including GaP SC layer, and one without[19] 21
2.13 1 sun AM0 J-V plots comparing historic InAs/GaAs QDSC results from Veeco MOCVD reactor with InAs/GaAs QDSC results from RIT Aixtron MOCVD Reactor 22
2.14 Experimental setup at RIT for TSPA spectroscopy showing chopping of light from the broadband IR source. 24
2.15 Differential QE from an InAs/GaNAs strain compensated GaAs QDSC from Okada et al.[17] from two QE measurements, one with IR light bias, and one without. The shape mimics what is seen when two QE measurements are taken at different temperatures subtracted from on another. . . 25
2.16 Plot showing TSPA measurements performed by Antolin et al.[21]. (a) shows a standard photocurrent measurement (uncalibrated SR) of an InAs/GaAs QDSC at 80 K. (b) shows the TSPA measurement with chopped IR illumination at 6 K. (c) shows the TSPA measurement at 80 K, and (d) is the TSPA measurement with the IR source turned off, showing the noise floor of the measurement system from unchopped monochromatic illumination. 26

2.17 Chart of bandgaps and lattice constants of binary and ternary III-V semiconductors. . . . 28
2.18 Contour plot of efficiency of triple junction solar cell vs middle and top cell bandgaps on 0.64 eV bottom cell irradiated by a 5760 K black body as calculated by detail balance. . . . 29
2.19 Microlink Devices IMM blanket array wrapped around 1.3” diameter pipe. Image courtesy of Dr. Stephen Polly . . . 30
2.20 Diagram depicting atom displacement from radiation damage in zincblende lattice (not to scale). . . . 31
2.21 Plot of relative J_{SC} at BoL and EoL in a 4-junction IMM solar cell by Patel et al.[28] . . . 33
2.22 Spectral response vs wavelength for the reference (black circle), single QD layer (blue square), and 5x QD (red triangle) at (a) beginning-of-life, and (b) at $6.7x10^{11}$ $\frac{\alpha}{cm^2}$. (c) shows spectral response vs fluence at 830 nm and 910 nm corresponding to GaAs and InAs QD absorption peaks respectively. (d) shows average PL intensities of GaAs control and a 5-layer InAs QD sample vs fluence. [29] . . . 34
2.23 Potential energy of an Indium primary knock-on atom along $\langle 201 \rangle$ for a 1% compressive, relaxed, and 1% tensile-strained lattice, showing that the lattice under tensile strain has the lowest required energy for defect formation.[31] . . . 35

3.1 Band energy vs. lattice constant diagram showing relative offsets of conduction and valence bands of III-V materials when strained to the InP lattice constant. The conduction band positions are shown in black, while valence band positions are shown in blue. Strain that would be present if the material was strained to the InP lattice constant determines whether the light hole or heavy hole bands determine bandgap of the material. Generated by Dr. Staffan Hellstroem . . . 38
3.2 Result of 8-band $k \cdot p$ simulation of InAs/AlAsSb QD structure. E_v to E_{QD0} (red), E_{QD0} to E_X (yellow), E_{QD0} to Γ (blue), and $E_{QD,excited}$ to Γ (green) transitions are shown. . . . 39
3.3 Schematic of QDSC layer structure used in this study. . . . 40
3.4 Modeled EQE of various InAlAs control cell designs, varying the emitter thickness from 50nm to 200 nm . . . 40
3.5 AM1.5G JV of InAlAs control cell and InAlAs cell with 15x InAs/AlAsSb QD. . . . 42
3.6 Dark JV (solid line) and J_{SC}-V_{OC} (dashed line) of InAlAs control cell and InAlAs cell with 15x InAs/AlAsSb QD. . . . 43

3.7 Band diagram of nip InAlAs solar cell with and without AlAsSb uid region showing the electron barrier preventing the transport of photogenerated current through the diode. 43
3.8 EQE and EL of InAlAs Control cell and InAlAs cell with 15x InAs/AlAsSb QD. No ARC was applied 44
3.9 ΔSR (top) and conventional SR (bottom) measurements as a function of temperature. 46
3.10 Diagram of photoreflectance setup. 48
3.11 Photoreflectance spectrum of InAlAs device with InAs/AlAsSb QDs. Oscillators fitted to 0.720 eV, 1.307 eV, and 1.453 eV. 48
3.12 Band diagram of InAlAs solar cell with AlAsSb emitter and uid region showing the elimination of the electron barrier that prevented the transport of photogenerated current through the diode. 49
3.13 AM1.5G *IV* of the three devices included in this study. 51
3.14 Dark *IV* and $I_{SC} - V_{OC}$ measurements from devices with AlAsSb *uid* region. 51
3.15 External quantum efficiency measurements of InAlAs control cell, InAlAs cell with AlAsSb i-region, and AlAsSb emitter/intrinsic InAlAs solar cell. 52
3.16 TEM cross-section of AlAsSb grown on InP showing threading dislocations nucleating from the AlAsSb interface. 53

4.1 AM0 IV results for baseline, QD homojunction, and heterojunction emitter solar cells. 57
4.2 Solar Cell Jsc-Voc characteristics. Dotted lines represent control devices while solid lines represent the QDSCs. 58
4.3 Full EQE spectra of QD solar cells with sub-band collection shown in log scale. 60
4.4 Fitting of EQE spectrum of heterojunction solar cell using a modified Hovel model and Synopsis Sentaurus. 61
4.5 Fitting of EQE spectrum of heterojunction 10x QD solar cells using a modified Hovel model and Synopsis Sentaurus. QD collection is not included in this model 62
4.6 (224) reciprocal space map of $In_xGa_{1-x}As$ metamorphic buffer grown on GaAs taken on the RIT Bruker D8 Discover HRXRD 63
4.7 Detailed balance calculation showing maximum efficiency vs middle and bottom cell bandgaps with a fixed 1.9 eV top cell. 63
4.8 EQE results from inverted GaAs control cell(left) and GaAs/InAs QDSC(right). 64
4.9 Fitted EQE of GaAs/InAs QDSC ordered by base MCDL arranged from longest to shortest MCDL. 64
4.10 Diagrams of ‘thick emitter’ nip$^+$ and ‘thin emitter’ n$^+$ip designs. 65

4.11 IV simulations of conventionally designed middle cell and redesigned middle cell in triple junction IMM 66
4.12 Measured EQE curves for top, middle, and bottom subcells of triple junction devices. Conventional thin-emitter designed cells are shown in black while the thick-emitter design is shown in blue. 68
4.13 Measured EQE curves for middle subcells of triple junction devices comparing the relative change between the thin and thick emitter design and between control device and QDSC. Conventional thin-emitter designed cells are shown in black while the thick-emitter design is shown in blue. . 68
4.14 Measured AM0 JV curves for triple junction devices with and without InAs QDs in the GaAs subcell. Conventional thin-emitter designed cells are shown in black while the thick-emitter design is shown in blue. 69
4.15 Triple junction solar cell electroluminescence measured with ASD Fieldspec. The control cell EL spectrum is shown in black and 10x QDSC shown in red. An injection current density of 120 mA/cm^2 is shown in this figure. 70
4.16 Current-voltage characteristics of top, middle, and bottom subcells as well as of the full 3J device calculated from EL and EQE measurements. The black curve a dark-IV measurement used to calculate δV. The green diamonds are the sum of the three subcell voltages calculated from EL. . . . 71
4.17 IV characteristics of control and QDSC 3J devices derived from EL and EQE spectra. Control cell characteristics are shown in black and QDSC characteristics are shown in red. The inset shows a comparison between control and QD-containing GaAs subcells. 73
4.18 EL spectrum calculated from QE curve and reciprocity relationship. Measured EL in red, and calculated EL in black. 73
4.19 AM0 IV characteristics of 3J ELO IMM at BoL and EoL after 1MeV electron irradiation. 75
4.20 BoL experimental and simulated EQE characteristics of each subcell in 3J IMM solar cell. 75
4.21 EoL experimental and simulated EQE characteristics of each subcell in 3J IMM solar cell. 76
4.22 BoL 1-sun IV Characteristics of IMM 3J Control, 3J with 10xQD enhanced J2, and 3J with 20xQD enhanced J2. 77
4.23 BoL EQE Characteristics of IMM 3J Control, 3J with 10xQD enhanced J2, and 3J with 20xQD enhanced J2. 78
4.24 Remaining factors of Control, 10xQDSC, and 20xQDSC after irradiation with 1MeV electron beam. 80
4.25 EQE of all 3 junctions at a 1MeV electron fluence of 2.2x10^{10} MeV/g . . 81

4.26 J2 EQE characteristics at BoL and at increasing particle fluences for control cell, 10x QDSC, and 20x QDSC. 81
4.27 Remaining EQE vs DDD at 690nm (black), 830nm (red), and 940nm (blue) shown for control, 10xQDSC and 20xQDSC J2. 82
4.28 Reflectance, temperature, and curvature readbacks from growth of metamorphic QW superlattices. 84
4.29 Experimental photolumeniscence of 7nm $In_{0.4}Ga_{0.6}As$ QW in 9nm $In_{0.2}Ga_{0.8}As$ barrier grown on relaxed $In_{0.3}Ga_{0.7}As$ plotted along with absorption coefficient of QW calculated in NextNano. The inset shows the calculated band structure. 85
4.30 Optimized Control Cell, cell with QDs in J3, and cell with QWs in J3 resulting in best performance at a simulated $2x10^15$ e^-/cm^2 fluence. . . . 86
4.31 Simulated JV characteristics of 3J IMM solar cells with a modeled irradiation of $2x10^15$ e^-/cm^2. The control design is shown in black, a device containing QWs in the InGaAs subcell in red, and a device containing QDs in the InGaAs subcell in blue. 87
4.32 Simulated EoL EQE of 3J IMM solar cells with a modeled irradiation of $2x10^15$ e^-/cm^2. J1 is shown in black, J2 in red, and J3 in blue with dotted lines representing the control, long dashes representing the structure optimized for 40x QD layers in J3 and short dashes representing the structure optimized for 40x QW layers. 87
4.33 Optimized Control Cell, cell with QDs in J2, and cell with QDs in J2 and QWs in J3 resulting in best performance at a simulated $2x10^15$ e^-/cm^2 fluence. 88
4.34 EQE of Control cell design (black), optimized cell including 20x QD superlattice in J2 (blue), and optimized cell including 20xQD superlattice in J2 and 10 QW superlattice in J3 (green). BoL EQE is shown with dotted lines and EoL with solid lines. 89
4.35 Simulated triple junction J_{SC} for optimized control cell design, optimized design employing QDs in J2 only, and an optimized design employing QDs in J2 and QWs in J3. 90
4.36 Curvature, reflectance, and temperature readbacks from the growth of J3 isotypes showing minimal deflection changes during growth. Curvature is shown in black, reflectance in blue, and temperature in red. 91
4.37 Comparison of Light IV of Control and 40x MQW 1 eV inverted single junctions. 91
4.38 Measured and modeled EQE of 1eV inverted single junction with extracted minority carrier electron lifetime 92

4.39 EQE measured with a reverse bias in order to enhance electric field through MQW region of device (left) and relative CCE at 910 nm (emitter side) and 1210nm (base side) with varying applied reverse bias. 93
4.40 IV characteristics of full triple junction solar cell with 40x InGaAs QW enhanced 1eV subcell. 94
4.41 EQE of IMM triple junction solar cells. The black curve is the control device and blue is from the sample containing a 10X MQW superlattice in J3. Integrated subcell J_{SC} is labeled for each corresponding subcell. . . 94
4.42 Comparison between triple junction subcell and single junction 1 eV solar cell EQE. Control cells are in black and QW containing cells are in blue. Solid lines are single junction results and dotted lines are multijunction results. 95

5.1 Electroluminescence Images of GaAs solar cells grown on poly-GaAs substrates (left) and poly-Ge substrates (right) 102
5.2 Plot of experimental and modeled EQE of the solar cells grown on crystalline and polycrystalline GaAs and Ge substrates without an ARC. . . 103
5.3 Plot showing experimental one sun AM1.5G IV measurements (solid lines) and modeled results (dotted lines) for solar cells grown on crystalline and polycrystalline GaAs and Ge substrates. No ARC has been applied. . . . 105
5.4 <220> TEM of GaAs nucleation layer on c-Ge substrate showing the presence of APDs. The linear density shown results in an aerial density of 1.3-$3x10^9$ cm^{-2}. 106
5.5 One-sun AM1.5G efficiency contour plot showing expected device efficiency across a range of grain sizes and grain boundary recombination velocities with an APD density of 10^7. The two horizontal bands in the plot are the expected unpassivated grain boundary recombination velocities for GaAs. The star in the plot is placed at the predicted efficiency of the GaAs cell grown on poly-Ge if an ARC was applied. The slight difference from experimental was due to the lower than expected shunt resistance seen in the cell grown on poly-Ge. 107

Chapter 1

Introduction

1.1 Motivation

Early satellites relied upon chemical potential energy to operate, limiting the operational lifetime of the satellite to the energy stored in the included batteries which was restricted to the weight that could be feasibly launched. Vanguard I, the first artificial satellite to include solar cells, was launched on March 17, 1958. Due to lack of faith in the then untested photovoltaic technology, chemical batteries were included as the main power source of the satellite. The on-board batteries lasted nineteen days, but the Vanguard I continued operating on solar power [1] for six years. This paved the way for use of solar power in space. Due to weight and size constraints, PV is the only feasible method of generating power in space in sub-Jupiter solar distances. Modern satellites and space probes have similar weight constraints to previously launched, but much higher power demands, thus requiring higher efficiency PV and lead to interest in the development of high efficiency III-V solar cells for space power applications.

Many of the features that made Silicon favorable for the microelectronics industry are beneficial for photovoltaics. Si is abundant, inexpensive, and crystalline wafer manufacturing capacity and equipment has already been developed for microelectornics. Surface passivation, which is a challenge with many semiconductor materials, is easily solved with Si by growth of a surface oxide. While many III-V materials, such as Gallium Arsenide, possess direct bandgaps leading to near complete absorption of light right up to the band edge in a few micrometers of material, poor material quality lead to short minority carrier lifetimes, and passivating active materials. Epitaxy, or specifically heteroepitaxy,

pioneered by Herbert Kroemer[2] provided the keys to both material purity as well as device passivation required to grow high quality materials for PV.

Epitaxial growth of high-quality III-V semiconductors is generally constrained to materials sharing a lattice constant or layers with thicknesses below a critical thickness where defects begin to form, with some notable exceptions that are outside the scope of this work. The requirement of starting with a binary substrate such as GaP, GaAs, InP, or InAs limits the potential available bandgaps and bandgap combinations. Additionally, these substrate materials are extremely expensive which limits the commercial or economic viability of III-V photovoltaics. This work presents three approaches to improving solar cell efficiency and reducing cost by engineering materials or assessing the impact an engineered substrate would have on device performance.

1.2 Organization of Work

Chapter 3, is an investigation of the intermediate band solar cell (IBSC) concept where the spectrum is split across three optical transitions by adding an intermediate energy level within the bandgap of a host material. In this chapter, a prototype IBSC was demonstrated by embedding InAs QDs in AlAsSb barriers in an InAlAs solar cell. This work was published in Bittner et al.[3].

The goal of Chapter 4 is to improve triple junction device efficiency and radiation tolerance by incorporating QDs. Included is an investigation of optimal subcell design for incorporating InAs/GaAs QDs into a bandgap engineered middle junction for closely current matched triple-junction solar cells. The project began with a focus on optimum design for an upright triple junction solar cell grown on Ge, but multijunction PV technology has transitioned from upright monolithic designs grown on Ge to inverted metamorphic designs removed from the substrate via epitaxial lift-off.

Chapter 5 changes gears slightly and tries to address the high cost of III-V PV with the development of a model for device performance with high defect densities grown on polycrystalline virtual substrates. Part of this chapter is being prepared for submission

as my second peer reviewed first-author work as there is a natural breaking-point in the work.

A background on photovoltaic device operation and theory supporting these three chapters is collected in Chapter 2. Section 2.1 presents an overview of PV device operation and modeling while Section 2.3 provides an overview of general PV device characterization techniques that are relevant to all chapters. Section 2.4 supports Chapter 3 while Sections 2.5 and 2.6 support Chapter 4. Finally, future work is summarized in Chapter 6.

Chapter 2

Background

2.1 Solar Cell Operation and Efficiency Limits

The solar cell is fundamentally a diode, or a junction between a semiconductor with impurities in the atomic lattice that either give up an electron (donors) or grab an electron (acceptors). When light of photon energies greater than the bandgap of the material (E_g) illuminates the diode, an electron-hole pair is generated. When an injected minority carrier diffuses to the diode junction, charge separation occurs due to the built-in diode electric field. This leads to a light injected current (J_L). When the diode is held at short-circuit, the current collected is called the short-circuit current (J_{sc}). The diode IV curve is effectively shifted downward into the fourth quadrant by J_{sc} (Figure 2.1 left). For solar cells, this quadrant is called the "power quadrant" because it is the operation range where power is generated. It is traditionally flipped into the first quadrant to show that power is being generated as seen in Figure 2.1 on the right and is expressed using the ideal Shockley diode equation as

$$J = J_L - J_0(e^{\frac{qV}{nk_bT}} - 1) \tag{2.1}$$

As a forward bias is applied to the diode, diode forward operation current begins to balance out the photon induced current until a forward bias point is reached where the net current through the diode is 0. This voltage bias point is the open circuit voltage (V_{oc}). The point on the JV curve where the maximum power is generated is called P_{max}. These parameters are shown on the JV curve in Figure 2.1. Fill factor is calculated

from P_{max} with the equation

$$FF = \frac{P_{max}}{I_{sc} * V_{oc}} = \frac{I_m * V_m}{I_{sc} V_{oc}} \tag{2.2}$$

The solar cell power conversion efficiency (η) is the ratio of the maximum generated power P_{max} at a given illumination to the incident illumination power, or

$$\eta = \frac{P_{max}}{P_{in}} \tag{2.3}$$

where P_{in} is the total power illuminating the cell. In the case of solar cells, this is P_{sun}. The incident power will be discussed later in this chapter with solar spectra.

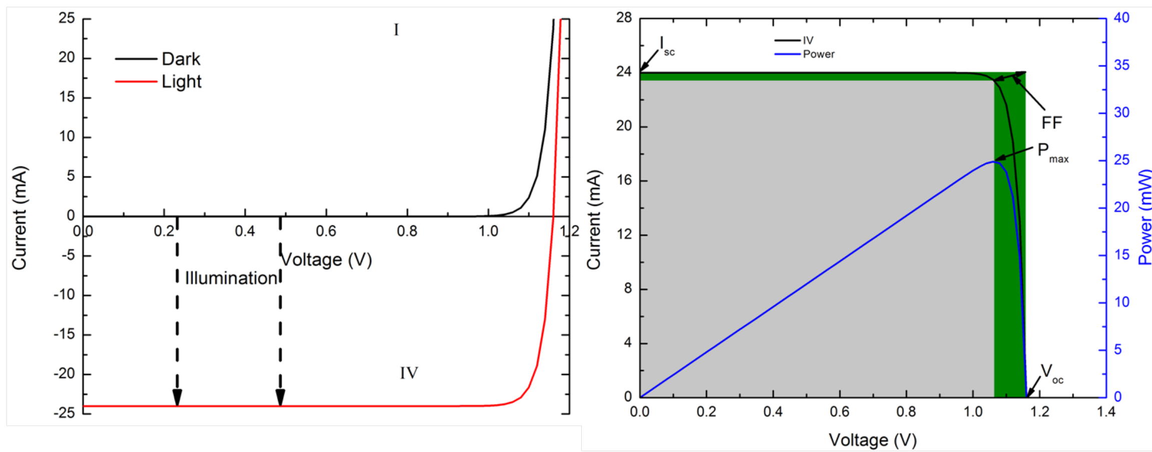

Figure 2.1: Example diode IV curve with and without illumination (left) and example solar cell IV curve with example parameters.

There are also two lumped parasitic resistance terms that are added to model resistance effects in the solar cell. The first being series resistance (R_s) which, true to the name, is shown as a resistor in series with the solar cell. Transport through the junction, lateral conduction in the solar cell emitter, conduction in the grid fingers and busbars of the cell, and metal-semiconductor contact resistances are included in this term. An ideal cell would have no series resistance. The second parasitic resistance term is the shunt resistance(R_{sh}), which characterizes the leakage current through the diode. The shunt resistance consists mostly of trap assisted tunneling across the diode. An ideal cell has an infinite shunt resistance. The series resistance is most pronounced when there is a

voltage drop across the two terminals of the cell and primarily reduces the magnitude of the slope around V_{oc}, while the shunt resistance is most pronounced at reverse bias, zero bias, or small forward biases and manifests as an increase in the magnitude of the slope around J_{sc}. Adding in the effects of parasitic resistances to the diode equation results in

$$J = J_L - J_0(e^{\frac{q(V-JR_s)}{nk_bT}} - 1) - \frac{V + JR_s}{R_{sh}} \tag{2.4}$$

Solving at $V = 0$ shows that with parasitic resistances, J_{sc} does not necessarily equal I_L as

$$J_{sc} = J_L - I_0e^{\frac{q(-JR_s)}{nk_bT}} - \frac{J_{sc}R_s}{R_{sh}} \tag{2.5}$$

where the exponential can be neglected due to the small magnitude resulting in

$$J_{sc} = J_L - J_{sc}\frac{R_s}{R_{sh}} \tag{2.6}$$

If the ratio of R_s to R_{sh} is not small, the effect on short circuit current can't be ignored. An equivalent circuit diagram is shown in figure 2.2.

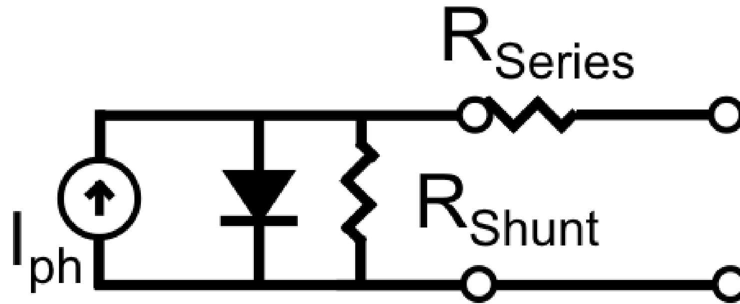

Figure 2.2: Solar Cell equivalent circuit

Photovoltaics are generally tested under a rigidly defined spectrum in order to be able to calculate an η for the target conditions of the device. In the case of solar cells, this spectrum is the solar spectrum. The sun is close in shape to a black body radiator with a temperature of $6000K$ and is often modeled as such. The precise solar spectrum measured from space is defined as Air Mass Zero ($AM0$) which has a total flux of 136.6 mW/cm^2. Since solar power has extensive terrestrial applications as well, a standardized spectrum

was chosen at $AM1.5G$, or the sun through 1.5 times the atmosphere thickness or at a corresponding zenith angle of 48.2^o and has a total flux of 100 mW/cm^2. There is general scattering of light in the visible range, and absorption dips due to specific molecules in the atmosphere such as H_2O and CO_2. These three spectra are shown for reference in Figure 2.3. The spectrum that a solar cell is designed to operate under is critical

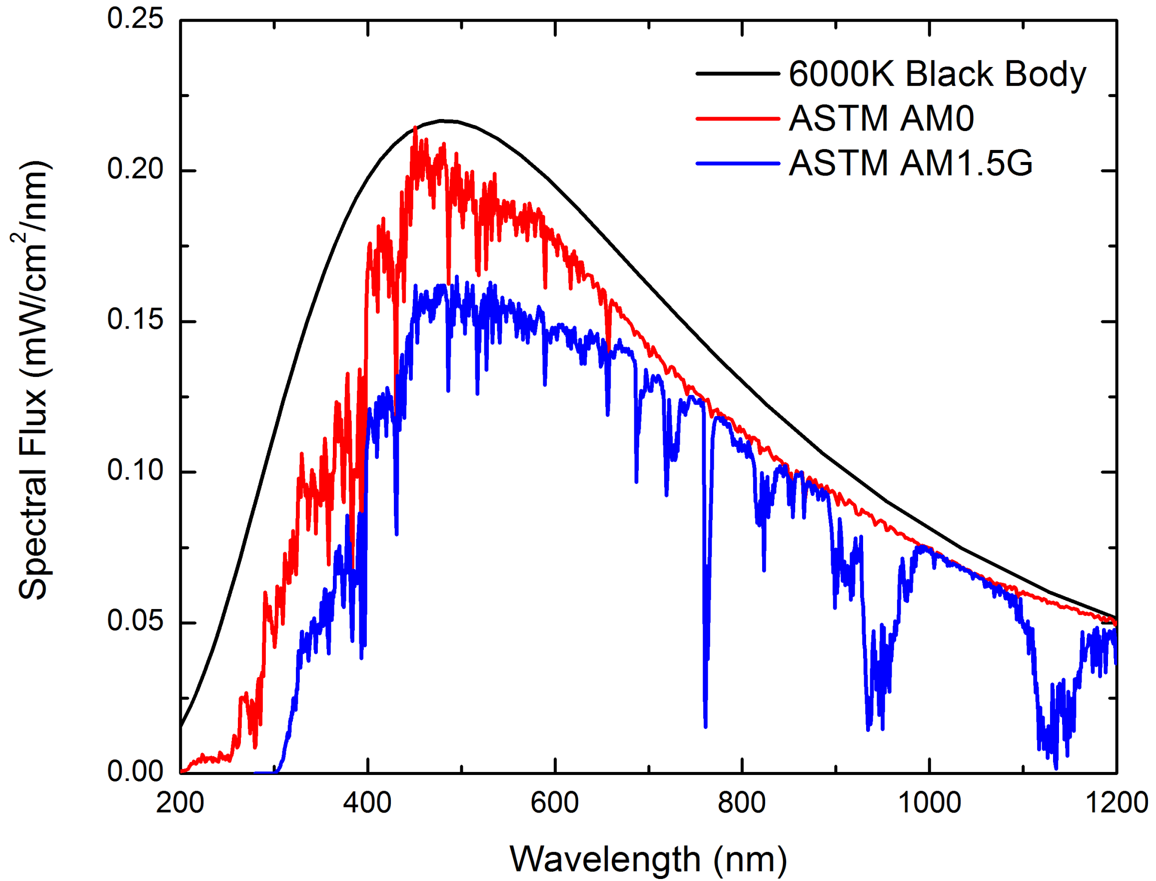

Figure 2.3: AM0 and AM1.5G spectra compared to 6000K black body

due to the major internal power loss mechanisms present in solar cells. The maximum thermodynamic, or Carnot, efficiency limit is given by the ratio of the temperatures of the two bodies involved[4].

$$\eta_{th} \leq 1 - \frac{T_{cell}}{T_{sun}} \tag{2.7}$$

where, as mentioned before, the sun is modeled as a $6000K$ black body radiator. Assuming the cell is operating at 25^oC, there is a maximum thermodynamic efficiency of 95%.

This value is not useful in determining maximum achievable solar cell efficiency because it ignores other power loss mechanisms which will be discussed in detail below.

Further power loss begins with transmission and thermalization. Photons with energies below the bandgap of the material can't be converted into electrical energy, while a photon with an energy above that of the bandgap can be absorbed. Assuming any photon that can generate a carrier does generate a carrier, there are further power loss mechanisms. Photons with energies above the bandgap of the semiconductor generate 'hot' carriers which relax down to the band-edge and the excess energy is lost to thermalization. Visualizations of these processes are shown in Figure 2.4.

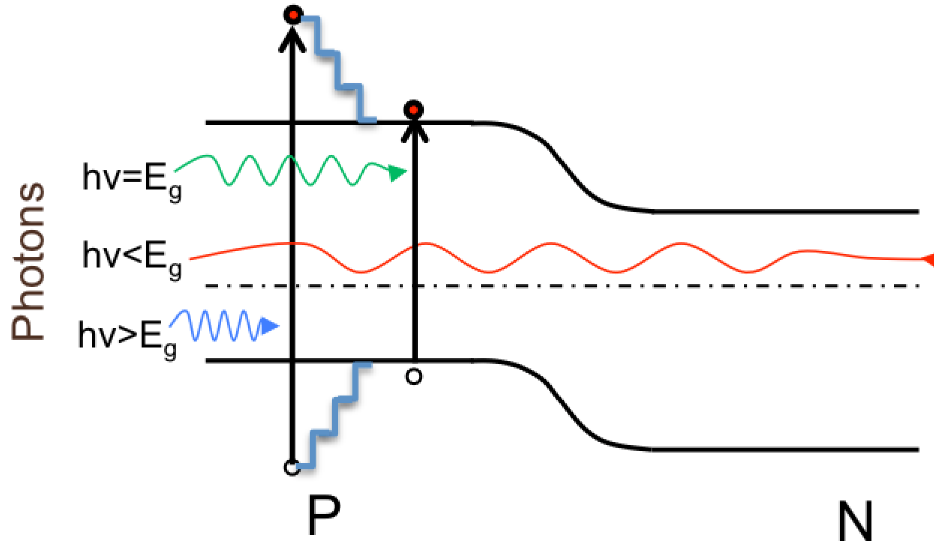

Figure 2.4: Visualization of thermalization and transmission events in a solar cell.

There is another power loss to entropy from the mismatch in absorption and emission angles. This is known as the Boltzmann loss. Both the Boltzmann and Carnot losses can be expressed as a reduction in optimal operating voltage[5]

$$V_{opt} = E_g \left(1 - \frac{T_{cell}}{T_{sun}}\right) - k_b T_{cell} \ln \left(\frac{\Omega_{emit}}{\Omega_{abs}}\right) \tag{2.8}$$

where Ω_{emit} is π, and Ω_{abs} is the solid angle of the Sun as seen from Earth, or $6.8 * 10^{-5}$ steradians[5]. Devices under high light concentration can outperform devices at an

equivalent one-sun illumination by reducing the Boltzmann loss through the increase in the effective absorption angle from the sun.

Finally, operating current can be calculated by subtracting the absorbed photon flux from the emitted photon flux at the the correct solid angle, defined, where flux, n, is

$$n(E, T, \mu, \Omega) = \frac{2\Omega}{c^2 h^2} \frac{E^2}{e^{\frac{E-\mu}{k_b T}} - 1} \tag{2.9}$$

where E is energy, c is the speed of light, h is Planck's constant, and μ is chemical potential and operating current is

$$J = e\left(\int_{E_g}^{\infty} n(E, T_{sun}, 0, \Omega abs)dE - \int_{q*V_{app}}^{\infty} n(E, T_{cell}, E_g, \Omega emit)dE\right) \tag{2.10}$$

and is based on Kirchoff's law of thermal radiation and is the difference between absorption and emission flux where V_{app} is the voltage applied to the cell. Rearranging to solve for solar cell power results in:

$$P_{SolarCell} = V_{app} * J(V_{app}) \tag{2.11}$$

Applying these power loss mechanisms as a function of bandgap results in the plot shown in Figure 2.5 It is clear from this model that at narrow bandgaps, the bulk of the power loss is due to thermalization, while with wide bandgap materials, the bulk of the power loss is due to transmission. The weaknesses of this model is that it assumes that the diffusion length is infinite, both the sun and cell are perfect radiators, any photon that can generate an electron-hole pair does so, and all recombination is radiative. The work in this study focuses primarily on the effects of thermalization and transmission for reasons that will be discussed later on [5].

2.2 Modeling Spectral Response

In reality, not every generated electron-hole pair results in collection. Devices are grown out of a material with a finite absorption coefficient and minority carrier lifetime.Bulk and surface recombination events and reflection loss result in lost potential current. The

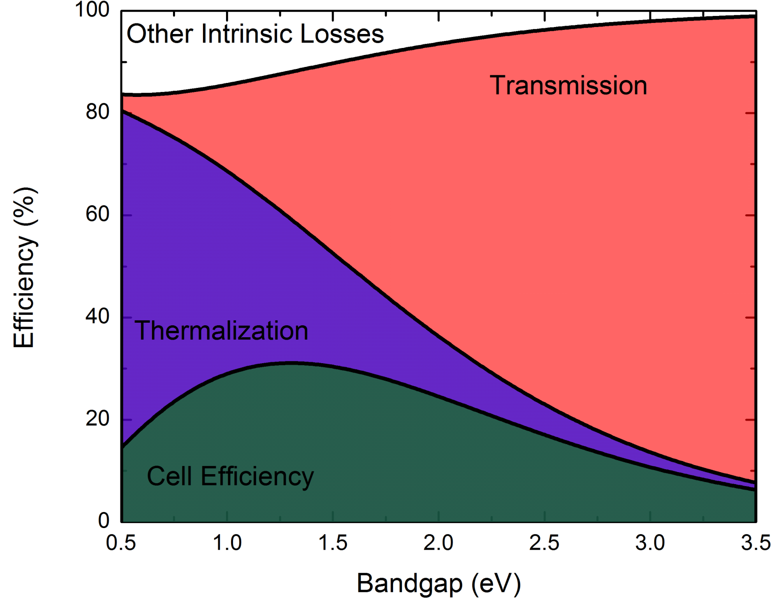

Figure 2.5: Example detailed balance calculation made using a $6000K$ reference spectrum, separating out transmission and thermalization loss.

ability to collect generated carriers, or the quantum efficiency of the device is an important metric in assessing both device design and material quality. This can be directly measured or modeled in terms of spectral responsivity (SR) which is defined as the amount of current (A) collected per unit power (W) illuminating the device at a given wavelength(λ). The Hovel/Woodall model[6] is a series of carrier transport equations that are the solution to the Poisson's equation for a diode. that can be used along with absorption data to model current collection in a device where a flux at a given wavelength (F), starting with current generated and collected in the front-surface field (FSF).

$$J_D = \frac{qF\beta L_a}{\beta^2 L_a^2 - 1}\left[\frac{\beta L_a + S_a \frac{\tau_a}{L_a}\left(1 - e^{-\beta D} cosh\frac{D}{L_a}\right) - e^{-\beta D} sinh\frac{D}{L_a}}{S_a \frac{\tau_a}{L_a} sinh\frac{D}{L_a} + cosh\frac{D}{L_a}} - \beta L_a e^{-\beta D}\right] \tag{2.12}$$

where β, D, L_a, τ_a S_a are the absorption coefficient, thickness, diffusion length, lifetime, and surface recombination velocity to air in the FSF material respectively. The next component, the emitter is modeled as

$$J_{D+d} = \frac{qFe^{-\beta D}\alpha L_g}{\alpha^2 L_g^2 - 1}\left[\frac{\alpha L_g + S_g \frac{\tau_g}{L_g}\left(1 - e^{-\alpha d} cosh\frac{d}{L_g}\right) - e^{-\alpha d} sinh\frac{d}{L_g}}{S_g \frac{\tau_g}{L_g} sinh\frac{g}{L_g} + cosh\frac{d}{L_g}} - \alpha L_g e^{-\alpha d}\right]$$

$$+\frac{J_D}{S_g\frac{\tau_g}{L_g}sinh\frac{g}{L_g}+cosh\frac{d}{L_g}} \tag{2.13}$$

where α, d, L_g, τ_g S_g are the absorption coefficient, thickness, diffusion length, lifetime, and surface recombination velocity to FSF in the emitter material respectively. Next, the space-charge, or depletion region of width W is modeled. The assumption here is that all generated carriers are collected because the drift field sweeps them out quickly.

$$J_W = qFe^{-\beta D}e^{-\alpha d}(1-e^{-\alpha W}) \tag{2.14}$$

Finally the contributions of the base are considered where

$$J_{D+d+w} = qFe^{-\beta D}e^{-\alpha d}e^{-\alpha W}L_p\frac{\alpha L_p}{\alpha L_p+1} \tag{2.15}$$

for a diode with a long base. The SR of the cell is given as

$$SR = \frac{J_{D+d}(\lambda)+J_W(\lambda)+J_{D+d+W}(\lambda)}{qF(\lambda)} \tag{2.16}$$

The value of such a model is that it allows for extraction of material quality parameters such as surface recombination velocities, minority carrier diffusion lengths, and minority carrier lifetimes when fitting to measured data or for the prediction of device performance using estimated or textbook parameters.

Finally, J_{sc} can be calculated from either measured SR data or an SR model by integrating across the spectrum where

$$J_{sc} = \int SR(\lambda) * \phi_{spectrum}(\lambda)d\lambda \tag{2.17}$$

where $\phi_{spectrum}(\lambda)$ is the desired spectrum that performance is to be measured under. The benefit of this technique is that it allows for the calculation of J_{sc} under any spectrum desired, without the concern of spectral mismatch from the lamps that would be used to simulate a spectrum. Generally, if the minority carrier diffusion length in a layer is at least twice as long as the layer is thick little current will be lost. The above model can be used to balance absorption via Beer-Lambert law and collection of minority carriers.

Minority carrier diffusion equations can also be used to more precisely estimate electrical characteristics of a solar cell. The diode reverse saturation current due to recombination in the quasi-neutral regions of the emitter and base

$$J_{p/n} = q\frac{D_{p/n}n_i^2}{N_{doping}L_{p/n}} \frac{sinh\frac{t-w_i}{L_{p/n}} + \frac{S*L_{p/n}}{D} * cosh\frac{t-w_i}{L_{p/n}}}{cosh\frac{t-w_i}{L_{p/n}} + \frac{S*L_{p/n}}{D_{p/n}} * sinh\frac{t-w_i}{L}} \tag{2.18}$$

Where $D_{p/n}$ is the diffusion constant for the minority carrier in the layer, S is the surface recombination velocity between the layer and corresponding window layer, $L_{p/n}$ is the minority carrier diffusion length, t is the film thickness, and w_i is the depletion width into the film. $J_{0,Diff}$ is the sum of J_p and J_n. Reverse saturation current due to recombination in the space-charge region can be modeled as

$$J_{0,SCR} = q\frac{n_i w_{i,emitter+base}}{(\tau_p \tau_n)^{1/2}} \tag{2.19}$$

where τ is the minority carrier lifetimes and w is the depletion width calculated from the built-in potential. Finally, the total diode current in the solar cell is given by

$$J = -J_{SC} + J_{0,Diff}(e^{q\frac{V-JR_s}{kT}} - 1) + J_{0,SCR}(e^{q\frac{V-JR_s}{2k_BT}} - 1) + \frac{V + JR_S}{R_{SH}} \tag{2.20}$$

where the diode ideality n=1 term comes from recombination in quasi-neutral regions of the diode and n=2 term comes from recombination in depletion regions of the device.

2.3 Basic Characterization techniques for Solar Cells

As we're interested in power generation, the first solar cell specific characterization technique employed is a one-sun illuminated IV measurement. For this measurement, the sample is placed on a temperature controlled chuck and illuminated with a light source calibrated to match the spectrum of interest. Figure 2.6 is a diagram of the solar simulator at RIT. It uses a hydrargyrum medium-arc iodide (HMI) lamp to generate the UV and visible portions of the solar spectrum and a quartz-tungsten halogen (QTH) lamp to generate the mid-IR through IR portion of the solar spectrum. Both lamp spectra are

shaped with permanent dielectric filters as well as optional AM1.5G simulating filters and the two spectra are mixed with a dichroic mirror. IV measurements are taken with source-measurement units (SMUs).

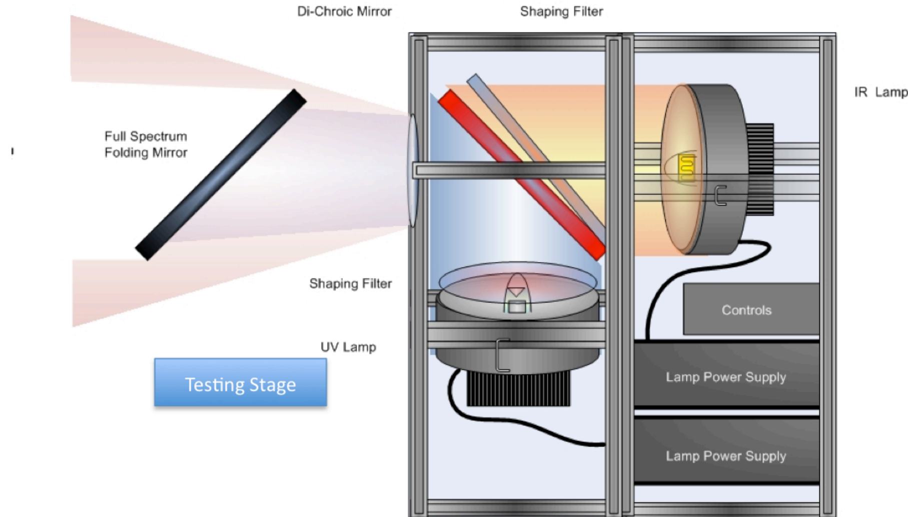

Figure 2.6: Diagram of TS Space Systems Solar Simulator at RIT.

Figure 2.7 shows the RIT AM0 spectrum along with the ASTM AM0 reference spectrum. The dip at 650 nm in the TSS spectrum corresponds with the crossover between HMI and QTH lamps. Both lamps need to be independently calibratable, so the crossover from the dichroic mirror is situated past the band edge of $InGaP_2$ which allows for calibration with an $InGaP_2$ reference cell, the standard top cell material in a III-V lattice matched triple junction solar cell. After the HMI lamp is calibrated, a GaAs reference cell is used to calibrate the QTH lamp.

Another important metric in PV characterization is external quantum efficiency (EQE), or the efficiency in which the solar cell converts photons of a specific wavelength into collected current. This is measured with a lamp coupled into a monochromator and calibrated against a detector with a known spectral responsivity (SR). The EQE measurement allows us to assess absorption and carrier escape properties in engineered materials containing quantum dots and quantum wells (discussed below) as well as estimate minority carrier diffusion lengths and lifetimes in bulk material using minority carrier

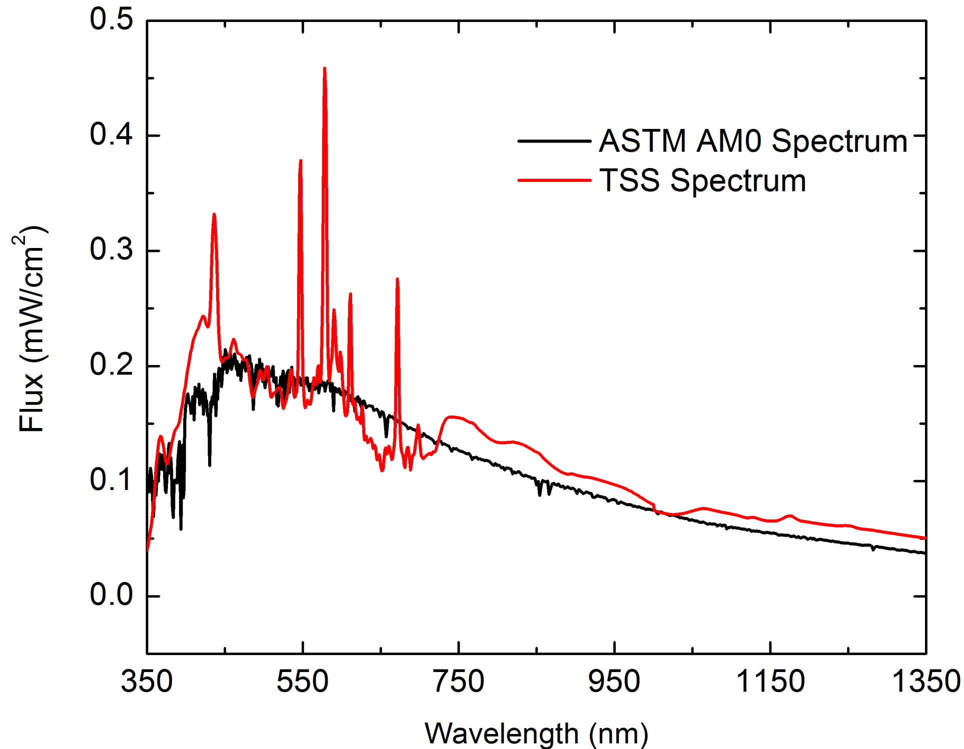

Figure 2.7: Measured spectrum from RIT TS Space (TSS) Systems solar simulator and the ASTM AM0 reference spectrum for comparison.

drift/diffusion equations shown in the section above along with measured indices of refraction and Hall mobilities. Figure 2.8 is a reference EQE curve of a GaAs solar cell along with the fit. Extracted minority carrier diffusion lengths will be discussed below in relevant sections.

Light emission can be as critical as light absorption in characterizing PV materials and devices. The first application is in determining the bandgap of ternary and quaternary alloys, relative intensity can provide information on material quality and the ratio of radiative to nonradiative recombination rates. Two methods of causing luminescence are used in this work. The first is photoluminescence (PL) where a minority carrier population is induced with a laser and the resulting emission from radiative recombination is measured with a monochromator and detector. This method can be used on as-grown epitaxial layers without requiring processing. The second method is electroluminescence (EL), where a fabricated solar cell is forward biased where minority carriers are injected

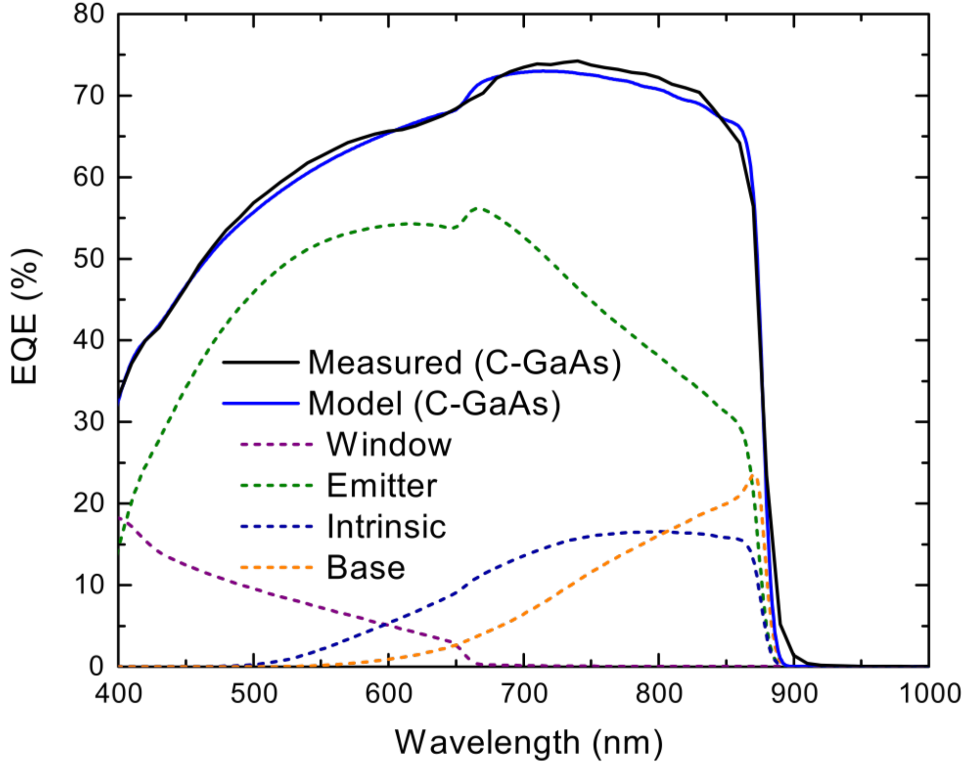

Figure 2.8: Example EQE curve of a GaAs solar cell along with modeled carrier collection via minority carrier diffusion equations.

across the junction. A calibrated injection current dependent EL measurement along with EQE measurements along with the reciprocity relationship between absorption and emission can be used to solve for the internal voltage of a solar cell [7] which can be used to either separate out the effects of series resistance, or in the case of multijunction solar cells, discussed below, can be used to extract subcell internal voltages.

Comparing emitted photon energy to V_{OC} is often used as a figure of merit to describe material quality. The figure-of-merit term W_{OC} is the difference between emission energy and V_{OC}, or[8]:

$$W_{OC} = \frac{E_{PL/EL}}{q} - V_{OC} \tag{2.21}$$

For bulk semiconductors, W_{OC} has been shown to be independent of bandgap and is related to the radiative efficiency of the solar cell[8]. A lower bound to W_OC is present in Detailed Balance as the power the cell radiates when applying V_max to Equation 2.10.

It is very weakly bandgap dependent and an ideal W_{OC}, as an approximation, is often expressed as 0.35 V[9] with typical values for high quality solar cells being around 0.4 V independent of material or bandgap[8].

2.4 The Intermediate Band Solar Cell

The intermediate band solar cell concept, much like the multijunction solar cell, still relies on a method of spectrum splitting. However, instead of physically splitting off to different materials, there is a virtual splitting by way of establishing multiple discrete energy levels in a single material. In the intermediate band solar cell, the highest energy transition is the bandgap of the host material. Controlled defects are introduced into the material where each defect creates an intermediate energy level within the bandgap. Electron wavefunctions in defect states, if spaced closely enough, will overlap forming an intermediate band, creating two new transitions, first from valence band to intermediate band, and from intermediate band to conduction band. The three level system reduces thermalization loss by allowing for the use of a wide bandgap host material, and then reduces transmission loss by having two lower energy transitions in the system. Collection requires either one high energy photon, or two lower energy photons, first to promote a carrier into the intermediate band from the valence band, and then from the intermediate band to the conduction band. A challenge is the relatively unlikely nature of two-step photon absorption processes which requires either extremely long carrier lifetimes or partial state filling in the intermediate band to provide a constant carrier population to promote from.

The first proposal was a defect band solar cell by Wolf *et al.*[10], but most defects behave as nonradiative recombination centers and are unable to contribute much to photocurrent[11]. The concept was revisited in 1997[12]. Luque *et al.*determined that with radiative recombination, a constant population in the intermediate band, and optical absorption driven escape from the intermediate band, it was possible to achieve a total power conversion efficiency of around 63% at full concentration under AM1.5G.[12]. The

example band structure, shown in Figure 2.9 is a nearly ideal case, with intermediate transitions of 0.7 eV and 1.23 eV and a 1.93 eV host material bandgap. This still leaves the challenge of introducing radiative "defect" states in order to establish the intermediate band.

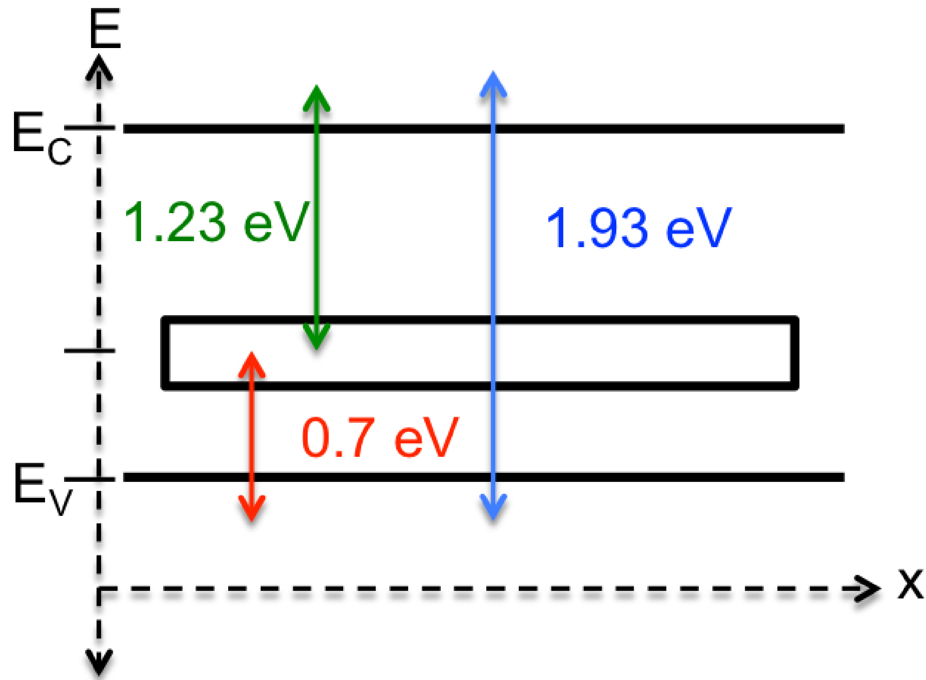

Figure 2.9: Example ideal intermediate band solar cell.

Figure 2.10 is a detailed balance calculation contour plot for an IBSC with arbitrary band separations between the intermediate and valence/conduction bands run under a 6000K black body spectrum at 1000x concentration. The host bandgap is the sum of E_{vi} and E_{ic}. Detailed balance assumes a single intermediate energy level with no absorption overlap. This calculation results in a max efficiency of 60% at $E_{vi} = 0.74\ eV$ and $E_{ic} = 1.27\ eV$ with a host bandgap of $2.01\ eV$.

Establishing intermediate states that are thermally isolated from both valence and conduction bands that don't act as nonradiative centers has been quite challenging. Au or Cu, for example, establish a state near midband in Si, but are entirely unsuitable for the purpose of engineering an IBSC because those defect levels promote nonradiative

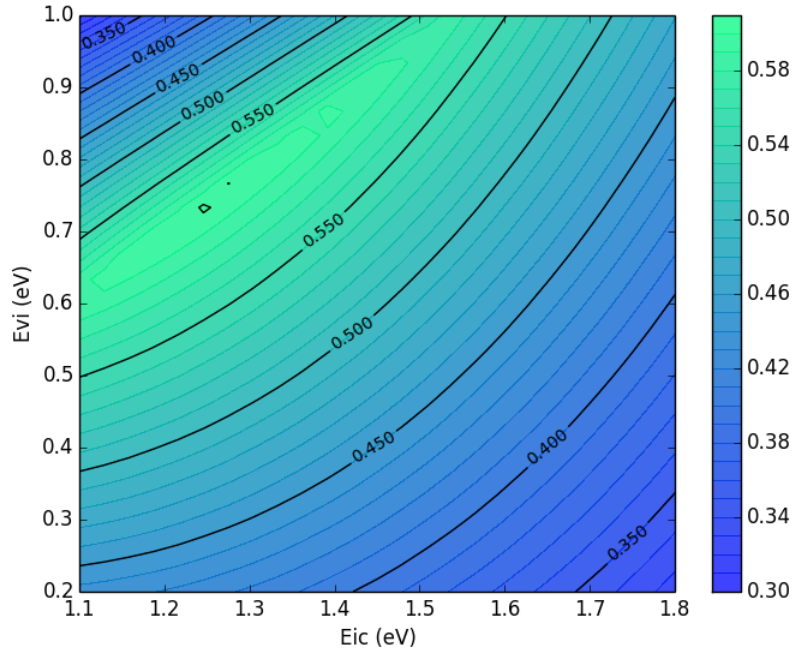

Figure 2.10: Detailed balance calculation for intermediate band solar cell performance under 1000x concentration under a 6000K black body spectrum with energy separation between intermediate and conduction bands on the x axis and energy separation between valence and intermediate band on y-axis.

recombination and lead to extremely poor solar cells[10]. Luque et al.[13] suggest that in order to suppress nonradiative recombination, a defect density above the Mott transition, the density allowing for wave function overlap between defect states and delocalization of carriers, is required to suppress nonradiative recombination.

One method of creating energy levels within a semiconductor without degrading the optical or luminescent properties is with semiconductor nanostructures; either quantum wells, quantum wires, or quantum dots for one dimensional, two dimensional, or three dimensional quantum confinement respectively. In any material with an energy level spacing that exceeds the thermal energy (k_BT), optical and electrical properties will exhibit a size dependence. The width of the bands, or the density of states, is dependent on degree of nearest-neighbor interactions in the material. Size dependence effects on electrical transitions in semiconductor nanocrystals occurs over much larger crystal sizes than in metallic nanocrystals due to the relatively strong nearest neighbor interactions

in semiconductors as compared to metallic bonding. The effective bandgap of a semiconductor cluster can show size dependent effects in crystals containing up to $10,000$ atoms[14]. The shape of the nanostructure plays an important role in the absorption spectrum. A bulk material has a bandgap and a continuum of states above and below the conduction and valence band respectively, resulting in broad spectral absorption up to the band edge. A quantum dot, with three dimensional confinement, behaves somewhat similarly to an atom, with discrete energy levels (similar to orbitals) as opposed to a continuum of states.

One proposed method of realizing the intermediate band is through the use of epitaxially grown quantum dots (QD)[15]. Quantum dots are a good choice because three dimensional quantum confinement leads to long radiative lifetimes and strong direct, polarization independent absorption. With proper material selection, it is possible to select materials with the correct potential barrier to prevent thermal escape

Another benefit of quantum dots, is that it is possible to grow high-density, high quality arrays of QDs on semiconductor substrates. Material deposition techniques such as metal organic chemical vapor deposition (MOCVD) and molecular beam epitaxy (MBE) are capable of precisely depositing crystalline semiconductor layers with thickness approaching single atomic layers. A thin, planar semiconductor film sharing a similar atomic spacing with and encapsulated by a wide bandgap host material results one-dimensional (z) confinement of carriers, leading to a quantum well. Selecting a highly lattice mismatched ($2\% - 10\%$) material for deposition allows for quantum dot nucleation via the Stranski-Krastanow growth mode, resulting in coherent nanoscale droplets on the surface, or QDs[16] with three-dimensional (x, y, z) quantum confinement. A pseudomorphic 'wetting-layer' first forms on the surface. After a critical thickness is reached, subsequent QD material begins to relax to the larger, preferred inter-atomic distance compared to that of the host template, and the material coalesces into droplets, or QDs. Eventually, a second critical thickness is reached, where larger defective dots begin to form. Previous work has focused on InAs QDs grown on GaAs, because the material system is well understood, so continued introduction of the QD IBSC concept will focus

on challenges seen in the InAs/GaAs material system.

InAs QDs formed on GaAs have diameters on the order of 25 nm and heights in the range of 2-3 nm. Characterization of density and size is generally performed via AFM on surface QDs. The AFM shown in Figure 2.11 is an example image showing densities on the order of $10^{10} cm^{-2}$.

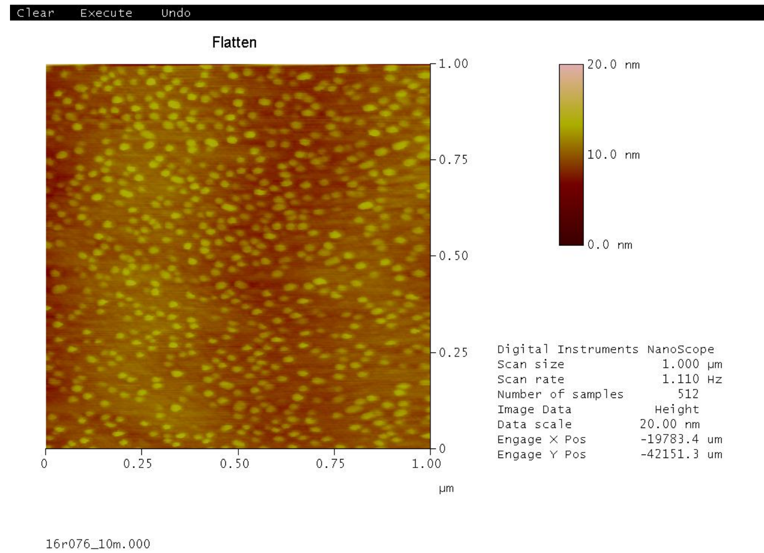

Figure 2.11: Example AFM of InAs QDs grown on GaAs

The QDs are placed in a unintentionally doped (*uid*) region between the emitter and base of the solar cell in order to minimize carrier capture via the presence of the cells built-in electric field. Even at open-circuit voltage, there is a slight field presence, hopefully allowing carriers generated in the emitter and base to be swept past the QDs uninhindered. Partial state-filling, a requirement mentioned above, can be accomplished by a few different methods. One common one is to introduce an n-type dopant near the QDs[17, 18]. The other is to illuminate the cell, optically generating a carrier population in the QDs. One challenge encountered with the QDSC is that of effective light absorption. A single layer of QDs may exhibit high volumetric absorption but the layer still only consists of, on average, less than 2-3 nm of material due to incomplete coverage and small QD heights. In order to enhance absorption, QDs are stacked in superlattice structures, however, as mentioned previously, the QD's form due to a compressive strain.

As additional QD layers are added, strain accumulates and results in a highly defective emitter, reducing both current collection and open circuit voltage. In order to avoid this, a tensilely strained GaP film can be added above each QD layer in order to compensate for the compressive strain. An example of this can be seen in Hubbard et al.[19] and is shown in Figure 2.12, where QDSCs with and without strain compensation (SC) layers are presented. The Baseline GaAs device has a J_{SC} of 23.6 mA/cm^2 and a V_{OC} of 1.02 V while the QDSC without SC achieves a J_{SC} of 18.7 mA/cm^2 and a V_{OC} of 0.51 V. Adding SC between QD layers allows for a net increase in J_{SC} to be measured from the current contribution of QDs and recovers V_{OC} to 830 mV.

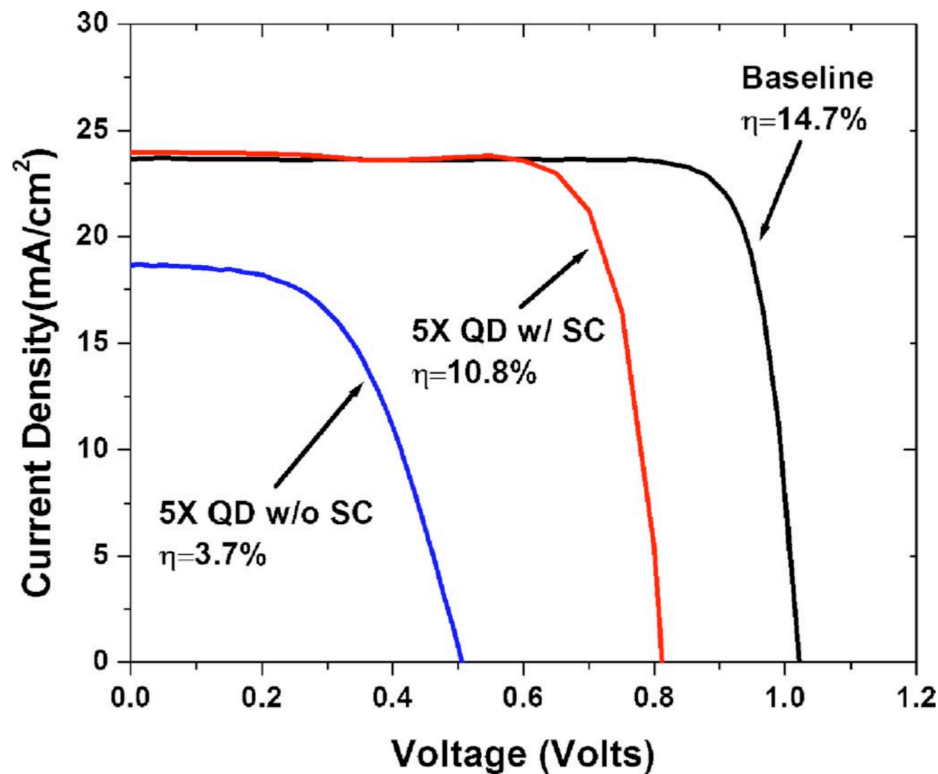

Figure 2.12: 1 sun AM0 J-V plots for baseline *pin* GaAs cell and two QD enhanced *pin* cells, one including GaP SC layer, and one without[19]

The QDSC in the above study still exhibited a drastic decrease in V_{OC} compared to the control cell. Bailey et al.[20] was able to demonstrate that open circuit voltage loss was a result of improper InAs coverage leading to large, optically inactive coalesced QDs

that behaved as recombination centers. The result of Bailey et al. was repeated on the Aixtron MOCVD at RIT, shown in Figure 2.13 suggesting the result, while non-trivial, is repeatable. Starting with the J-V curves in Figure2.13, both devices have near 1 V open-circuit voltages, closely comparable to that of a GaAs control cell. The RIT grown device exhibits a slightly higher J_{SC} and slightly lower fill factor. The J_{SC} increase is partly attributable to increased base collection due to longer lifetimes in RIT grown n-GaAs, but is mostly attributable to differences in calibration. Unfortunately the historic cell tested is no longer in condition for retesting because it was irradiated with alpha particles as part of a radiation study. Moving on to EQE, the characteristic InAs/GaAs QD response can be seen in the inset as current generation beyond the 880 nm band edge of GaAs.

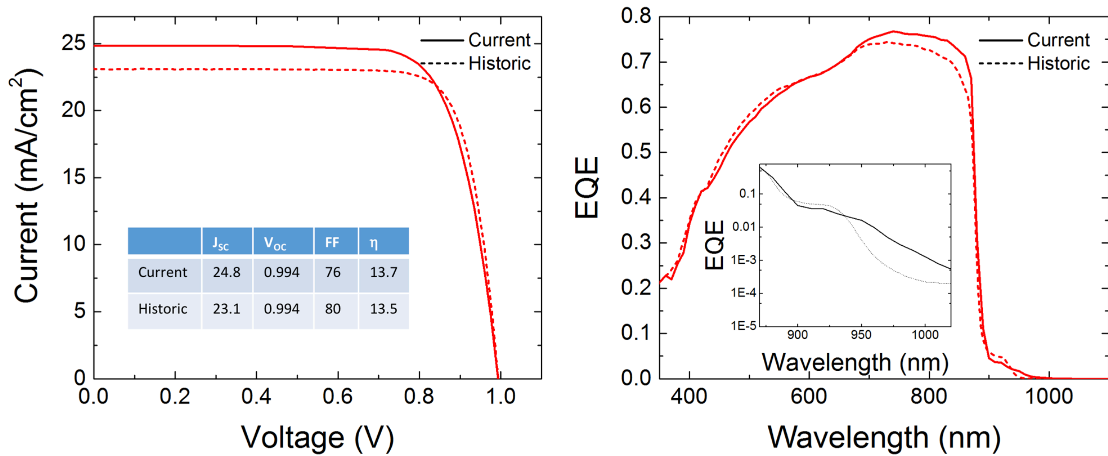

	J_{sc}	V_{oc}	FF	η
Current	24.8	0.994	76	13.7
Historic	23.1	0.994	80	13.5

Figure 2.13: 1 sun AM0 J-V plots comparing historic InAs/GaAs QDSC results from Veeco MOCVD reactor with InAs/GaAs QDSC results from RIT Aixtron MOCVD Reactor

There is one glaring issue with the EQE curve in Figure 2.13 as it relates to the IBSC. In order to achieve Fermi-level splitting, the intermediate state is supposed to be thermally isolated from the conduction band, meaning carrier collection requires the presence of a second photon. The collection shown in the EQE curve is driven from the 1.3 eV from valence band to QD state, and the shallow confinement in the conduction band of 0.12 eV is not adequate to suppress thermal escape[Yushuai Dai's soon to be submitted manuscript].If these devices were capable of exhibiting a two-photon

step conversion process, required for the IBSC, a single source SR setup would not be able to detect it. Two groups, one at the University of Madrid, and the other at the University of Tokyo[17, 21], pioneered a method to detect the presence and application of a sequential absorption event, sometimes referred to as two-step photon absorption (TSPA) spectroscopy.

Figure2.14 shows an example experimental setup designed to detect the presence of a state that allows for sequential absorption. Two light sources are employed. The first is a broadband, IR filtered light source, responsible for promoting carriers across the low-energy transition, in the case of InAs/GaAs QDs this would be from the QD to conduction band, and a monochromator with coupled lamp responsible for exciting carriers across the high energy transition. There are two methods of performing this measurement. The first is to perform a conventional SR measurement, where the monochromatic light is chopped and fed into the lock-in amplifier, both with and without the IR light bias, and subtract the two to extract a ΔSR. The second method is to disable the chopper attached to the monochromator and chop the IR light source, directly measuring ΔSR. The second method is the preferable option because it avoids issues with device temperature differences between two measurement that can occur with intense IR illumination as temperature is monitored on the cryostat stage, and not the sample itself.

Previous experiments we have performed using the former method have resulted in a ΔSR signal that looks like a subtraction of SR measurements taken at slightly different sample temperatures.

Okada et al. [17] employed InAs QDs on GaAs with GaNAs strain compensation layers and investigated the effects of Si doping to create a population in the carriers. Adding Si doping caused a PL blue shift from adding Si-doping which was not discussed in the paper, but also increased PL intensity by a factor of 1.7, which they attribute to defect state filling from the doping. When they looked at the Si-doped QD sample via TSPA spectroscopy, shown in Figure 2.15from Okada et al. [17], the results share similarities with what you'd see if taking the difference of two QDSC SR measurements at slightly different temperatures. As the band edge red-shifts, collection increases right

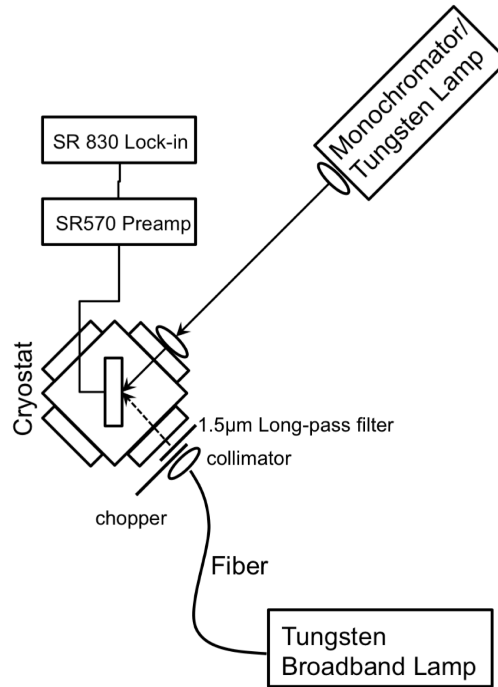

Figure 2.14: Experimental setup at RIT for TSPA spectroscopy showing chopping of light from the broadband IR source.

near the location of the lower temperature band edge, through the regions where the nanostructure absorbs, and abruptly ends at the absorption edge of the nanostructured region at the higher temperature. It also doesn't adequately address why the bulk of the change in QE occurs between 450 and 850 *nm*, and the explanation of the IR bias alleviating issues with carrier trapping in the QDs is at odds with the explanation of enhanced EQE in the case where Si doping is used to generate a carrier population. Light at 450nm has the lowest chance of generating a photon because carriers are generated near a surface where recombination is more likely. IR light biasing shouldn't effect that.

The TSPA spectroscopy technique with the IR light chopped was originally shown in 2008 by Antolin et al.[21] and included in Figure2.16. In this study, no strain compensation is employed, but the QDs are Si-doped. The QDs are in a flat-band area in a *pnin* structure which more closely resembles an IBSC, but can cause issues with carrier collection from the base of the cell. Curve (a) shows spectrally resolved photocurrent, or uncalibrated spectral response. A previous plot in the article shows EQE, but plots it

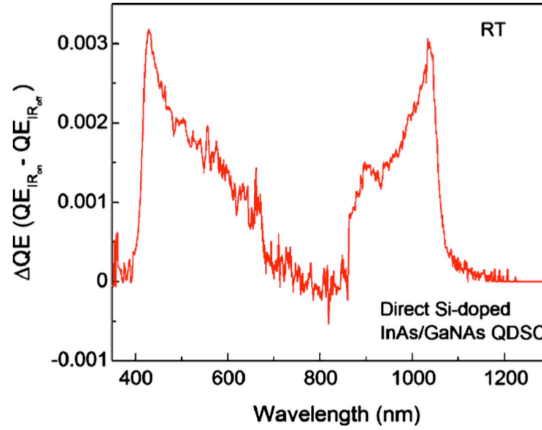

Figure 2.15: Differential QE from an InAs/GaNAs strain compensated GaAs QDSC from Okada et al.[17] from two QE measurements, one with IR light bias, and one without. The shape mimics what is seen when two QE measurements are taken at different temperatures subtracted from on another.

on log scale across six decades, hiding the poor bulk wavelength collection of the device. Moving curve (d), the noise floor measurement, there is some feature when the cell is illuminated with monochromatic light from 400 nm to 800 nm measured by the lock-in amplifier. There is DC current running through the system which can have the effect of increasing the noise floor and require a lower sensitivity setting from the lock-in. Moving onto curve (c), there is clear signal outside the noise floor across the entire spectrum of monochromatic illumination, probably caused by incomplete collection of the generated DC current due to carrier capture by the QDs. Any wavelength of monochromatic light establishes a population of carriers in the QD for the chopped IR illumination to excite but the greatest relative increase is at wavelengths that resonantly excite carriers into the QDs. Cooling the sample down to liquid He temperatures (curve (b)) further enhances this effect by increasing carrier lifetime in the QD and suppressing thermal escape. This example continues to be one of the most convincing examples of TSPA in literature.

Substantial work has gone into trying to establish partial state-filling in the InAs-GaAs QDSC material system at RIT in order to increase the probability of measuring two-step absorption processes[18], but we have not yet successfully measured this phenomenon in InAs/GaAs QDSC systems. Even at 20K, it is difficult to suppress carrier escape from

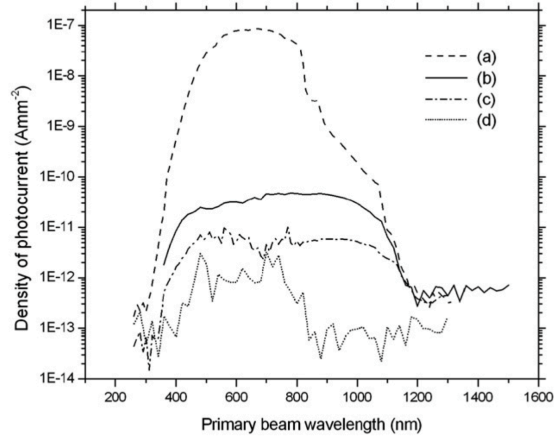

Figure 2.16: Plot showing TSPA measurements performed by Antolin et al.[21]. (a) shows a standard photocurrent measurement (uncalibrated SR) of an InAs/GaAs QDSC at 80 K. (b) shows the TSPA measurement with chopped IR illumination at 6 K. (c) shows the TSPA measurement at 80 K, and (d) is the TSPA measurement with the IR source turned off, showing the noise floor of the measurement system from unchopped monochromatic illumination.

QD to conduction band, and since photon flux is low near 10 μm from light sources we've used, absorption from QD state to conduction band requires promotion well above the conduction band (0.5+ eV) where the density of states is low. This thesis includes work on a material system I think is more suitable for the IBSC concept as it more closely matches the ideal energy levels.

2.5 The Multijunction Solar Cell

Most methods of "breaking" the Shockley-Queisser efficiency limit previously discussed involves splitting the solar spectrum up in some way in order to minimize efficiency losses due to thermalization and transmission. The conventional approach is the multijunction solar cell. Traditionally, the cell designer selects three or more materials with closely matched lattice constants but largely different bandgaps and grows subcells with each material onto a monolithic stack. The widest bandgap material is on top, and it transmits lower energy photons to the middle and bottom subcells. subcells are connected in series via tunnel junctions and the total current output is limited by the output of the lowest current producing cell, while voltages are additive. The two design objectives for a good

multijunction cell are to maximize the spectral coverage of the cell while keeping each subcell current matched.

Since the total output current of a triple junction solar cell is the amount of current produced by the subcell with the lowest J_{SC}, two of the subcells in a triple junction solar cell may operate in a region between the maximum power point and V_{OC} where excess photocurrent is injected across the junction. Through the reciprocity relationship, based on material quality, light may be re-emitted where it can either be reabsorbed by the same junction, a process called photon recycling[7], or transmitted to a subsequent junction in a process called luminescent coupling [22]. Luminescent coupling is limited by competition between radiative and nonradiative recombination processes so while it can improve current matching between subcells, it is not necessarily a substitute for current matching by managing absorption overlap between subcells.

The fundamental design challenge of the multijunction approach is that the starting lattice constant is somewhat constrained by substrate availability. Figure 2.17 shows the bandgap and lattice constant of common binary semiconductor materials along with ternary blends with appropriate bowing when applicable. Commonly available substrates are Si, Ge, GaAs, and InP.

Ge has been the primary substrate historically used for multijunction PV because it is possible to activate a p-type substrate as the bottom cell with an As diffusion step and with the 0.64 eV bandgap is reasonably suitable for the bottom cell. In0.01Ga0.99As is lattice matched and can be grown psuedomorphically along with $InGaP_2$. Figure 2.18 shows possible efficiencies achievable with a bottom cell matching the bandgap of Ge. Going back to Figure 2.17, the narrowest bandgap available for a lattice matched middle cell is 1.44 eV (GaAs), limiting the max efficiency of a triple junction Ge based multijunction cell to 31%.

Looking at Figure 2.18, it is apparent that if the bandgap of the middle cell can be lowered from 1.44 eV to around 1.2 eV, the maximum achievable efficiency goes from 31% to 47%. The problem with the GaAs/Ge based multijunction system is that no bulk materials with bandgaps lower than that of GaAs are available, so an engineered

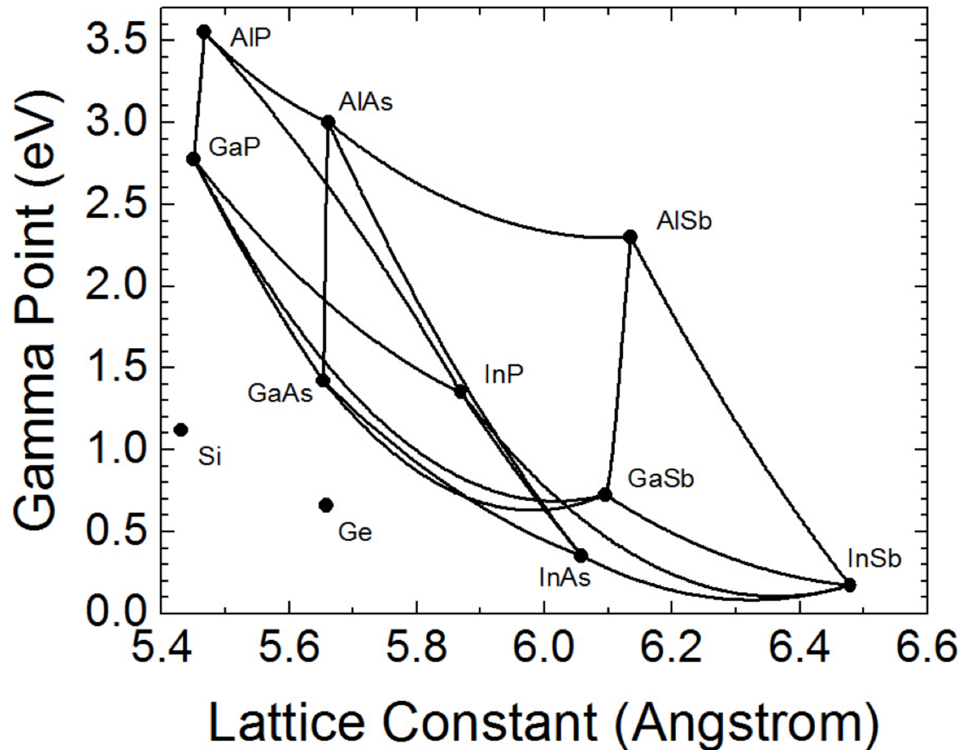

Figure 2.17: Chart of bandgaps and lattice constants of binary and ternary III-V semiconductors.

material is required. The previous section discussed the InAs/GaAs QD material system and some reasons why it may not be suitable for for IBSC applications, but the ease in which carriers are thermally excited out of the QD make InAs/GaAs QDs perfectly suitable as a method to engineer a reduction in the GaAs bandgap for the purposes of current balancing a middle subcell for a triple junction solar cell.

Growing multijunction solar cells on Ge has a few drawbacks. Due to the lack of a lattice-matched nitrogen-free material with a bandgap between GaAs or Ge, three junctions is the practical limit. Since the substrate is an active cell, there is no method allowing for removal of the solar cell from the substrate in order to reuse the substrate and reduce costs. Because of these limitations, NREL engineered an alternate triple junction scheme where the top then middle subcells are grown lattice matched to the substrate. In order to increase the V_{OC} of the cell, a bottom-cell bandgap of 1 eV can be employed. This is grown metamorphically. A transparent graded buffer of $In_{1-x}Ga_xP$ is grown to

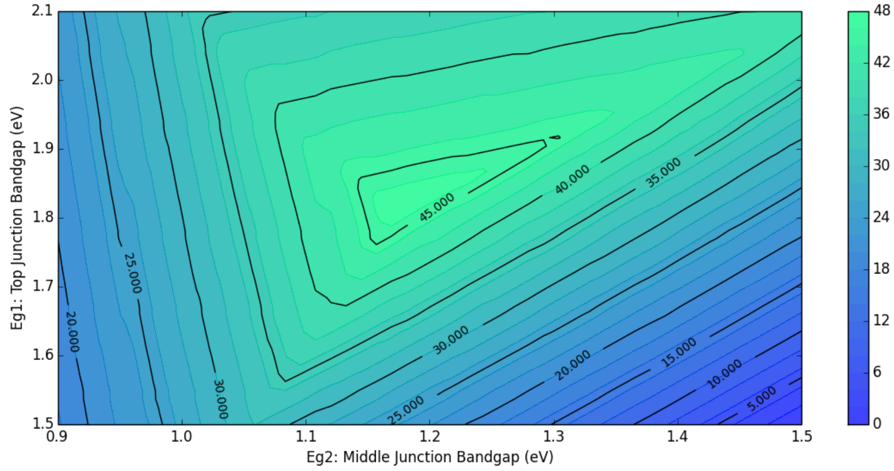

Figure 2.18: Contour plot of efficiency of triple junction solar cell vs middle and top cell bandgaps on 0.64 eV bottom cell irradiated by a 5760 K black body as calculated by detail balance.

grade the lattice constant from 5.66 to 5.76 allowing for the growth of relaxed $In_{0.3}Ga_{0.7}As$ with a bandgap around 1 eV[23]. These devices are grown on a substrate in an inverted manner where top and middle cells are grown first and second pseudomorphically on a GaAs substrate before the buffer layers and bottom cell. An etch stop or sacrificial layer is inserted between the substrate and the solar cell allowing for substrate removal. This design is known as the inverted metamorphic multijunction (IMM). An added benefit of the IMM design is the possibility of epitaxial lift-off (ELO) where the selectively etchable layer below the active solar cell layers is Al(Ga)As (with $> 70\%$ Al), which unlike the rest of the materials employed in the structure etches readily in HF. The ELO process has the benefit of preserving the substrate for subsequent growths[24], drastically reducing the cost. Figure 2.19 is an example of a flexible IMM array. The entire epitaxial film can be rolled without inducing cleaves or cracks.

2.6 Radiation effects in QDSCs

A major concern for the longevity of satellites in Medium Earth orbit (MEO), or orbital radii from 1.8 to 2.5 times the Earth's radius(R_e) is the high energy radiation effects,

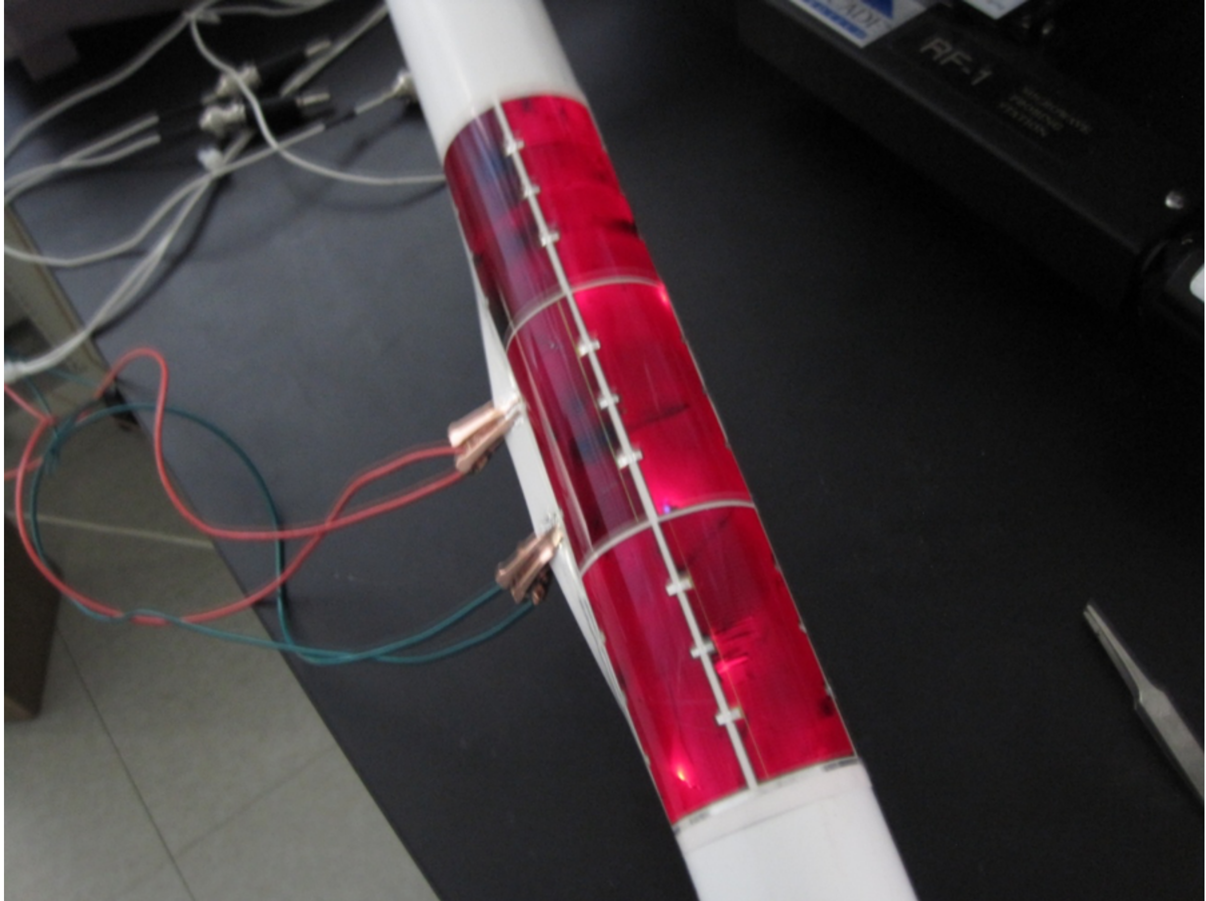

Figure 2.19: Microlink Devices IMM blanket array wrapped around 1.3” diameter pipe. Image courtesy of Dr. Stephen Polly

the main cause of solar cell degradation in space, from passing through the Van Allen belts where charge particles are trapped by the Earth’s magnetic field. Electron fluxes are as high as $9.4 * 10^9$ $e^-/cm^2/s$ and proton fluxes as high as $2 * 10^8$ $protons/cm^2/s$ are seen [25]. Incident particles collide with atoms in the crystalline lattice and lose energy through ionizing and non-ionizing interactions. Additionally, at lower fluxes is a presence of an assortment of trapped ions, mainly α particles and O^+. An α particle is a high energy helium nucleus (two protons and two neutrons). While radiation tolerance of bulk semiconductor materials is well understood[26], radiation tolerance of bandgap engineered materials using QDs or QWs, discussed in Chapter 1, is not well understood.

Ionizing energy loss occurs when a particle collides with a bound electron. The collision knocks the electron out of position, ionizing the atom it surrounded. This does

not permanently damage the device because another electron can be captured, annihilating the trapped charge. Cell degradation is caused by non-ionizing energy loss (NIEL) events where the high energy particle collides with an atomic nucleus. The primary knock-on (PKO) atom is displaced if the energy absorbed from the collision is enough to break the chemical bonds and force the atom out of position, generating a vacancy and, when it stops moving, resting in an interstitial site in the lattice. The generated vacancy/interstitial defect pair is known as a Frenkel defect. If the PKO atom absorbs enough energy, it can generate secondary vacancies. Most of the damage to displacements is concentrated near the stopping range of the particle. An example of an atomic displacement is shown in Figure 2.20 which is a depiction of a zincblende lattice.

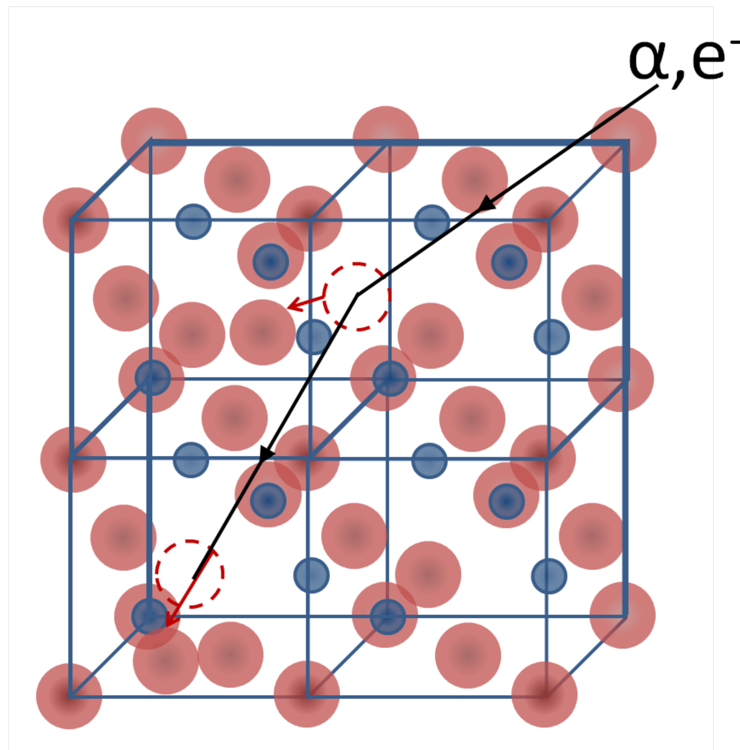

Figure 2.20: Diagram depicting atom displacement from radiation damage in zincblende lattice (not to scale).

In general, around 99% of the energy lost by a particle is to ionization[27]. The atomic diameter is on the order of 1 while the nuclear diameters are on the order of 10^{-5} . Since the electron cloud occupies 10^{15} times more volume, an electron collision is much more

probable however it's the NIEL that degrades the device. The generation of defects in the crystalline lattice has the effect of shortening the minority carrier diffusion length in the material by increasing the probability of carrier trapping and scattering. Radiation damage can be quantified through the use of damage constants. Minority carrier diffusion length damage constant is expressed as K_L expressed as

$$K_L = \frac{\left(\frac{1}{L_\phi^2} - \frac{1}{L_0^2}\right)}{\phi} \tag{2.22}$$

where L_ϕ is the minority carrier diffusion length at a given fluence (ϕ) and L_0 is the beginning-of-life (BOL) diffusion length. Carrier removal rate is expressed as a linear constant that is independent of BOL doping expressed as

$$N(\phi) = N_0 - R\phi \tag{2.23}$$

where N is doping and R is the carrier removal rate. With high fluences, carrier removal effects can decrease the effective doping of a material which often manifests as a widening in depletion width (w_d).

Radiation damage is of particular concern when designing multijunction devices because each subcell material degrades at different rates and different layer thicknesses are required to achieve proper BoL current matching. Figure 2.21 is a demonstration, from Patel et al.[28], of the relative change in J_{SC} from BoL to EoL of each subcell in a four-junction solar cell. The InGaP subcell is highly radiation damage tolerant while the GaAs and InGaAs subcells are significantly less so.

An early investigation of radiation tolerance of QDSCs was performed by our group (Cress et al. [29]) with a few notable conclusions. Spectral responsivity, a measure of how efficiently a solar cell is able to convert photons to electrons, is shown for a GaAs control cel and QDSCs at beginning-of-life in Figure 2.22(a), and after alpha particle exposure in Figure 2.22(b). The first conclusion was that the QD contribution to spectral responsivity remained relatively constant out to fluences that resulted in an 80% reduction in carrier collection in the bulk material, shown in Figure 2.22(c). Second,

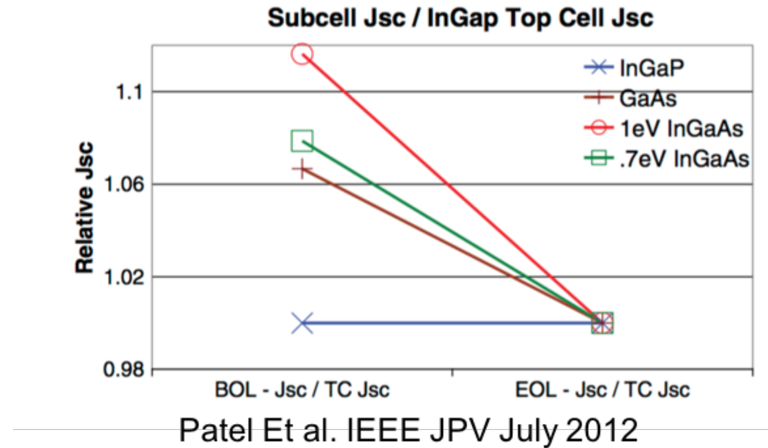

Figure 2.21: Plot of relative J_{SC} at BoL and EoL in a 4-junction IMM solar cell by Patel et al.[28]

a photoluminescence measurement showed that QD emission sustained over 50% of the beginning-of-life (BoL) intensity at an order of magnitude higher fluence as compared to bulk GaAs, shown in Figure 2.22(d). These results demonstrate the value of QDs for radiation hardness and maintenance of current generation. Further work, however, is required to conclusively demonstrate the cause, and to further maximize the radiation tolerance of the device.

Hubbard et al. [30] took the experimental approach of measuring displacement effects directly, and fabricated QD test structures for deep-level transient spectroscopy (DLTS), a technique where a voltage pulse is applied to a sample, and a transient capacitance is measured as a function of sample temperature. The change in capacitance and carrier escape time from traps vs temperature gives an overview of trap depth and location within the bandgap of the material. The conclusion of this study was that the QD device appeared to be less tolerant to an E4 defect, a majority carrier electron trap reported in literature, but suppressed formation of an E3 defect, in agreement with the hypothesis that the strain present in the QDs may increase the required knock-on energy for simple displacements[31].

There are two potential hypotheses for the increased radiation tolerance. The first hypothesis is that the strain present increases the required knock-on energy to create

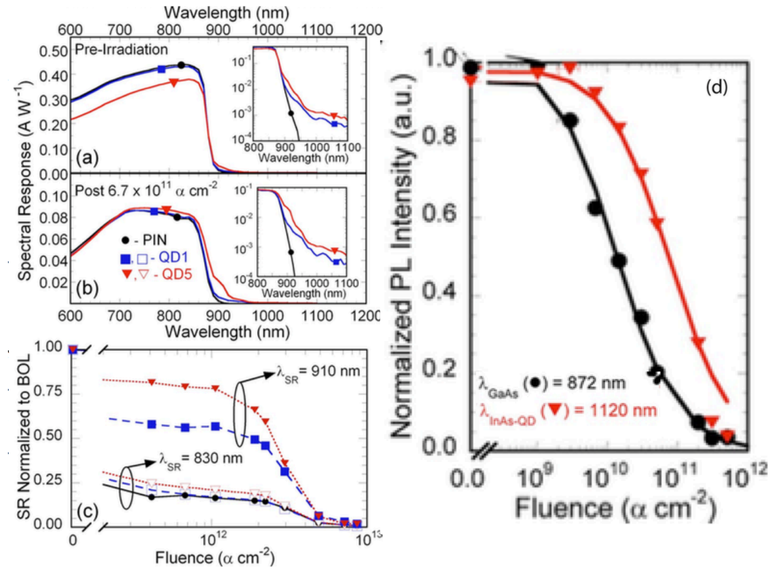

Figure 2.22: Spectral response vs wavelength for the reference (black circle), single QD layer (blue square), and 5x QD (red triangle) at (a) beginning-of-life, and (b) at $6.7x10^{11}\ \frac{\alpha}{cm^2}$. (c) shows spectral response vs fluence at 830 nm and 910 nm corresponding to GaAs and InAs QD absorption peaks respectively. (d) shows average PL intensities of GaAs control and a 5-layer InAs QD sample vs fluence. [29]

a displacement [31], thus directly inhibiting radiation damage. This concept is demonstrated in Figure 2.23 where the barrier to dislocation is lowered from around 36 eV to around 31 eV for an Indium dislocation along $\langle 201 \rangle$. While Kerestes *et al.*[31] provided good evidence that compressively strained samples provided better radiation hardness, one weakeness of the study is that all devices were selected from a single wafer, and strain effects were unintentional due to poor cross-wafer uniformity of either the QDs or the strain compensation layer.

The second hypothesis is that the QDs confine carriers in defect-free areas, preventing induced defect driven recombination, similar to reported effects the addition of QDs has on cell sidewall recombination [32]. This theory is supported by work in III-nitride optoelectronics where slight differences in bandgaps exist between wurtzite and zinc-blende crystals[33] with the difference in the two phases being the stacking sequence of III-N planes leading to a small potential energy difference[34]. This leads to carrier localization in zinc-blende domains which exhibit a high quality radiative recombination

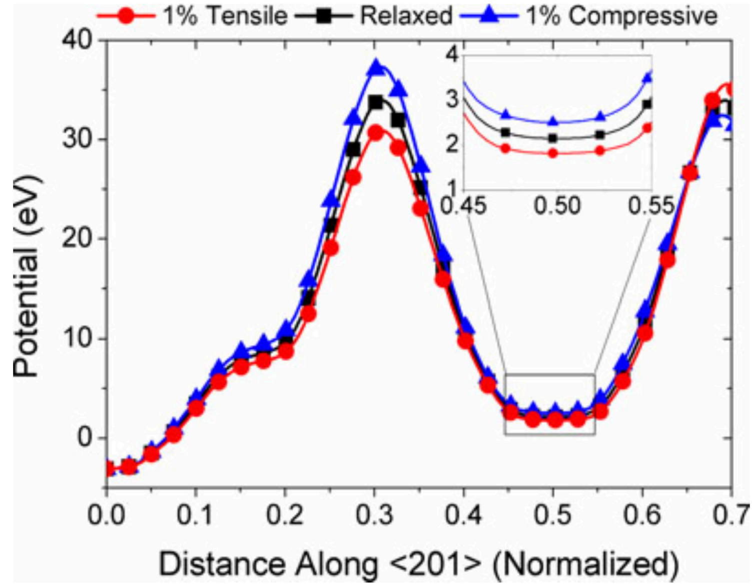

Figure 2.23: Potential energy of an Indium primary knock-on atom along ⟨201⟩ for a 1% compressive, relaxed, and 1% tensile-strained lattice, showing that the lattice under tensile strain has the lowest required energy for defect formation.[31]

in spite of high dislocation densities. The high defect tolerance of InAs/GaAs QDs has been used to fabricate 1.3 μm QD lasers on Si[35] which maintain high luminescent yield in spite of high dislocation densities, defects much larger and potentially detrimental than the densities of Frenkel defects seen in PV systems on satellites.

Chapter 3

Development of Quantum Dot Intermediate Band Solar Cells

3.1 Introduction

The intermediate band solar cell (IBSC), proposed by Luque and Marti [12], is a novel approach to breaking the Shockley Queisser single junction efficiency limit through spectral splitting in a monolithic device, which, unlike multijunction cells, requires only a few μm of material and a single electrical junction. A wide bandgap (E_G) host material is in order to minimize thermalization loss, and an intermediate band is established, allowing photons with energies less than the bandgap of the host material to promote an electron from the valence band into the intermediate band ($E_{V,I}$) and from the intermediate band into the conduction band ($E_{I,C}$). In the ideal case, with intermediate transitions of 0.7 eV and 1.23 eV with a 1.93 eV host material bandgap, it is possible to achieve a total power conversion efficiency of around 63%[12]. The challenge with this approach is establishing the intermediate energy level.

One proposed method of realizing the intermediate band is through the use of epitaxially grown quantum dots (QD)[15]. A highly lattice mismatched narrow-bandgap material is deposited, either via molecular beam epitaxy (MBE) or metal-organic chemical vapor deposition (MOCVD), and is allowed to relax in the Stranski-Krastanow growth mode into coherent droplets on the surface[16] before being capped by the host material. This results in a nanostructure in which charge carriers are confined in three dimensions. The energy levels within the QD are a function of QD material bandgap, barrier height, QD size, and material strain.

A great deal of work has gone towards demonstrating the intermediate band concept in In(Ga)As / GaAs quantum dot solar cell (QDSC) material systems [17, 18, 36]. Investigations have focused on evidence of sub-band collection and experimental evidence of sequential absorption. InAs/GaAs QDs have proven effective in bandgap engineering [20].However, this system is not ideal for IBSC. As the band offset is split between valence and conduction bands, the total confinement depth is limited to a few hundred meV, which is much lower than the ideal 0.7 eV separation for the IBSC concept[12]. Shallow confinement also makes suppressing thermal escape and thermal capture impossible[37].

In order to address the challenge of thermal escape and to select materials with energy levels more suitable for an IBSC, this study focuses on characterization of a new material system. The material selection rules applied for this study were: a type-II band alignment leading to no confinement in the valence band (VB), $0.7 - 1.2$ eV confinement in the conduction band (CB) to suppress thermal escape and align the IB near the ideal level, and a host material that is lattice matched to available substrate materials (GaAs or InP). Figure 3.1, was used to assist in selecting materials that followed the aforementioned selection rules. The figure is a band energy-lattice constant diagram. However, unlike the traditional crystal growers chart, it shows relative band positions instead of bandgap. The band positions and bandgaps have been modified to what they are for a given material that is strained, pseudomorphically, to the InP lattice constant as would be the case if it were grown below the critical thickness. $AlAs_{0.56}Sb_{0.44}$ (abbreviated to AlAsSb) is lattice matched to InP and has a bandgap (E_G) of 1.89 eV. InAs forms a slight type-II band alignment with AlAsSb, with a small negative offset in the valence band, and a large offset in the conduction band, making the combination of these two materials favorable for a prototype IBSC. The type-II band alignment may even be beneficial because it can lead to longer carrier lifetimes in the QD states. AlAsSb is, however, an indirect bandgap material with a direct bandgap (E_0) of 2.47 eV which leads to weak absorption and may limit carrier collection from QD states.

Figure 3.2 is the band structure of a $20x20x4$ nm hemispherical InAs QD in AlAsSb calculated using the 8-band $k \cdot p$ perturbation method, a method of approximating band

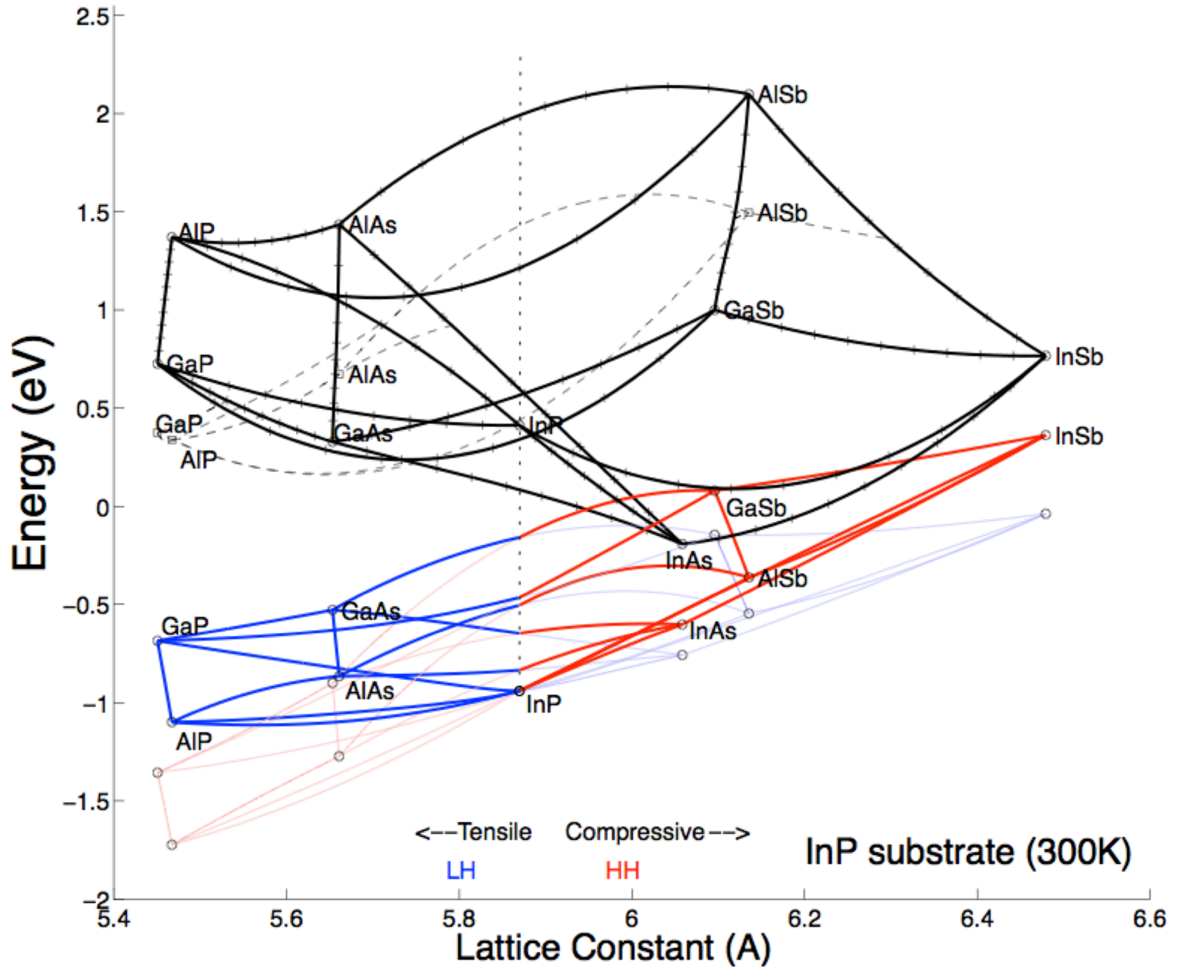

Figure 3.1: Band energy vs. lattice constant diagram showing relative offsets of conduction and valence bands of III-V materials when strained to the InP lattice constant. The conduction band positions are shown in black, while valence band positions are shown in blue. Strain that would be present if the material was strained to the InP lattice constant determines whether the light hole or heavy hole bands determine bandgap of the material. Generated by Dr. Staffan Hellstroem

structure. There is a multitude of states present. Three transition energies of interest are the valence band to QD ground state (QD0) transition ($E_{V,QD0}$), QD0 to AlAsSb indirect X valley in conduction band ($E_{QD0,X}$), and QD0 to AlAsSb direct Γ valley ($E_{QD0,\Gamma}$). These transitions were modeled to have energies of 0.78 eV, 1.1 eV, and 1.69 eV, respectively. Assuming fully populated QD states, the strongest intraband absorption, promoting electrons from QD to conduction band, is expected to occur from excited QD states to the AlAsSb Γ valley in the conduction band at energies ranging from $1.2 - 1.35$ eV, while a low probability exists of promoting electrons into the X valley from any QD

states[38]. Using this model as validation for the concept, we grew InAs/AlAsSb QDSCs in an attempt to establish a material system that enables excitation into and out of an intermediate state with energy levels that closely align with the theoretical ideal system.

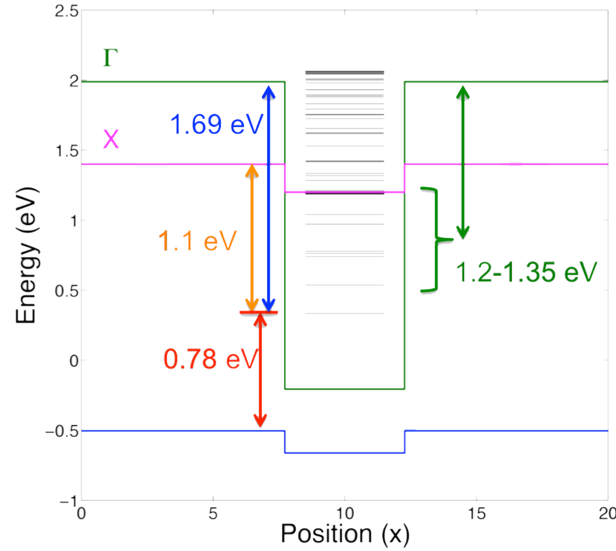

Figure 3.2: Result of 8-band $k \cdot p$ simulation of InAs/AlAsSb QD structure. E_v to E_{QD0} (red), E_{QD0} to E_X (yellow), E_{QD0} to Γ (blue), and $E_{QD,excited}$ to Γ (green) transitions are shown.

The next step was to incorporate the QDs into a device. The growth of these devices and optimization of InAs QDs in an AlAsSb matrix was performed by our collaborators at the University of California in Los Angeles Integrated NanoMaterials Core Lab. Figure 3.3 shows a schematic of the QDSC. A thin GaAs layer was grown before nucleating the InAs QDs because attempting to grow QDs directly on AlAsSb resulted in poor quality elongated QDs. The QD layers were capped with GaAs(Sb) in order to preserve QD quality[39].

Hall measurements were performed on test structures, where a 25 cm^2/vs hole mobility and a 606 cm^2/vs electron mobility were measured. Based on doping and expected material quality from fitting InAlAs results shown in literature [40], I estimated a hole lifetime of 20 ps in the heavily doped emitter, and an 806 ps electron lifetime in the lightly doped base. Figure 3.4 shows predicted EQE characteristics for 50 nm, 100 nm, and 200 nm emitter thicknesses with a 1.5 μm base thickness. Thinning the emitter too

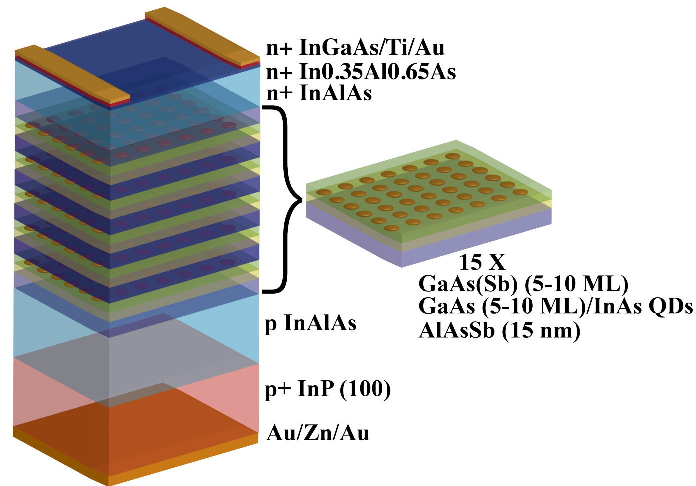

Figure 3.3: Schematic of QDSC layer structure used in this study.

far risks a degradation in fill factor from lateral spreading resistance as majority carriers need to flow to the grid fingers to be extracted and shifts current collection to the thick base, which can be problematic if material quality is mediocre. The final design employed a 75 nm emitter and is shown in Table 3.1. A control cell without QDs was also grown to provide a baseline for expected device performance and in order to determine whether or not the addition of QDs resulted in an improvement.

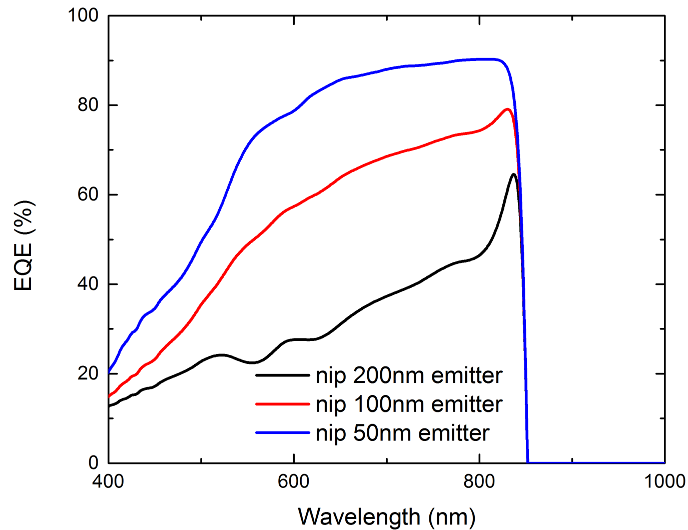

Figure 3.4: Modeled EQE of various InAlAs control cell designs, varying the emitter thickness from 50nm to 200 nm

Devices were fabricated with Au/Zn/Au contacts to the p-InP substrate and Ti/Au

Table 3.1: Devices included in study

	Control	QDSC
Contact	15nm n^{++}-InGaAs	
Window	20nm n^{+}-$In_{0.35}Al_{0.65}As$	
Emitter	75nm n-InAlAs	
Intrinsic	*uid*-InAlAs	15x QD
Base	1.5 μm p-InAlAs	
BSF	200nm p^{+}-InAlAs	
Substrate	350 μm p-InP (001)	

contacts to the InGaAs contact layer. Devices were isolated with a H_3PO_4:H_2O_2:H_2O wet mesa etch, and the contact layer was cleared between grid fingers using a Citric Acid:H_2O_2 mixture. Devices are $1cm \times 1cm$ with $\sim 4\%$ grid shadowing. No antireflective coating (ARC) was applied.

One-Sun AM0 illuminated IV measurements were performed with a two-zone TS Space Systems solar simulator with a Keithley 2440 SMU. External quantum efficiency (EQE) was calculated from spectral responsivity (SR) measurements using an Oriel IQE200 monochromator and a Stanford Research SR570 preamplifier coupled to a SR830 lock-in amplifier. $I_{SC} - V_{OC}$ measurements were performed using a Keithley 2400 SMU and a halogen bulb. Electroluminescence (EL) was measured with Ocean Optics NIR512 and HR4000 spectrometers.

3.2 Device Results

Figure 3.5 shows AM1.5G illuminated JV characteristics of the solar cells in this study. The InAlAs control cell exhibits a short circuit current density (J_{SC}) of 12.55 mA/cm^2 which, while on the low side, is in line with previously reported experimental results. Leite *et al.*[40]. report 19 mA/cm^2 in an InAlAs solar cell with an AR coating, which corresponds with around 13 mA/cm^2 without one. Efficiency suffers from what appears to be a reduced fill factor from shunting, and an open circuit voltage (V_{OC}) of 803mV, potentially the result of shunting or another dark current mechanism. The QDSC shows a further degraded J_{SC} and V_{OC}, a problem common early in experimental QD systems [19], especially if strain accumulation is not fully mitigated. Further testing was performed to help determine the root cause of the degradation.

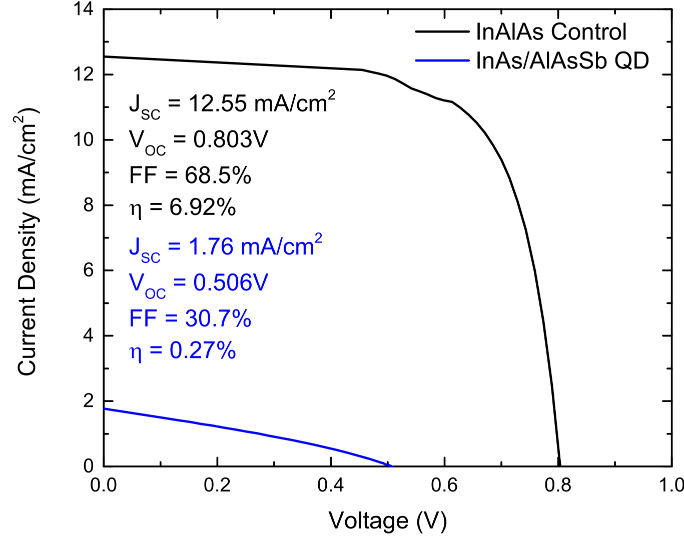

Figure 3.5: AM1.5G JV of InAlAs control cell and InAlAs cell with 15x InAs/AlAsSb QD.

Dark IV and I_{SC}-V_{OC} measurements, shown in Figure 3.6, were taken in order to further investigate diode characteristics and to extract parasitic resistance terms. The InAlAs control cell had a series resistance (R_S) of 0.793Ω and a shunt resistance (R_{SH}) of 12.6kΩ. The low shunt resistance explains the sloping shown in the light JV curve around J_{SC} and the reduction in fill factor. The QDSC, however, shows an R_S of 110Ω which explains the resistor-like electrical characteristics. The wide bandgap AlAsSb barrier that composes most of the i-region may be impeding carrier transport through the device, resulting in a high cell series resistance. The increase in cell shunt resistance from 12.6kΩ to 55.1kΩ in spite of any strain-induced defects QD growth could have caused supports this hypothesis because the wide bandgap material exists inside the bulk shunt pathway.

Figure 3.7 shows a band diagram of both the InAlAs control cell and a matching device with an AlAsSb uid region simulated in Synopsis TCAD^{TM}, a commercial semiconductor finite element analysis simulation tool. QDs are omitted for the sake of simplicity but would not make a major difference. The AlAsSb i-region should indeed act as a current barrier, inhibiting collection of electrons generated in the base of the device. A smaller energy barrier exists in the valence band that could potentially block carriers injected into the i-region from the emitter.

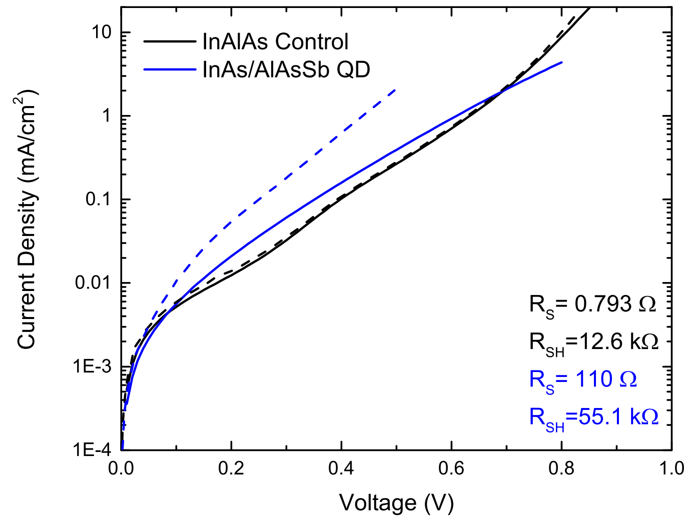

Figure 3.6: Dark JV (solid line) and J_{SC}-V_{OC} (dashed line) of InAlAs control cell and InAlAs cell with 15x InAs/AlAsSb QD.

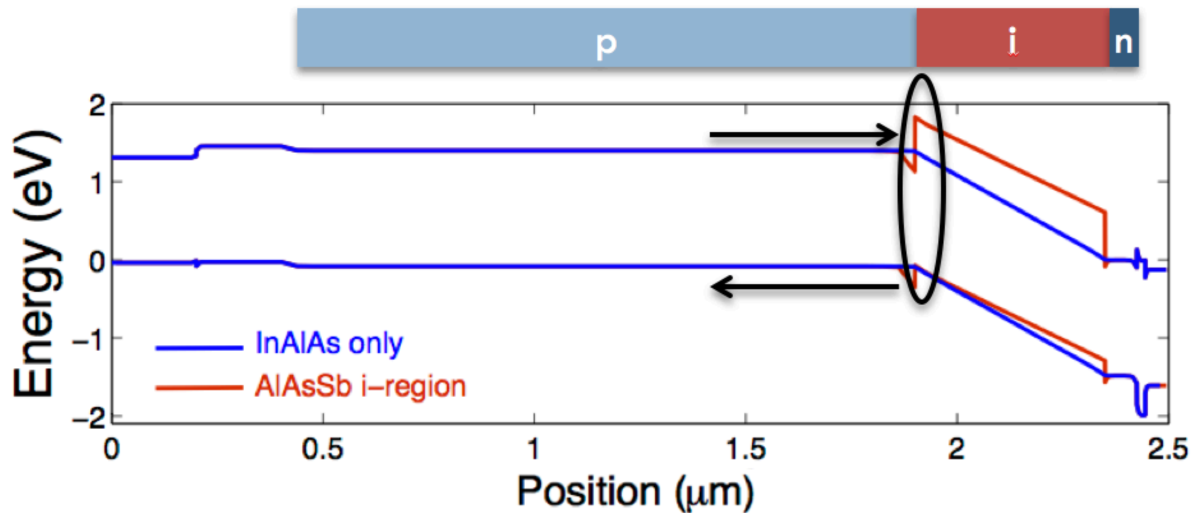

Figure 3.7: Band diagram of nip InAlAs solar cell with and without AlAsSb uid region showing the electron barrier preventing the transport of photogenerated current through the diode.

In order to assess photon collection efficiency, spectral responsivities (SR) of the control and QDSC were measured. Room temperature external quantum efficiency (EQE) of the QDSC, plotted with electroluminescence (EL) as a point of comparison is shown in Figure 3.8. The EQE curve shows a degradation in bulk collection in the QDSC as compared to an InAlAs control cell. The cause of the degradation is the AlAsSb QD cladding acts as a current injection barrier in the solar cell leading to greatly reduced current collection and a sharp reduction in fill factor[3]. The QDSC showed collection out

to 1750 nm (0.71 eV) while an InAlAs control cell showed an abrupt cutoff in collection at 860 nm (1.44 eV). This suggests that the QDs are effective at introducing sub-bandgap absorption out to the target VB-IB energy separation. The EL peak at 0.764 eV aligns with $E_{V,QD0}$ and is indicative of relatively low-defect material as crystallographic defects lead to nonradiative recombination. However, collection from the sub-band state under monochromatic illumination suggests that either there is an equilibrium carrier population in the QDs, or thermal escape from the QDs is still occurring in spite of the 1.1 eV confinement potential. While direct thermal excitation is unlikely as the thermionic lifetime from 1.1 eV confinement is on the order of hundreds of milliseconds as calculated from Schneider et al.[41], there may be some phonon-ladder effects due to the relatively high density of states in the QD.

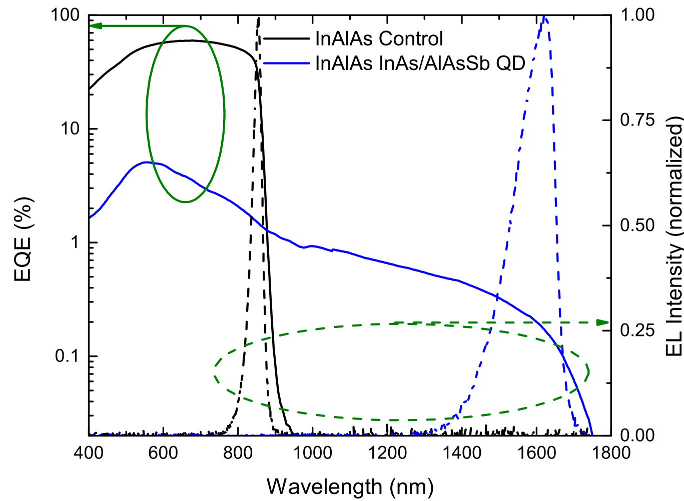

Figure 3.8: EQE and EL of InAlAs Control cell and InAlAs cell with 15x InAs/AlAsSb QD. No ARC was applied

Thermally driven collection, as shown in the EQE measurement is not necessarily beneficial because it may mean Fermi level separation from the IB to CB is not achieved. The ideal system should only allow optically driven excitation from QD state to conduction band. The next section is an investigation into two-step photon absorption and direct measurement optical transitions.

3.3 Probing Intermediate Transitions

3.3.1 Modulated Spectral Responsivity

As an integral part of the IBSC concept is the ability of the intermediate band or intermediate states to allow for absorption to promote into and out of the intermediate band, a custom experimental setup was required to look for this phenomenon of sequential absorption. The goal of the experimental setup should be to demonstrate increased collection strength from the intraband transition by exciting the interband transition. Standard SR measurements employ a monochromator to generate a photocurrent. As excitation out of a QD requires an established carrier population in the QD, a somewhat non-conventional technique to measure spectral responsivity has been developed to specifically probe an intermediate band or intermediate states[17, 21]. The SR setup in this study, shown in Figure 2.14, similar to that used by Antolin et al.[21], employs both a monochromator and a tungsten lamp with a 1500 nm cut-on filter. Conventional SR is taken with a chopped monochromatic signal, and a change in SR due to the presence of a second light source (ΔSR) is measured by modulating the filtered IR light while holding the monochromatic light constant. As the IR lamp is chopped, it modulates the carrier population in the QD. When the monochromatic light is at a wavelength that can facilitate promotion from the QD into the conduction band, a ΔSR can be directly measured. Both temperature dependent SR and an IR light biased pump-probe ΔSR were measured in order to investigate carrier collection strength from the QDs.

Figure 3.9 shows both temperature dependent ΔSR (top), and temperature dependent relative SR (bottom). Starting from the bottom plot in Figure 3.9, it is apparent from the non-zero collection past 860 nm, the InAlAs band edge, that carrier escape from QD states is still not entirely suppressed at 20 K, but reducing temperature drastically reduces the SR $\frac{peak_{qd}}{peak_{bulk}}$ ratio which shows that thermal escape from the QDs is arrested. The 15 nm AlAsSb barrier should be sufficient to suppress tunneling escape out of the QDs. With increasing temperature, sub-band photoresponse is enhanced, and a peak becomes apparent around 1.2 eV, near the edge of expected optical QD to Γ transitions.

With increased thermal energy, more intraband excitation is expected, and the presence of the peak around 1.2 eV is evidence that some equilibrium population of carriers exists in the QDs, allowing for single-photon driven collection, which may possibly reduce the probability of seeing sequential absorption in the 2-photon experiment.

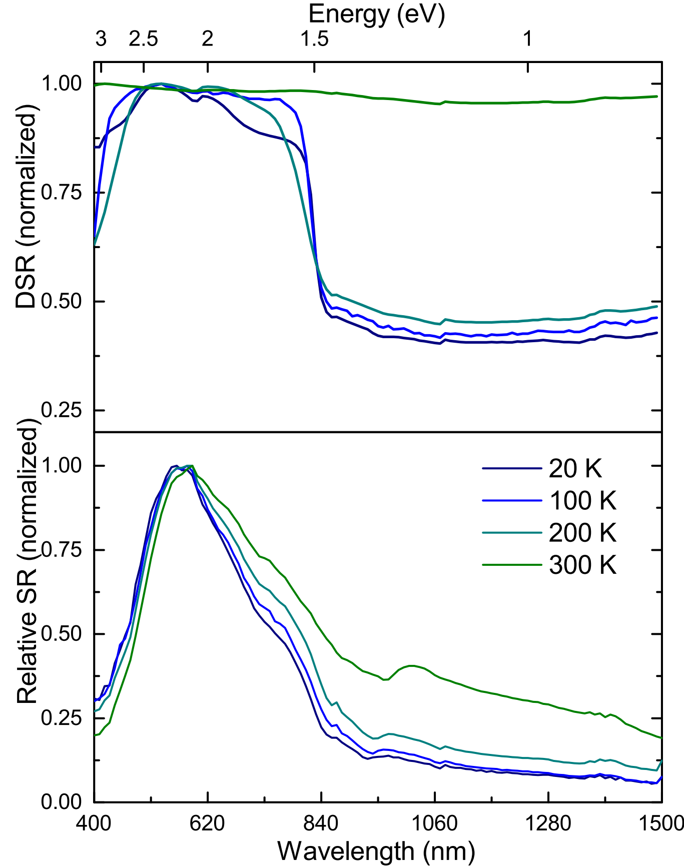

Figure 3.9: ΔSR (top) and conventional SR (bottom) measurements as a function of temperature.

Figure 3.9 (top) shows the result of ΔSR at 20 K to 300 K, normalized for detail. A background photocurrent was measured through the 1500 nm cut-on filter. At room-temperature, little change was seen spectroscopically with changing monochromatic pump wavelength. After cooling the sample to 20 K, an increase in SR was seen with monochromatic pump energies > 1.5 eV, corresponding to $E_{QD0-1,\Gamma}$, but no higher order excited QD to Γ transitions, or any QD state to X transition appears to be enhanced by the presence of IR illumination, suggesting few carriers are present in QD excited states due to ladder climbing as well as weak absorption to the indirect conduction band.

Selecting a direct bandgap host material, or one where the Γ and X valley energy separation is lower should enhance absorption strength coming from carriers trapped in QDs. As temperature is increased, the background AC signal from the IR illumination increases, suggesting a higher carrier escape probability, until the ΔSR signal is lost in the background.

3.3.2 Photoreflectance

While SR demonstrates collection, it does not allow for direct measurement of energy levels because absorption is convolved with collection. In order to directly probe the electronic structure of the QD material, photoreflectance (PR) was measured. PR is a sensitive contactless method, capable of determining the electronic structure of complex material systems[42]. While photoluminescence (PL) requires an optical transition to provide a radiative recombination pathway (that also supports a high recombination probability as compared to other recombination paths) and often requires deconvolution of buried gaussian-like peaks, photoreflectance results in a spectrum resembling the derivative of the dielectric constant of the material. As a modulation spectroscopy technique, it uses an electric field, induced and modulated by a chopped laser to change the index of refraction of the material, to measure a small change in reflectance, ΔR/R. Fitting this data uses an Aspnes third-derivative functional form (TDFF) for bulk materials and the first-derivative functional form (FDFF) for nanostructures[43]. The photoreflectance measurement in this study employs a chopped Ar ion laser ($\lambda = 514$ nm) and a broadband fiber coupled white light source reflected into a Horiba iHR320 monochromator. A diagram of the photoreflectance setup is shown in Figure 3.10.

Figure 3.11 is a photoreflectance spectrum from the device in this study. The first apparent transition has an oscillator center (TDFF) at 1.453 eV, which agrees with expectations for bulk InAlAs. The second strong transition (FDFF) is seen at 0.720 eV, which, going back to Figure 3.2, is close to the predicted 0.78 eV transition. The addition of the GaAs(Sb) spacers, or larger-than-expected dots can account for the discrepancy in these energies. Finally, a broad oscillator (FDFF) is seen at 1.307 eV, which, again

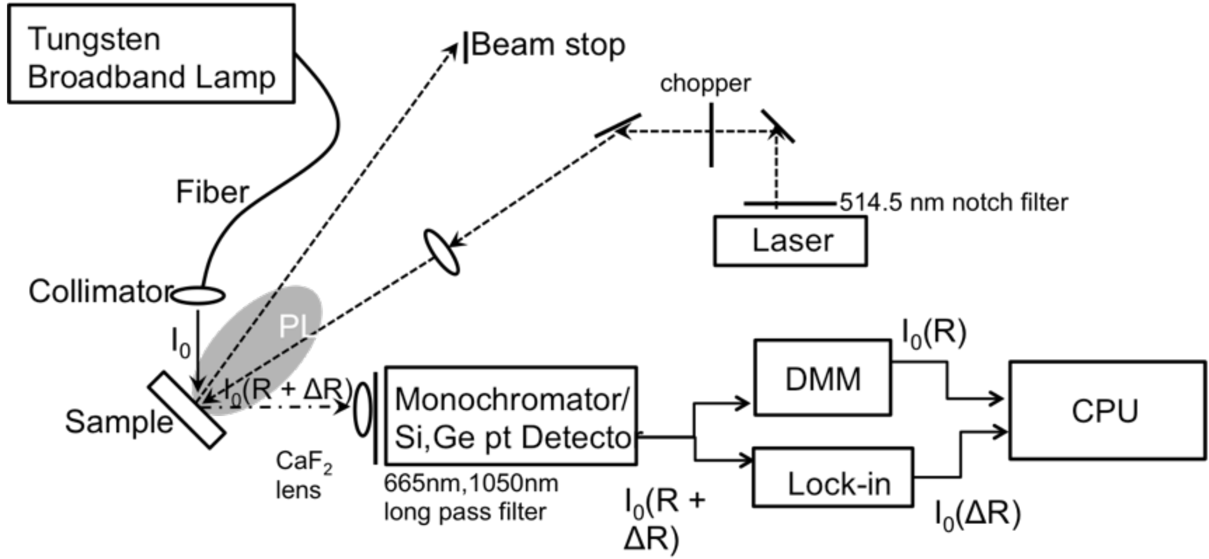

Figure 3.10: Diagram of photoreflectance setup.

referencing Figure 3.2, is in line with a series of expected excited QD to AlAsSb Γ point. This suggests a direct observation of an intraband optical transition being established by adding QDs to AlAsSb. The lack of oscillations of energies on the order of $E_{QD,X}$ suggests that excitation to the X valley is improbable.

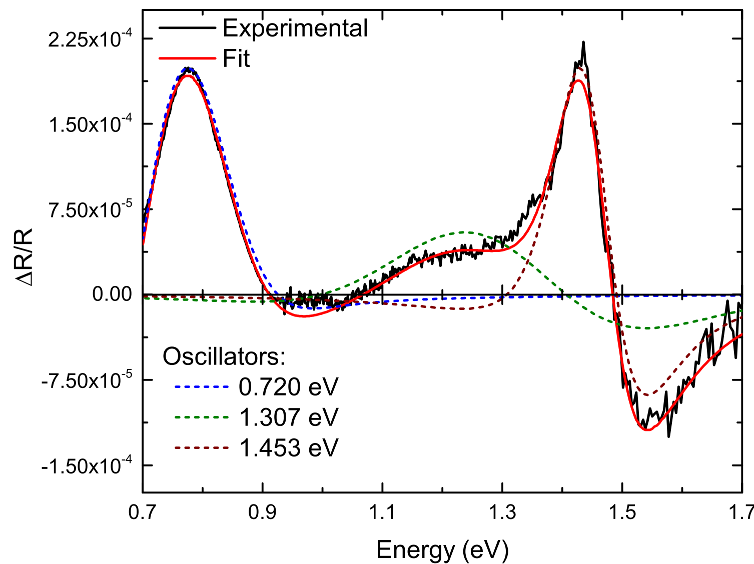

Figure 3.11: Photoreflectance spectrum of InAlAs device with InAs/AlAsSb QDs. Oscillators fitted to 0.720 eV, 1.307 eV, and 1.453 eV.

While the above results validate the material system as a prototype IBSC system, the electrical properties of these devices were poor. The next step is a study to improve the

electrical performance of the heterojunction design.

3.4 Redesigned Device

3.4.1 Experimental

The QDSCs presented in Section 3.2 exhibited promising optical properties via the TSPA spectroscopy measurement as well as from photoreflectance, but the AlAsSb barrier matrix around the QDs prevented current collection and severely degraded the electrical characteristics of the solar cell necessitating a redesign. We determined that a pin device polarity with an AlAsSb emitter would be more suitable. Figure 3.12 is a band diagram of the redesigned cell generated in Sentaurus TCAD, showing that with this polarity, the AlAsSb/InAlAs heterojunction should block diode forward current while allowing the photogenerated reverse current to move unhindered through the device.

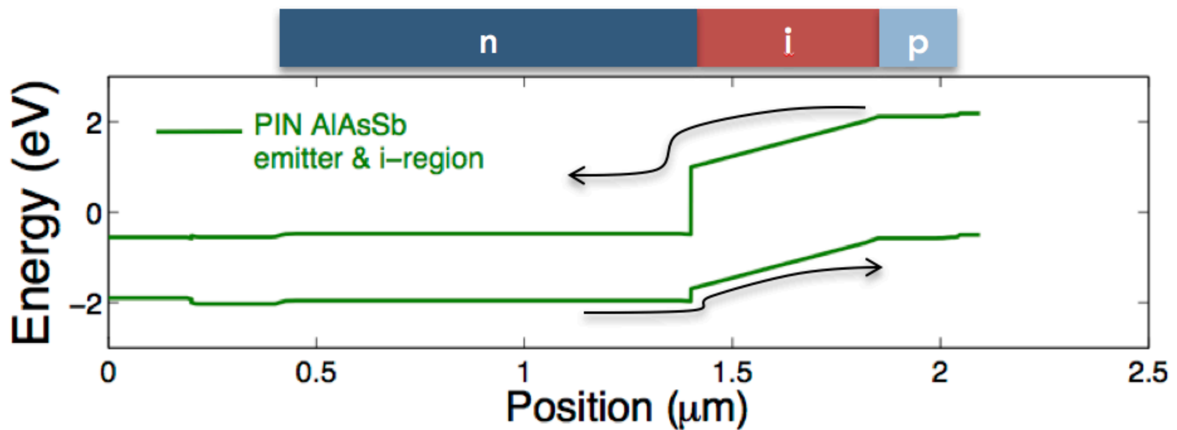

Figure 3.12: Band diagram of InAlAs solar cell with AlAsSb emitter and uid region showing the elimination of the electron barrier that prevented the transport of photogenerated current through the diode.

In order to validate the design, three devices were grown via MBE. The first is a *pin* InAlAs control cell with a 400nm *uid* region grown between emitter and base in order to keep region thicknesses constant with QDSCs. The second device consists of an InAlAs emitter and base, but contains an AlAsSb *uid* region without QDs in order to investigate if the AlAsSb region still behaves as a current blocking layer with the *pin* configuration. The final device has an AlAsSb emitter and *uid* region, which Sentaurus simulations

suggest will alleviate problems with carrier transport through the device. A sumary of devices is shown in Table 3.2.

Table 3.2: Devices included in study

	Control	AlAsSb intrinsic	AlAsSb emitter/intrinsic
Contact	15nm p^{++}-InGaAs		
Window	20nm p^+-$In_{0.35}Al_{0.65}As$		n/a
Emitter	150nm p-InAlAs		150nm p-AlAsSb
Intrinsic	*uid*-InAlAs	*uid*-AlAsSb	
Base	1.0 μm n-InAlAs		
BSF	200nm n^+-InAlAs		
Substrate	350 μm n-InP (001)		

3.4.2 Results & Discussion

Current-Voltage (IV) measurements were taken under a simulated AM1.5G solar spectrum. The results, in Figure 3.13, show that the InAlAs control cell exhibits collection characteristics comparable to previously published results [44], with a short circuit current density (J_{SC}) of 12.0 mA/cm^2. Inserting an AlAsSb layer in the intrinsic region of the device results in a reduction of J_{SC} to 3.73 mA/cm^2 as well as a sharp reduction in fill factor. A degraded open circuit voltage V_{OC} is also seen. Utilizing an AlAsSb emitter and intrinsic region results in a recovery of J_{SC} and fill factor, but a further decrease in V_{OC} is measured, limiting achieved efficiency recovery. While use of an AlAsSb emitter resolves the problem of high Rs, the dark IV measurement shows that there is an increased dark current, consistent with the degraded V_{OC}.

Electrical characteristics of the two device designs utilizing AlAsSb intrinsic regions were further charactierized through dark IV and $I_{SC} - V_{OC}$ measurements. The measurements, shown in Figure 3.14, were taken in order to deconvolve diode effects from parasitic resistances. The extracted series resistance (Rs) from the device with an AlAsSb intrinsic region was 36.5Ω as compared to 1.64Ω for the device with the AlAsSb emitter and intrinsic region, supporting the hypothesis that the AlAsSb i-region behaves as a current-blocking layer. While exhibiting a lower Rs, the device with an AlAsSb emitter has an increased overall dark current, consistent with the reduced V_{OC}.

Figure 3.15 shows the external quantum efficiency (EQE) measured from the three

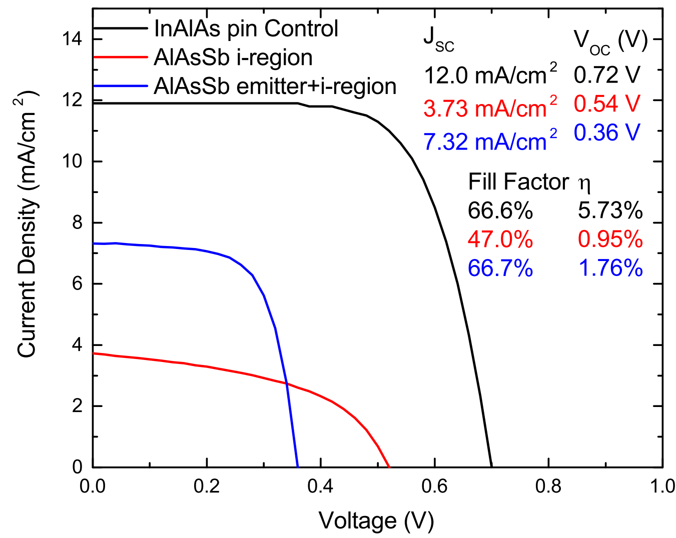

Figure 3.13: AM1.5G IV of the three devices included in this study.

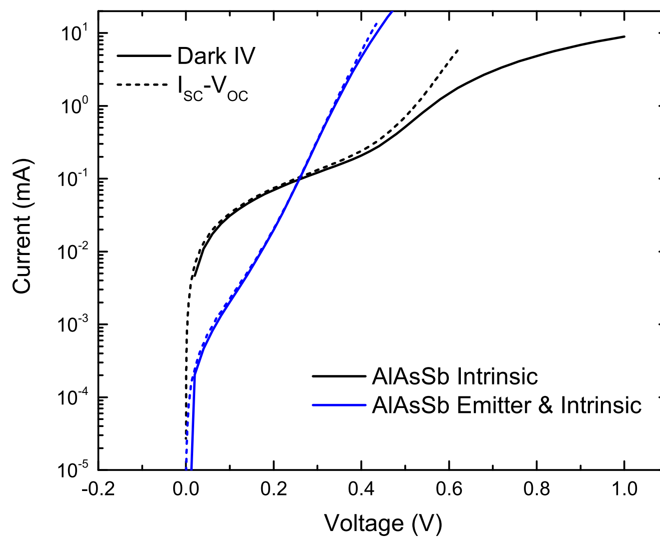

Figure 3.14: Dark IV and $I_{SC} - V_{OC}$ measurements from devices with AlAsSb *uid* region.

cells. The InAlAs control cell shows a peak QE of 55%, while both devices containing AlAsSb show a drop in EQE. Modeling the results using minority carrier diffusion equations[45] gives a base minority carrier diffusion length of around 280 nm, which is significantly shorter than the 1 μm base thickness, resulting in degraded base collection. The short minority carrier diffusion length in the base is mitigated by collection from the emitter in the InAlAs control cell, but is consistent with the measured EQE from the AlAsSb emitter/intrinsic region device. The same model suggests the AlAsSb emitter and intrinsic regions are parasitic absorbers, contributing little photocurrent to the solar cell. The basic minority carrier drift/diffusion model is not sufficient to explain EQE degradation seen in the device with an InAlAs emitter and AlAsSb i-region, which is further indication that current injection across the junction is being inhibited. Further analysis is required to determine why the AlAsSb emitter and i-region aren't assisting in light collection and why the InAlAs minority carrier diffusion lengths are so low in comparison to previous results.

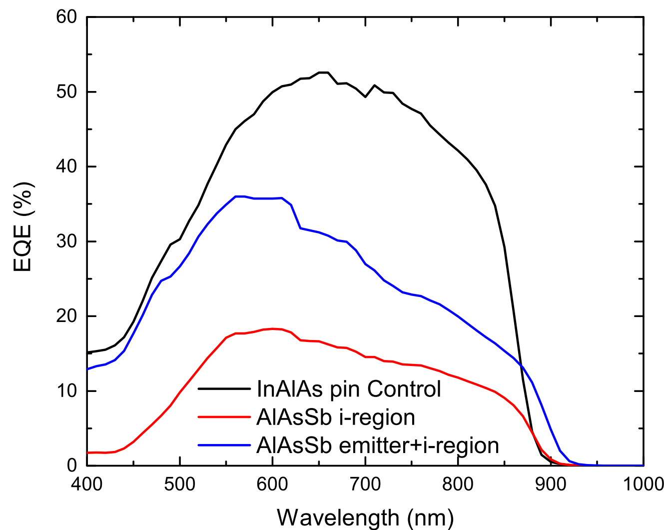

Figure 3.15: External quantum efficiency measurements of InAlAs control cell, InAlAs cell with AlAsSb i-region, and AlAsSb emitter/intrinsic InAlAs solar cell.

Transmission electron microscopy (TEM) of the cross-section from a sample consisting of an AlAsSb layer grown on InP, shown in Figure 3.16, reveals a high density of

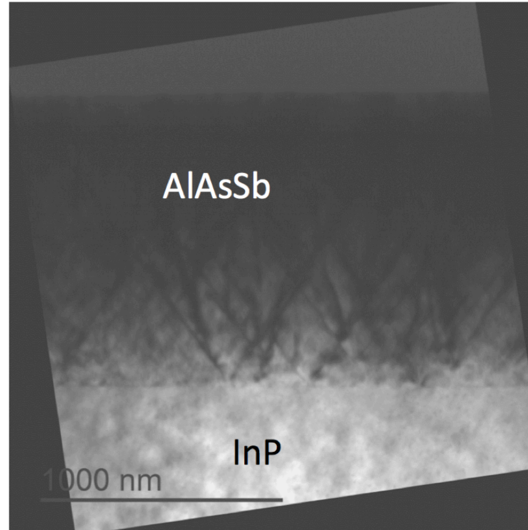

Figure 3.16: TEM cross-section of AlAsSb grown on InP showing threading dislocations nucleating from the AlAsSb interface.

threading dislocations propagating from the AlAsSb interface. XRD of the same sample confirmed that the AlAsSb layer is lattice matched to the underlying InP. The high density of extended defects in the AlAsSb emitter and intrinsic regions are expected to drastically reduce minority carrier diffusion lengths and to behave as recombination pathways contributing to the high dark current under forward bias.

3.5 Conclusions

In this work an intraband transition in InAs/AlAsSb QDSCs was measured via both photoreflectance and TSPA measurements in a system with a type-II band alignment, however the indirect bandgap of AlAsSb and poor material quality limit both the total photogenerated current and achievable open-circuit voltage. InAlAs was employed as an absorber material, however the band offset between InAlAs and AlAsSb blocks current collection in the cell. Switching to a *pin* polarity and employing an AlAsSb emitter mitigates barrier problems, driving fill factor recovery and demonstrating that the device problem was correctly identified as the InAlAs/AlAsSb material interfaces. The open circuit voltage remains low due to defects identified via TEM.

Chapter 4

Development of optimized QDSCs for multijunction PV

4.1 Introduction

Enhancing the efficiency of III-V photovoltaic (PV) devices beyond the single-junction Shockley Queisser (SQ) limit has been a driving issue in photovoltaic development. One approach has been to split the spectrum across multiple bandgap materials (e.g. multijunction PV). Another approach has been through bandgap engineering where nanostructures, such as quantum dots (QD) or quantum wells (QW), are suspended in a wider bandgap host material. Suspended nanostructures allow for quantum confinement effects, generating intermediate states within the host bandgap, resulting in the possibility of sub-bandgap absorption. Thermal escape, two-photon absorption, or Fowler-Nordheim tunneling [9] can drive carrier collection from quantum-confined states. Sub-band absorption enables a reduction in transmission loss, inherent to the SQ efficiency model. InAs/GaAs quantum dot solar cells (QDSC) have numerous applications in photovoltaics, including engineering the bandgap of single-junction GaAs cells closer to the detailed balanced optimum efficiency for concentrator photovoltaics [46] and enhancing efficiency of monolithic triple junction photovoltaics through improvements in current matching of the middle cell [47]. The InAs/GaAs material system has also been proposed as a candidate as a potential material system for prototype intermediate-band solar cell (IBSC) development [48]. Mitigation of dark current through the application of a heterojunction emitter can potentially further improve conversion efficiencies of the GaAs/InAs QDSC. A p-on-n device structure has conventionally been employed to take advantage of high

minority carrier mobility in p-GaAs. Integrating the InAs/GaAs QDSC into the current monolithic triple junction solar cell structure, used for high efficiency space applications, requires an n-on-p polarity. The cell polarity is dictated by the application of an arsenic diffused-junction Ge bottom cell on a p^+-Ge substrate [49]. Low hole mobility in n-GaAs coupled with short minority carrier lifetimes from heavy doping results in higher device sensitivity to emitter thickness. Application of a heterojunction emitter can potentially alleviate device sensitivity to emitter minority carrier lifetime.

The standard homojunction solar cell has a thin, heavily doped emitter above a thick, lightly doped base. Since a substantial portion of the spectrum is absorbed in the emitter, minority carrier lifetime (τ_e) in the emitter is critical for absorbed light to be collected. Lattice-matched wide-bandgap heterojunction emitters have been employed in photovoltaics to decrease minority recombination in the emitter through a reduction in absorption [50]. An added benefit is the potential band offset between the emitter and base can inhibit minority carrier injection into the emitter. This potentially reduces the diode dark current, increasing the open circuit voltage (V_{OC}) of the solar cell [50]. In this section, the goal is utilize QDs and cell design to engineer a high-efficiency reduced bandgap GaAs subcell for multijunction photovoltaics and to demonstrate improved radiation tolerance over conventional triple junction devices.

4.2 Experimental

For this study samples, shown in Table 4.1, were grown via metal organic chemical vapor deposition (MOCVD). Two sets of *nip* GaAs solar cells, each set consisting of a “baseline” and a ten layer (10x) superlattice InAs/GaAs QDSC with the superlattice imbedded in an i-region, were grown on 2” 10^{18} cm^{-3} Si-doped n-GaAs (001) wafers offcut 2° to the (110). Samples were grown in a Veeco D125 3x2” MOCVD reactor. The first set had a 100 nm homojunction emitter while the second set utilized a 100 nm $In_{0.48}Ga_{0.52}P$ (InGaP) heterojunction emitter. The p-GaAs base was grown at 650°C. The n-GaAs emitter was grown at 620°C. The n-InGaP emitter material was grown at 620°C. The InAs QD layers

were strain balanced using a GaP barrier discussed elsewhere [51]. QDs were grown with a 13s InAs deposition time to an approximate thickness of 1.8 monolayers[52] with a 60 second growth interrupt to allow for formation of QDs. Solar cells were fabricated using alloyed Ge/Au/Ni/Au *n*-type contacts and Au/Zn/Au *p*-type contacts. 1x1 cm^2 cells were defined with a wet chemical mesa isolation etch. Anti-reflective coatings were not employed. One-Sun AM0 illuminated JV measurements were performed with a two-zone TS Space Systems solar simulator at the NanoPower Research Labs at RIT with a Keithley 2400 SMU. Spectral responsivity was measured using an Optronic Laboratory OL750 monochromator. $J_{SC} - V_{OC}$ measurements were performed using a Keithley 2440 SMU and a halogen bulb.

Table 4.1: Devices included in study

	nip		Heterojunction	
	Baseline	10 x QD	Baseline	10 x QD
Contact	500nm n-GaAs Te $1.8 \times 10^{19} cm^{-3}$			
Window	30nm n-InGaP		10nm n-InGaP 20nm n-AlInP	
Emitter	100nm n-GaAs		100nm n-InGaP	
Intrinsic	100nm *uid*-GaAs	35nm GaAs 10x QD 35nm GaAs	100nm *uid*-GaAs	35nm GaAs 10x QD 35nm GaAs
Base	2.5 μm p-GaAs			
Window	50nm p-InGaP			
Substrate	350 μm p-GaAs (001) 2° to (110)			

4.3 Results

Figure 4.1 & Table 4.2 show AM0 illuminated IV characteristics of the solar cells used in this study along with previous *pin* devices as a point of comparison[52]. The QD devices in this study exhibited open circuit voltage reduction of less than 50 mV when compared to corresponding baseline samples, and V_{OC}s greater than 970 mV, which is indicative of high material quality. Both heterojunction cells show a substantial reduction in J_{SC} and a slight reduction in V_{OC} when compared to the corresponding homojunction *nip* cell. The minimal reduction in V_{OC} (5-10 mV) suggests that it is primarily coupled with the loss in J_{SC}. It is important to note that a slight increase in V_{OC} is expected from a reduction in dark current when employing a heterojunction. Both *nip* homojunction

and heterojunction QD samples also exhibited a reduction in J_{SC} compared to the corresponding control samples. Diode properties were further investigated using I_{SC}-V_{OC} method.

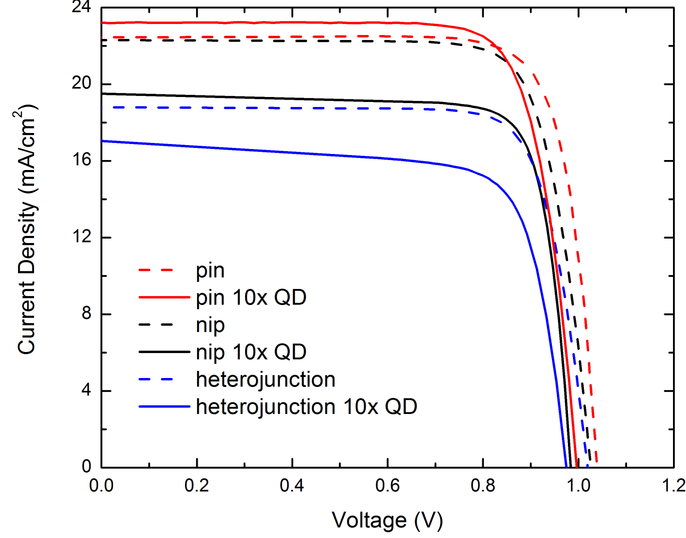

Figure 4.1: AM0 IV results for baseline, QD homojunction, and heterojunction emitter solar cells.

Table 4.2: Solar Cell AM0 IV Characteristics

Sample	J_{sc} (mA/cm^2)	V_{oc} (V)	FF (%)	η (%)
GaAs *pin*	22.47	1.039	80.0	13.8
GaAs *pin* 10× QD	23.21	0.997	78.5	13.4
GaAs *nip*	22.32	1.025	78.7	13.3
GaAs *nip* 10× QD	19.52	0.983	80.4	11.4
Heterojunction	18.81	1.020	78.9	11.1
Heterojunction 10× QD	17.04	0.974	80.4	7.2

Diode J-V characteristics with series resistance effects removed can be extracted using a variable intensity lamp and a SMU by measuring I_{SC} and V_{OC} at variable illumination levels. Figure 4.2 and Table 4.3 show that the heterojunction baseline exhibited an ideality factor closer to unity than the homojunction baseline, as expected from higher injection efficiencies achieved through the heterojunction structure. Both baseline cells exhibit nearly identical J-V characteristics around the 1-Sun V_{OC}, which suggests that under identical illumination conditions, or with an InGaP filter over both cells, open circuit voltages would be nearly identical. A reduction in dark current is expected with

the heterojunction structure, so interface recombination may still be affecting device performance.

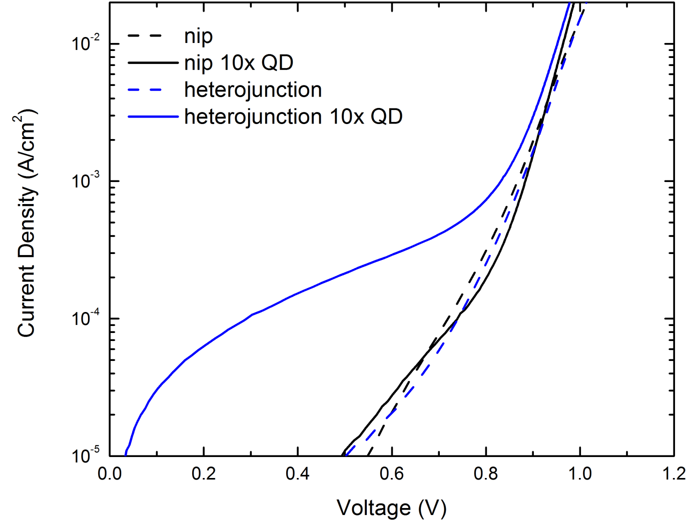

Figure 4.2: Solar Cell Jsc-Voc characteristics. Dotted lines represent control devices while solid lines represent the QDSCs.

Table 4.3: Device diode characteristics.

Sample	$J_{0,1}$ (A/cm^2)	n_1	$J_{0,2}$ (A/cm^2)	n_2
GaAs *nip*	2.35×10^{-11}	1.90	5.73×10^{-9}	2.83
GaAs *nip* 10x QD	6.90×10^{-15}	1.32	9.21×10^{-8}	4.05
Heterojunction	4.24×10^{-12}	1.75	5.51×10^{-9}	2.90
Heterojunction 10x QD	8.37×10^{-13}	1.58	3.99×10^{-5}	11.57

While the heterojunction emitter control sample exhibited no clear shunting in the J_{SC}-V_{OC} curve, the heterojunction QD device exhibited a shallow slope at low bias, indicative of shunting. This may be the result of degraded InGaP quality when grown after QDs. Kerestes et al. [53] demonstrated a degradation in the InGaP top cell performance in triple junction solar cells with QDs in the middle cell if strain-balanced conditions are not met. It is possible that increased surface roughness from buried QD structures along with any residual global strain can degrade the quality of InGaP. The degradation seen is not an insurmountable problem and could probably be addressed by optimizing growth conditions. Gudovskikh et al. suggest that $In_{0.47}Al_{0.53}P/GaAs$ and $Al_{0.8}Ga_{0.2}As/GaAs$ heterojunctions provide a reduced sensitivity to interface trap density as compared to

InGaP [50].

Both QD devices exhibited a near V_{MP} ideality factor closer to unity than the corresponding baselines. This suggests that the QDs may provide a suppression of non-radiative recombination in the quasi-neutral region [54]. This merits further investigation via the reciprocity relationship between EQE and EL and will be partially addressed in subsequent sections. The conclusion that can be drawn from the J_{SC}-V_{OC} plot is that the heterojunction emitter does not degrade the electrical performance of the cell, which leaves reduced collection from the emitter or parasitic absorption from somewhere else as possible causes of the degraded J_{SC} when comparing the heterojunction cells to the baseline *nip* cell. The cause of the current reduction was further investigated through spectral responsivity measurements shown below.

As shown in Figure 4.3, both QD devices show an increased sub-band response, indicative of a high quality, optically active superlattice structure. Fitting of the external quantum efficiency (EQE), shown in Figure 4.3, using minority carrier diffusion equations [45] yielded an emitter minority carrier diffusion length (L_e) of 92 nm in the homojunction emitter *nip* baseline, and 50 nm in the homojunction emitter QD cell. A reduction in base diffusion lengths was not required to obtain a good fit for the nip QD sample. Device modeling showed that an L_e greater than twice the emitter length is required to achieve nearly full collection from the emitter. Since the baseline L_e is nearly the same as the emitter length, emitter collection exhibits an extreme sensitivity to changes in minority carrier diffusion length. While the cells are strain balanced to minimize global out-of-plane strain, deviations from the perfect strain balancing conditions can cause some emitter degradation. The expected decreased sensitivity to emitter quality from switching to a heterojunction emitter [50] was not seen in this sample set. The cause of the degradation in heterojunction devices will be investigated below.

As with the GaAs emitter QDSC, the heterojunction emitter QDSC showed a decreased sub-650nm response. The EQE of the heterojunction devices coincides with the EQE of the homojunction emitter devices right at the InGaP band edge (650 nm), which suggests that a bulk of the J_{SC} reduction is from absorption in InGaP. In a triple

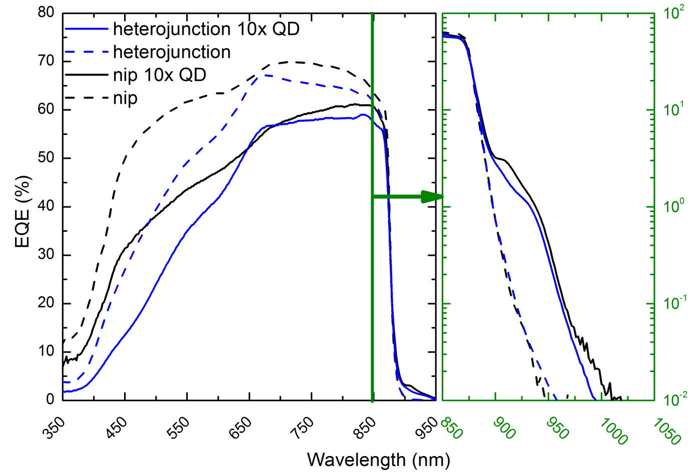

Figure 4.3: Full EQE spectra of QD solar cells with sub-band collection shown in log scale.

junction solar cell, the top cell would absorb heavily up to 650 nm, significantly reducing the difference in J_{SC} between the heterojunction and homojunction nip cells as well as provide nearly identical reflectance spectra between the two cells. A 3-junction isotype GaAs cell designed with a thick InGaP emitter to emulate absorption conditions of a 3-junction middle cell could be used to characterize cells designed as triple junction mid-cells, but short wavelength collection information is lost, which is critical for single-junction GaAs/InAs QDSC applications.

The heterojunction device was simulated in Sentaurus and interface recombination effects were added to the Hovel/Woodall model[45]. The results are shown in Figure 4.4. An emitter diffusion length of 20nm was extracted for the baseline heterojunction solar cell. Thinning the emitter to 30 nm in both models resulted in restoration in the EQE spectrum to comparable levels to the *nip* devices.

The heterojunction emitter QDSC should show a lower sensitivity to emitter quality than the homojunction *nip* cell because absorption in the emitter should be significantly lower, but looking at Figure 4.3, this does not appear to be the case. Figure 4.5 shows the heterojunction emitter 10x QDSC measured EQE compared to outputs from the modified Hovel/Woodall model and Sentaurus with collection from the emitter fully suppressed. It is clear, particularly from the modified Hovel/Woodall model, that the expected collection from the space-charge region (SCR) is greater than what appears to

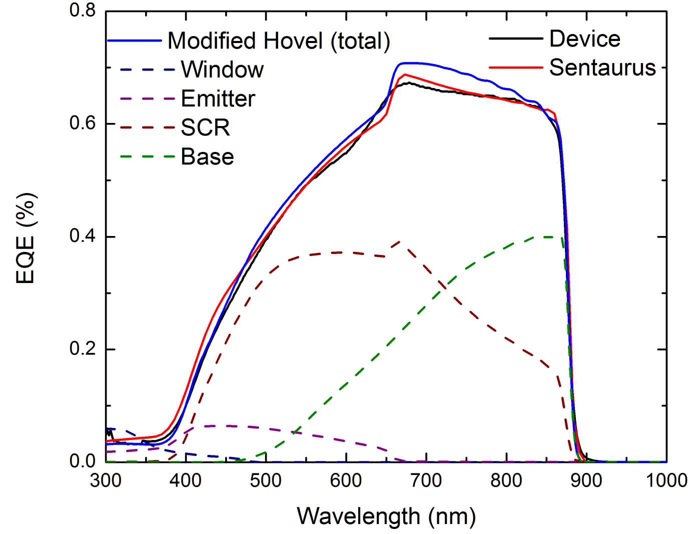

Figure 4.4: Fitting of EQE spectrum of heterojunction solar cell using a modified Hovel model and Synopsis Sentaurus.

be collected in the device. Two possible causes for the lower-than-expected collection are interface recombination, recombination in the SCR. The built-in potential (V_{bi}) of the *p*-*n* junction should suppress recombination effects in the depleted *i*-region at a 0V applied bias, so any defect causing substantial recombination in the SCR at I_{SC} should have a detrimental impact on V_{OC} when the electric field in the SCR is reduced. The two mechanisms mentioned above are unlikely because open circuit voltage is maintained in the QDSC. A third possibility is a phase separation effect in the InGaP emitter caused by strain induced by the QD layers[55],[56] changing the absorption profile of the InGaP emitter, but not resulting in an enhanced collection. If this is the cause of the degraded J_{SC}, thinning the emitter would alleviate parasitic absorption effects in the emitter.

4.4 QD Enhanced IMM Triple Junction Solar Cell

Since this work was started, SOA multijunction technology has shifted from tandem cells grown on Ge to inverted multijunction cells with a metamorphic InGaAs bottom cell, trading some of the Ge subcell excess current for increased open-circuit voltage. For these cells, a thick sacrificial layer is grown on the substrate. The top cell is grown first, followed by the middle cell, a metamorphic graded buffer in which the lattice constant is

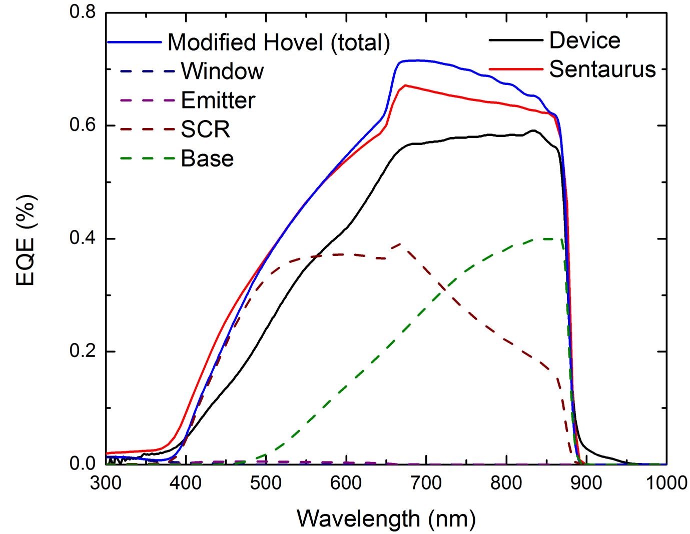

Figure 4.5: Fitting of EQE spectrum of heterojunction 10x QD solar cells using a modified Hovel model and Synopsis Sentaurus. QD collection is not included in this model

stepped towards larger atomic spacings, allowing for incorporation of InGaAs.

Figure 4.6 is an example asymmetric (224) RSM I took on a GaAs wafer with an InGaAs graded buffer. Pseudomorphically grown material shares the in-plane lattice constant with the substrate and bond elongation occurs along the $< 001 >$ surface normal direction. Both an "overshoot" and "undershoot" layer are grown in order to achieve the correct in-plane lattice constant before growing a layer with the target In composition.

After the lattice constant is graded, an InGaAs bottom cell is grown. The front of the wafer is then metallized, and the sacrificial layer is etched, removing the solar cell from the substrate. The *nip* polarity is still traditionally used. The IMM approach mitigates some efficiency loss, but does not address the non-ideal current matching between the top and middle junction, leaving room for improvement from realizing a bandgap engineered middle junction. Figure 4.7 is a detailed balance calculation with the top cell bandgap pinned at 1.9 eV and the middle and bottom cell bandgaps allowed to float, showing that an efficiency increase, if not as great of one as compared to the Ge based triple junction solar cell, is achievable with a 1 eV bottom cell if the middle cell bandgap is lowered. However, other challenges exist in the IMM solar cell such as achieving sufficient

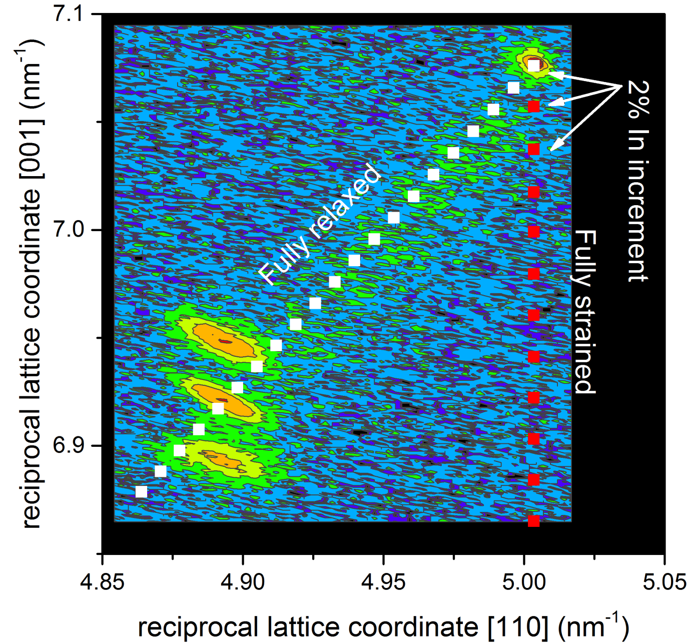

Figure 4.6: (224) reciprocal space map of $In_xGa_{1-x}As$ metamorphic buffer grown on GaAs taken on the RIT Bruker D8 Discover HRXRD

relaxation in the grading layers without causing threading dislocations to propagate through the bottom cell. The increase in efficiency from transitioning from a Ge based triple junction to an IMM triple junction is from improved current matching between the middle and bottom subcells.

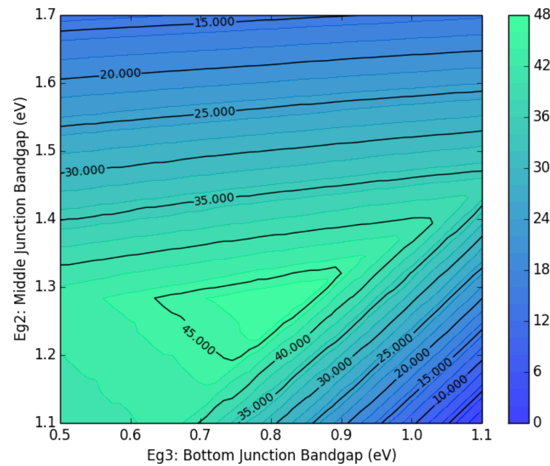

Figure 4.7: Detailed balance calculation showing maximum efficiency vs middle and bottom cell bandgaps with a fixed 1.9 eV top cell.

Shown in Figure 4.8 are spectral response results from a first attempt to add quantum dots to an inverted GaAs solar cell. The left plot is from the wafer of control cells, while the right plot is from the wafer of QDSCs[57]. The QDSC sample exhibited poor cross-wafer uniformity with sharp degradation by the band edge.

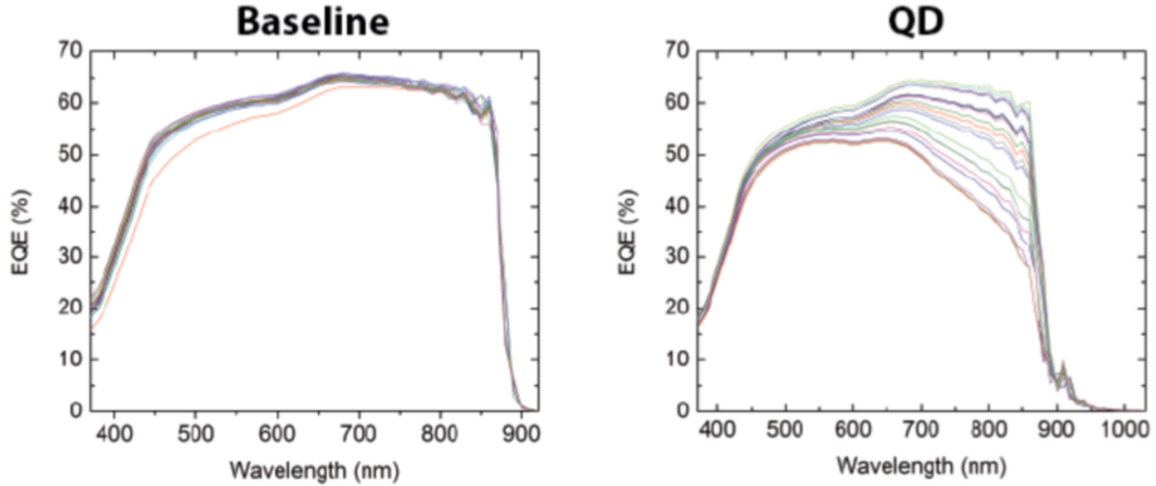

Figure 4.8: EQE results from inverted GaAs control cell(left) and GaAs/InAs QDSC(right).

Figure 4.9 and Table 4.4 includes modeled EQE and resulting predicted triple junction J_{SC} calculated by filtering light through a modeled top cell. The minority carrier diffusion length in the base varied from 470 nm to 2.3 μm in QDSC devices while no change in minority carrier diffusion length was seen in the emitter. Since the emitter is grown first in the inverted design, material degradation is shifted towards the base of the solar cell which is the opposite of what was seen in the upright *nip* design shown in Section 4.3.

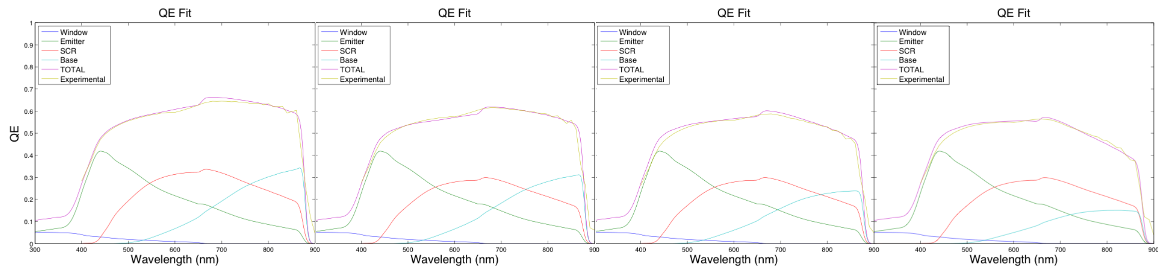

Figure 4.9: Fitted EQE of GaAs/InAs QDSC ordered by base MCDL arranged from longest to shortest MCDL.

Table 4.4: Device diode characteristics.

Cell	A	B	C	D
Base MCDL (μm)	2.3	1.8	1.0	0.47
SCR Collection	90%	80%	80%	80%
J_{SC} (mA/cm^2)	20.9	19.7	18.9	17.8
Predicted 3J J_{SC} (mA/cm^2)	15.6	14.6	12.7	11.4

Just as emitter degradation was seen in the upright solar cell design, adding QDs complicates base growth in the inverted design. Work will focus on redesigning the solar cell to mitigate these loses. The proposed redesign is shown in Figure4.10 and Table4.5. In the traditional design, the base of the solar cell is responsible for collecting 30% of the total current in the solar cell, on par with the emitter contribution. The solution to the problem shown here is similar to the solution from above; to shift carrier collection to the film grown before the quantum dots. By growing a thick, lightly-doped "base" before the QDs, collection is shifted to pristine material, and the GaAs layer grown after the QDs acts as a back surface field instead of an optically active layer. The two designs are called 'thick emitter' nip$^+$ and 'thin emitter' n$^+$ip designs.

Table 4.5: Devices included in study

	n$^+$ip 'Thin Emitter'	nip$^+$ 'Thick Emitter'
Top Cell	$InGaP_2$ Top Cell	
Emitter	100 nm 10^{18} n GaAs	3.1 μm 10^{17} n GaAs
Intrinsic	100 nm *uid*-GaAs	
Base	3.5 μm 10^{17} p GaAs	500 nm 10^{18} p GaAs
Bottom Cell	$In_{0.3}Ga_{0.7}As$ Bottom Cell	

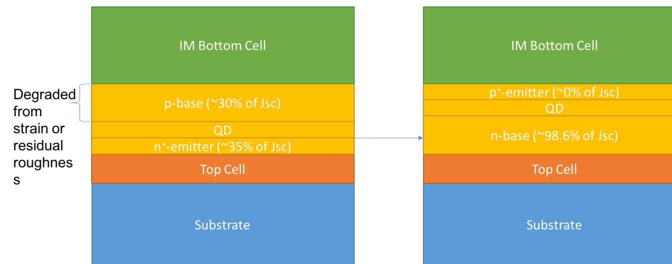

Figure 4.10: Diagrams of 'thick emitter' nip$^+$ and 'thin emitter' n$^+$ip designs.

The full triple junction stack with both middle junction designs (sans QDs) were simulated in Synopsis Sentaurus for validation of design. The resulting IV curves in Figure 4.11 predict no difference in open circuit voltage between the two designs, but

shows a 0.5 mA/cm^2 drop in J_{SC}. It is unclear whether or not this is a real effect, or a result of unoptimized material parameters fed into Sentaurus. Modeling using the Hovel model, used in the above work does not suggest the same drop in J_{SC}, but is not a good predictor for open circuit voltage. The Sentaurus simulation provides qualification for the idea.

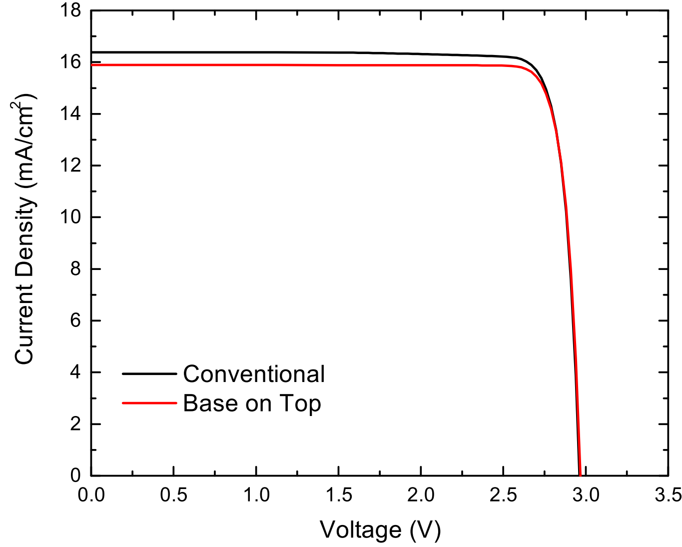

Figure 4.11: IV simulations of conventionally designed middle cell and redesigned middle cell in triple junction IMM

Table 4.6: Modeled Triple Junction AM0 IV Characteristics

Sample	J_{sc} (mA/cm^2)	V_{oc} (V)	FF (%)	η (%)
Conventional	16.38	2.96	87.5	31.0
Redesign	15.90	2.97	88.4	30.5

ELO templates on GaAs substrates with pre-grown In(Al)GaP top cells were sent from Microlink Devices Inc., a corporate partner for this project, to Rochester Institute of Technology where the middle junction for both control devices and QDSCs were grown in an Aixtron 3x2" close-coupled showerhead MOCVD reactor.Samples were then sent back to Microlink Devices for growth of the metamorphic buffer and $In_{0.3}Ga_{0.7}As$ bottom cell and for ELO and fabrication. Devices matching what is shown in Table 4.5 were grown as control cells with matching 10x QDSCs of both the thin emitter and thick emitter design. No antireflective coating (ARC) was applied. One-sun AM0 IV measurements

were performed on a two-zone TS Space Systems solar simulator and spectral response (SR) was measured using an IQE200 monochromator with a Stanford Research SR570 preamplifier and SR830 lock-in amplifier along with 570nm, 850nm, and 950nm LEDs for light biasing the top, middle, and bottom cells respectively.

Triple junction EQE measurements were taken and are presented in Figure4.12. Black curves are the results from the thin-emitter control cell and blue curves are the results from the thick-emitter control cell. The thin-emitter control device appears to be current limited by the bottom junction, which close current matching between middle and bottom junctions, while the top junction is current rich in comparison. The application of an ARC would assist in suppressing cavity modes in the GaAs subcell and further improve current matching between the three subcells. The samples have been sent back to Microlink Devices for ARC application and dicing. The top cell of the thick-emitter control cell shows a 2.7% decrease in top-cell integrated J_{SC} and a 2.8% decrease in middle-cell integrated J_{SC} compared to the thin-emitter control cell.The Accurate bottom-cell EQE measurements were not achieved for the thick-emitter control cell, suggesting some degradation such as shunting as this problem was not seen in the thin-emitter control cell. Control subcell design is not expected to impact either top or bottom subcell EQE performance.

Figure 4.13 compares measured EQE of the middle junctions between the two sets of control and QDSC devices. In both thin and thick emitter designs, the addition of QDs increases integrated J_{SC} without degrading bulk collection. Integrated SR between 850 nm and 1000 nm showed a 210 μA/cm^2 increase between thin-emitter control and QDSC and a 140 μA/cm^2 between thick-emitter control and QDSC devices. The difference in increased current between the two QDSCs appears to be caused by the proximity of a cavity-mode maximum in the thin-emitter device with respect to the band edge of GaAs. The application of an ARC would likely reduce this effect. A similar difference is seen between the 10x QDSC integrated current densities as is seen with the two control devices.

One-sun AM0 IV results are shown Figure 4.14. Again, the black curves are from

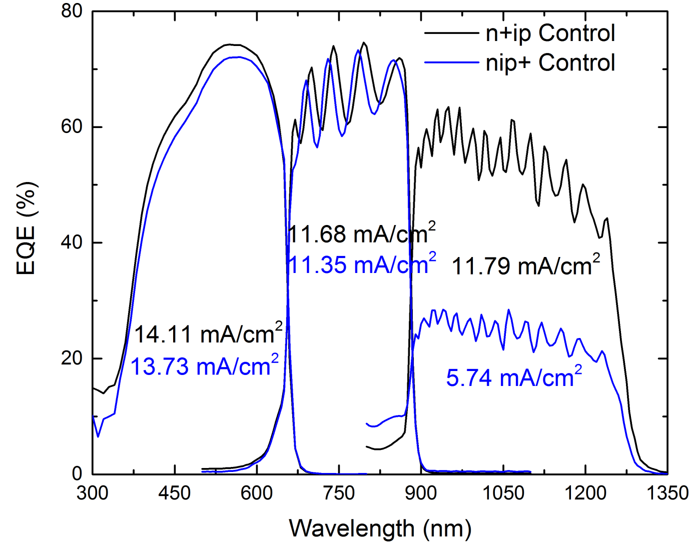

Figure 4.12: Measured EQE curves for top, middle, and bottom subcells of triple junction devices. Conventional thin-emitter designed cells are shown in black while the thick-emitter design is shown in blue.

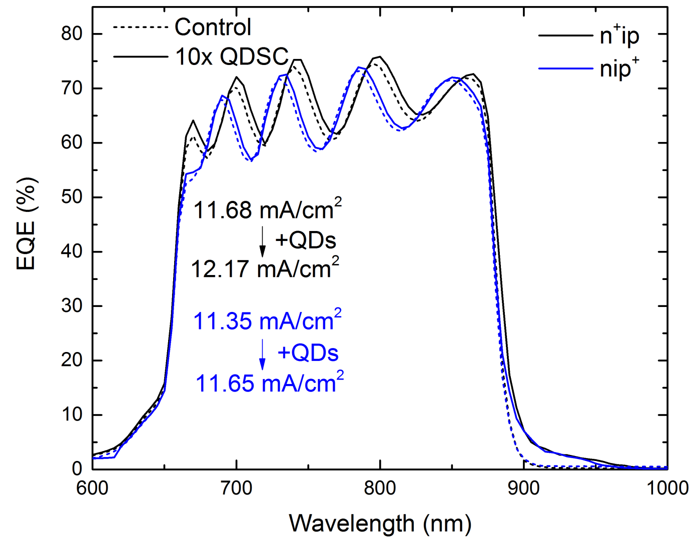

Figure 4.13: Measured EQE curves for middle subcells of triple junction devices comparing the relative change between the thin and thick emitter design and between control device and QDSC. Conventional thin-emitter designed cells are shown in black while the thick-emitter design is shown in blue.

the thin-emitter dataset, while the blue curves belong to the thick-emitter devices. The first thing to note is that the addition of QDs to the thin emitter design resulted in an increase in J_{SC} without a reduction in V_{OC}. The increase of 220μA corresponds with the increase in subband absorption shown in Figure4.13 above. The V_{OC} of both devices was

2.83 V, resulting in a relative efficiency enhancement of 1.8% from 21.9% to 22.3%. The increase in J_{SC} from the inclusion of QDs also demonstrates that the middle-junction is indeed current limiting. Conversely, in spite of the increase in SR integrated J_{SC}, the thick-emitter QDSC exhibited a decrease in J_{SC} compared to the control cell while the control cell showed a nearly 1 mA decrease in J_{SC} as compared to the thin-emitter control cell, suggesting both devices are bottom-cell limited meaning a yet undetermined factor degraded the bottom cell in both devices.

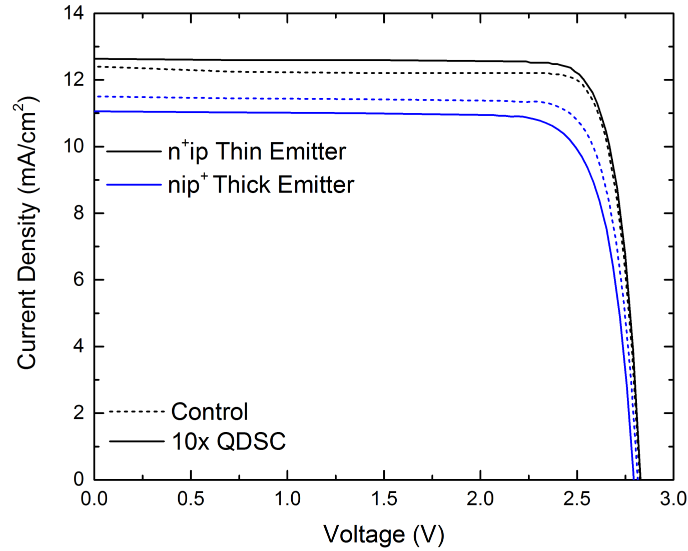

Figure 4.14: Measured AM0 JV curves for triple junction devices with and without InAs QDs in the GaAs subcell. Conventional thin-emitter designed cells are shown in black while the thick-emitter design is shown in blue.

Electroluminescence measurements were taken with an ASD Fieldspec, a calibrated spectrophotometer, on the control and 10x QDSC devices with a range of injection current densities from 4 mA/cm^2 to 120 mA/cm^2. The measurements taken at 120 mA/cm^2 are shown in Figure 4.15. Top and bottom cell EL intensities are comparable, although the bottom cell EL was not detectable at low current injection densities however the QDSC devices emitted at the GaAs band edge with 70-80% of the QD peak intensity at 120 mA/cm^2, suggesting that state filling in the QDs may play a role in open circuit voltage maintenance in the QDSCs.

In order to characterize subcell IV performance, the injection current dependent EL

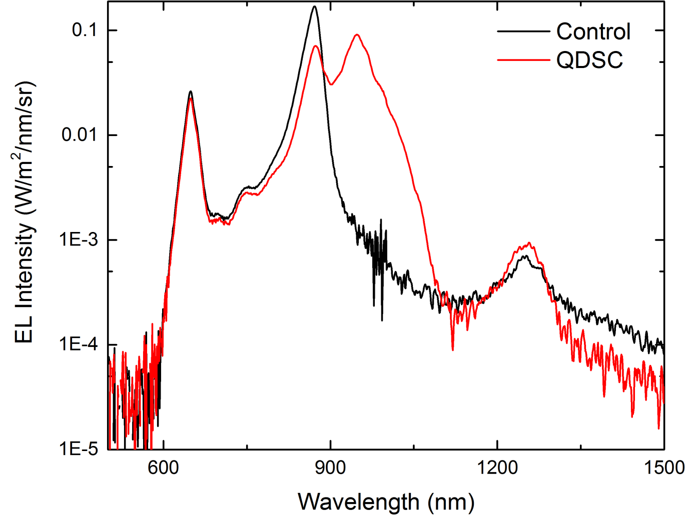

Figure 4.15: Triple junction solar cell electroluminescence measured with ASD Fieldspec. The control cell EL spectrum is shown in black and 10x QDSC shown in red. An injection current density of 120 mA/cm^2 is shown in this figure.

model was developed by Roensch et al.[58] using the spectral reciprocity relationship:

$$\phi_{EL,i}(J_{EL}) = \phi_{EQE,i}\phi_{BB}[e^{\frac{qV_i(J_{EL})}{kT}} - 1] \tag{4.1}$$

where J_{EL} is the EL injection current, $\phi_{EL,i}$ is the EL intensity of subcell i, $\phi_{EQE,i}$ is the EQE of the solar cell at the peak EL wavelength, ϕ_{BB} is the black body photon flux at the subcell EL peak wavelength, V_i is the current dependent subcell voltage at J_{EL}, and kT is the product of the Boltzmann constant and cell temperature.[58]

Rearranging the equation to solve for internal subcell voltage as a function of J_{EL} using the Boltzmann approximation gives the Equation:

$$V_i(J_{EL}) = \frac{kT}{q}ln[\phi_{EL,i}(J_{EL})] + \frac{E}{q} - 2\frac{kT}{q}lnE - \frac{kT}{q}ln(\phi_{EQE,i}) - \frac{kT}{q}ln(C) = V_i^*(J_{EL}) - \delta V \tag{4.2}$$

where E is EL peak photon energy and C is a constant calibration factor for the experimental setup. The calibration factor becomes the voltage offset δV. V_i^* is the internal subcell voltage. Summing the injection current dependent voltages of the three subcells gives the equation:

$$V_{OC,3J} = V_{OC,top} + V_{OC,mid} + V_{OC,bot} = V^*_{OC,top} + V^*_{OC,mid} + V^*_{OC,bot} - 3\delta V \tag{4.3}$$

which allows for the solution of δV because $V_{OC,3J}$ is a known value and $V_i(J_{SC})$ can be calculated from EL.

The above method was applied to the control cell and 10x QDSC in this work. In this method, the measured absorption EQE, the integrated peak emission intensity, and the peak emission energy are used to calculate a subcell voltage plus an offset due to system calibration. This offset, δV, is independent of EL injection current density and emission energy. Figure 4.16 shows the resulting reverse saturation current densities, ideality factors, and interpolated one-sun V_{OC} values for each subcell. The In(Al)GaP top cell and GaAs middle cell exhibited V_{OC} values in line with high quality subcells, however the InGaAs bottom cell appears slightly degraded, having a $W_{OC} > 0.6\ eV$, resulting in the triple junction V_{OC} of 2.83 V.

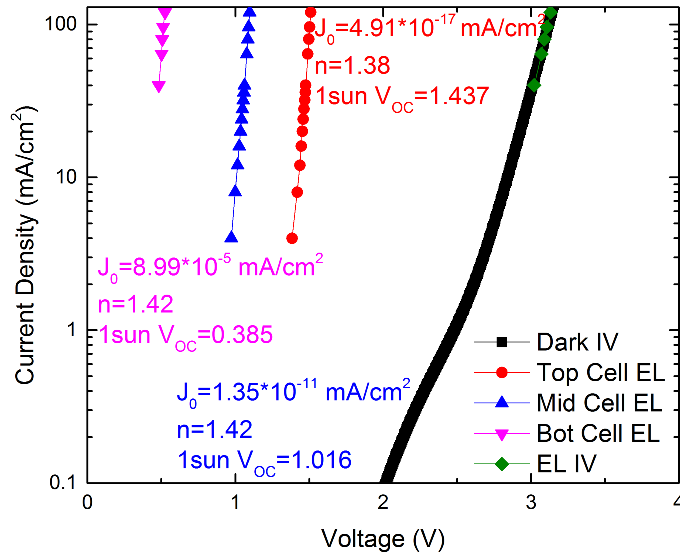

Figure 4.16: Current-voltage characteristics of top, middle, and bottom subcells as well as of the full 3J device calculated from EL and EQE measurements. The black curve a dark-IV measurement used to calculate δV. The green diamonds are the sum of the three subcell voltages calculated from EL.

The EL-IV method was applied to the QDSC by treating QD emission as defect mediated recombination which, in conventional GaAs solar cells, is nonradiative. This does

not ignore the dark current through the QDs as every carrier that recombines through a QD detracts from the intensity of the luminescence from GaAs band to band recombination. The assumption works experimentally because the internal voltage is heavily dependent on emission energy and emission through the QDs occurs at significantly lower energies than through the GaAs bulk so while the intensities may be similar, integrating across the entire subcell EL instead of just using the GaAs peak EL doesn't make a significant difference in extracted subcell voltage. I am currently conducting experiments on single junction devices with QDs and QWs in order to determine how the method applies if the QD/QW EL intensity is much greater than the GaAs band to band EL intensity.

The internal subcell voltage is determined by the emission energy and radiative efficiency of the highest energy emission peak for the subcell. Figure 4.17 compares the IV characteristics calculated from EL of both the control and QD 3J devices. Relatively little change was seen in intensities of top and bottom cell, resulting in little change in IV characteristics. The inset in Figure 4.17 presents a close-up look at IV characteristics of only the GaAs subcells. At injection currents below three suns, the emission intensity from the GaAs band-band transition was higher in the QDSC than in the GaAs control cell, resulting in a higher calculated subcell voltage, but EL intensity trended with a diode ideality factor closer to n=1 while the GaAs control subcell had a measured diode ideality factor of n=1.42, suggesting that the QDs play a role in suppressing SCR recombination leading to a higher luminescent efficiency at low injection currents. The control cell would exhibit higher open-circuit voltages at concentrations greater than three Suns.

Using the spectral reciprocity relationship, equation 4.1, absorption strength and emission strength are compared in Figure 4.18. The ratio of bulk material emission to nanostructure emission shows the relative strength of the two recombination pathways.[59]

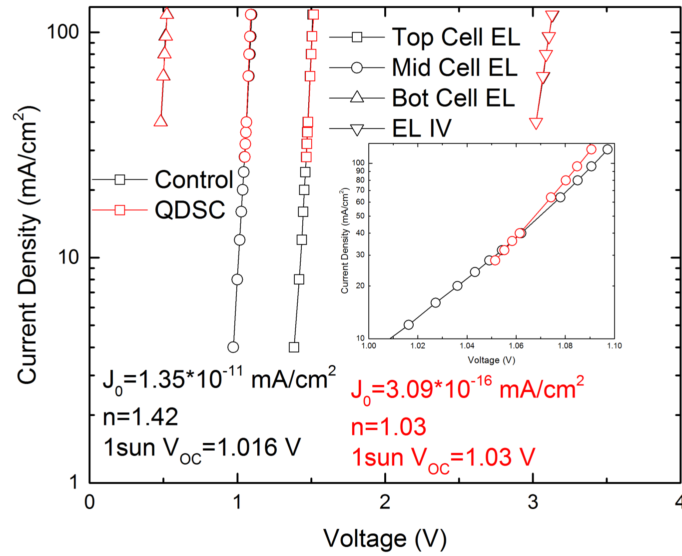

Figure 4.17: IV characteristics of control and QDSC 3J devices derived from EL and EQE spectra. Control cell characteristics are shown in black and QDSC characteristics are shown in red. The inset shows a comparison between control and QD-containing GaAs subcells.

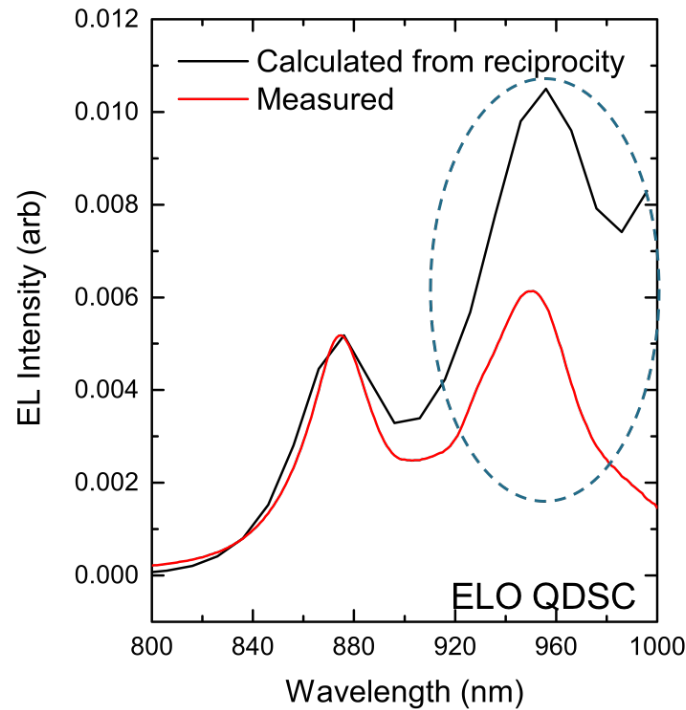

Figure 4.18: EL spectrum calculated from QE curve and reciprocity relationship. Measured EL in red, and calculated EL in black.

4.5 Radiation Tolerance of QD Enhanced Triple Junction Solar Cells

4.5.1 Modeling of Radiation Tolerance of IMM3J Solar Cells

Due to the superior performance and expected higher radiation tolerance of the conventional, thin-emitter designed triple junction solar cell, it was down-selected to from the

aforementioned designs for a study into radiation effects. Devices with 10 and 20 QD superlattice periods were grown.

Before modeling the inclusion of QDs and QWs in the InGaAs subcell, A triple junction device model was developed in Sentaurus TCAD, a physics based semiconductor device simulation software package. Calibration of the device model was done by comparing the simulated current-voltage and external quantum efficiency to a triple junction ELO IMM solar cell at BoL and EoL. For the modeled device, ELO templates on GaAs substrates with pre-grown In(Al)GaP top cells were sent from Microlink Devices Inc. to Rochester Institute of Technology where the GaAs subcell was overgrown. Samples were then sent to Microlink Devices for growth of the metamorphic buffer and $In_{0.3}Ga_{0.7}As$ subcell and for ELO and fabrication. Demonstration of high quality overgrowth is important because overgrowth will be employed for the addition of QWs and QDs in the InGaAs subcell.

Devices were modeled with a 1.2 μm In(Al)GaP subcell and 3.6 μm GaAs and InGaAs subcell with GaAs tunnel junctions connecting each subsequent cell. Devices were then fabricated via ELO for IV and EQE measurements. It was then irradiated with $2x10^{15}$ 1MeV e^{-}/cm^{2} and electrical characteristics were remeasured. The design is not optimized for EoL conditions but the thick base design assists in fitting material damage coefficients.

Current-Voltage characteristics are shown in Figure 4.19 along with modeled IVs in Synopsis Sentaurus^{TM} TCAD. Solid lines show BoL results while dotted lines show EoL results. Starting with BoL, the experimental device had an open circuit voltage (V_{OC}) of 2.93 V, a short circuit current density (J_{SC}) of 15.41 mA/cm^{2}, and an AM0 efficiency of 28% at BoL while the simulated device had a V_{OC} of 2.89 V, a short circuit current density (J_{SC}) of 15.35 mA/cm^{2}, and an AM0 efficiency of 28%. Accuracy in subcell characteristics were verified via EQE measurements.

Figure 4.20 is a comparison between experimental and simulated EQE at beginning of life. EQE was integrated across the AM0 spectrum to calculate an EQE integrated J_{SC}. The experimental In(Al)GaP, GaAs , and InGaAs subcells integrated EQE are 17.1, 15.4, and 15.6 mA/cm^{2} respectively. Simulated subcell integrated EQE are 16.26, 15.2,

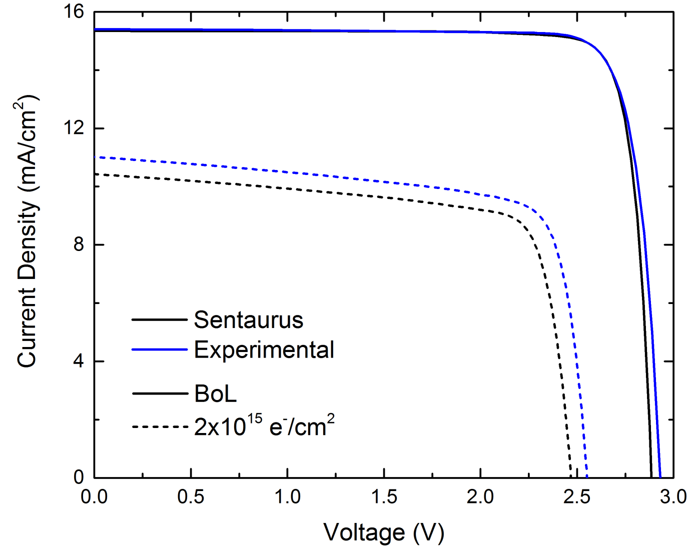

Figure 4.19: AM0 IV characteristics of 3J ELO IMM at BoL and EoL after 1MeV electron irradiation.

and 16.68 mA/cm^2 respectively. Disagreement between top cell measured and simulated EQE is due to variation in ARC thickness.

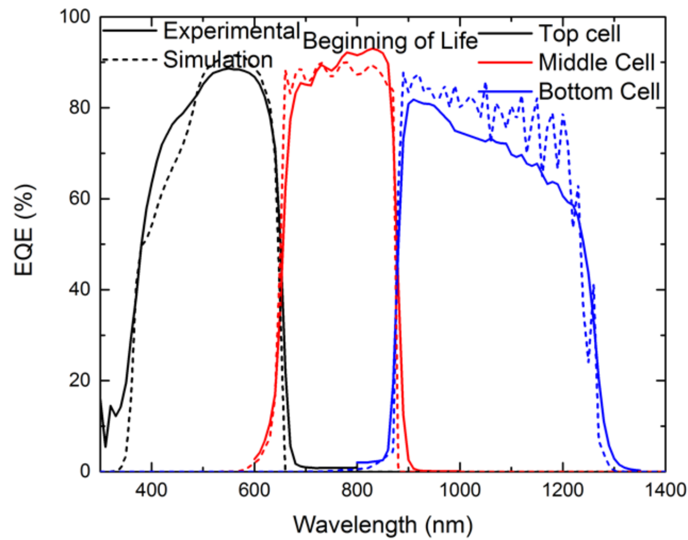

Figure 4.20: BoL experimental and simulated EQE characteristics of each subcell in 3J IMM solar cell.

Returning to Figure 4.19, the experimental device had a V_{OC} of 2.55 V, a J_{SC} of 11.03 mA/cm^2, and an AM0 efficiency of 15.3% at EoL while the simulated device had a V_{OC} of 2.47 V, a short circuit current density (J_{SC}) of 10.42 mA/cm^2, and an AM0 efficiency of 14.1%. EoL EQE measurements and simulations are shown in Figure 4.21.

The experimental subcell integrated EQE at EoL are 15.3 mA/cm^2, 11.6 mA/cm^2, and 11.2 mA/cm^2 respectively. Simulated subcell integrated EoL EQE are 14.2 mA/cm^2, 12.4 mA/cm^2, and 9.4 mA/cm^2 respectively. Experimental damage coefficients were found to be $3{\times}10^{-7}$ for In(Al)GaP, $1{\times}10^{-8}$ for GaAs, and $5{\times}10^{-7}$ for InGaAs. The largest difference between measured and simulated EQE is in the top cell, and is driven by estimated optical parameters for the Microlink window material.

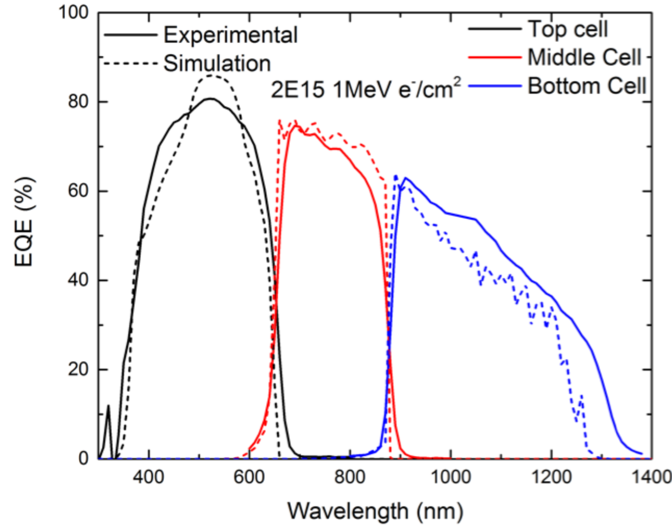

Figure 4.21: EoL experimental and simulated EQE characteristics of each subcell in 3J IMM solar cell.

4.5.2 Measurement of Radiation Tolerance of QD Enhanced IMM Triple Junction Solar Cells

A series of experimental devices with the structure modeled above in 4.5.1 were grown consisting of a control cell without QDs, a set with a 10 period superlattice of strain balanced QDs, and a set with a 20 period superlattice of strain balanced QDs. Figure 4.22 shows the current-voltage characteristics of the series of samples. Adding a 10x QD superlattice resulted in a 0.54 mA/cm^2 increase in J_{SC} and a 20 mV reduction in V_{OC} resulting in an overall net efficiency increase. Increasing the QD superlattice layer count to 20x resulted in no further increase in current, suggesting that under these test conditions, the devices become J3 current limited. Because precise isotypes matching structures grown in this study weren't available to calibrate the solar simulator against, an approximate calibration was used by measuring single-junction $InGaP_2$ and GaAs solar cells. Spectral responsivity measurements are required to investigate more closely the impact of adding QDs and whether or not adding more layers of QDs is beneficial.

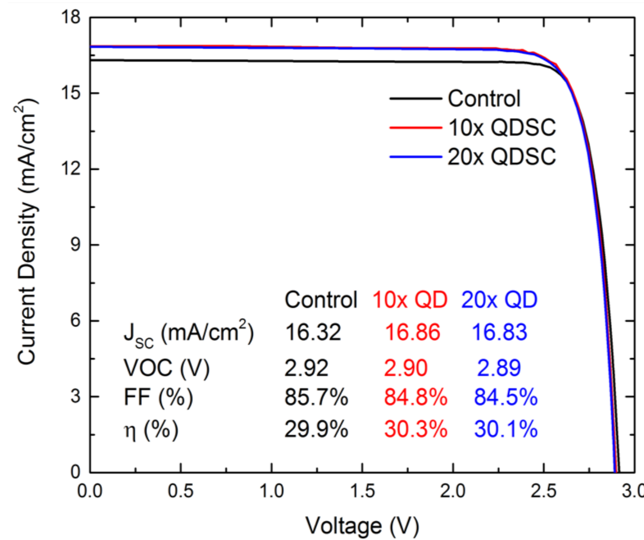

Figure 4.22: BoL 1-sun IV Characteristics of IMM 3J Control, 3J with 10xQD enhanced J2, and 3J with 20xQD enhanced J2.

EQE, calculated from spectral responsivity measurements is shown in Figure 4.23a and subcell J_{SC} calculated by from spectral responsivity and the AM0 spectrum is shown below each subcell. In these devices, J1 is current rich with approximately 6% overfill,

while J2 and J3 are closely current matched. Thinning J1 or slightly increasing the bandgap would be required for a better current match, allowing for approximately 2% relative increase in BoL efficiency. Slight spectral mismatch between the solar simulator and the AM0 spectrum would result in a trade-off between current limiting subcells. Figure 4.23b shows J2 EQE only and has sub-band absorption broken out showing 0.22 mA/cm^2 current enhancement per 10 QD layers. No degradation was seen in either the J2 base or J3, which is grown after the QD superlattice, providing further evidence that the strain balanced superlattice isn't a source of crystalline defects. The integrated J_{SC} further suggests that the 20x QDSC should be J2/J3 current matched with proper solar simulator calibration, but to take advantage of further current increases in J2, a reduction in effective J3 bandgap would be required which would bring the IMM triple junction design closer to that of the ideal detailed-balance triple junction design.

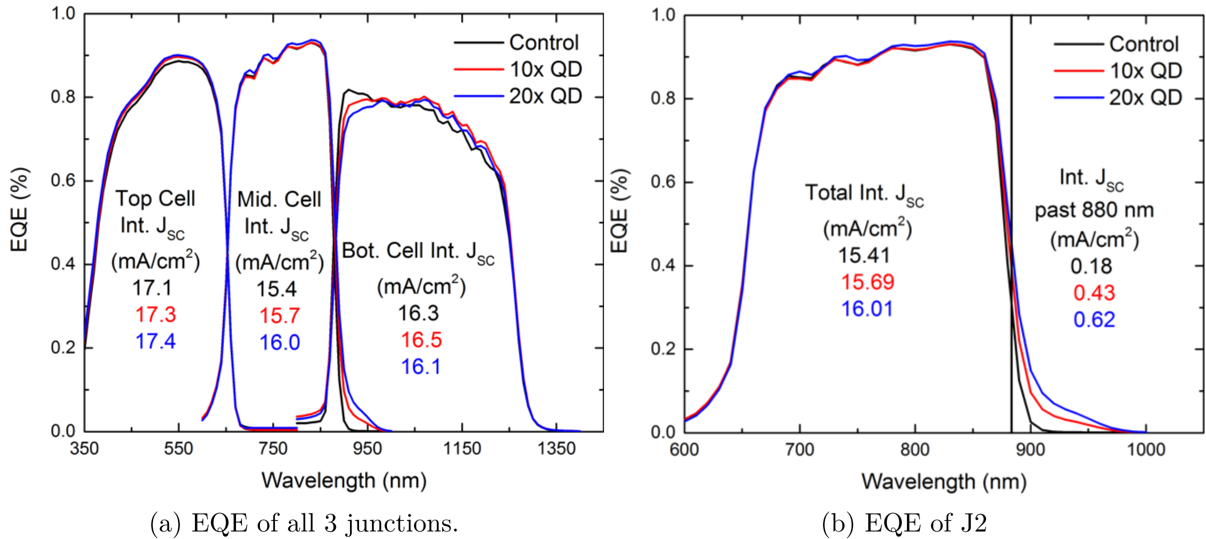

(a) EQE of all 3 junctions.

(b) EQE of J2

Figure 4.23: BoL EQE Characteristics of IMM 3J Control, 3J with 10xQD enhanced J2, and 3J with 20xQD enhanced J2.

A set of each: control, 10x, and 20x QD superlattice samples were irradiated in an electron beam facility to a range of 1MeV electron fluences from 10^{14} e^-/cm^2 to 2x10^{15} e^-/cm^2 with 10^{15} e^-/cm^2 being a typical end-of-life (EoL) fluence for geosynchronous orbits. Irradiation was performed at NeoBeam in Middlebury, Ohio. Samples were mounted on direct bond copper substrates with silver paint and a sample set consisting of

two samples of each was assembled on a silicon wafer for each target fluence. Fluence was monitored by integrating current measured via a farraday cup, and the sample stage was moved back and forth through the beam path in order to improve uniformity of exposure and mitigate heating. The steady-state temperature, measured via thermocouple was 34°C.

After irradiation, 1-sun IV measurements were taken on all exposed samples along with a full set of unexposed monitor samples in order to ensure consistency in calibration. Remaining factors were calculated by dividing post-irradiation IV characteristics by the pre-irradiation IV characteristics. Remaining factors are plotted in Figure 4.24. A few of the samples were shunted during the handling process and were screened out. The greatest difference seen in IV characteristics was in fill factor degradation where the control cell retained 97% BoL fill factor while the 10x QDSC retained 77% BoL fill factor and the 20x QDSC retained 90% BoL fill factor. The increase in fill factor degradation can be explained by the wider *uid* region required to incorporate QDs becoming more resistive as defects are generated, but the 20x QDSC, requiring an additional 15nm per superlattice repeat unit would seen an exacerbated fill factor degradation. No clear trend is seen in other IV characteristics. Since the greatest degradation from irradiation seen was in J_{SC}, spectral responsivity was remeasured.

Figure 4.25 is an example triple junction EQE curve measured from the sample set irradiated to 2.2x10^{10} MeV/g (2x10^{15} 1MeV e^-/cm^2). J1 and J3 show equivalent degradation for the entire sampleset, but J2 shows increased degradation in the bulk collection region of the device, which is primarily driven by absorption in the base of the diode. Since a voltage and light bias is already required to measure spectral response in the triple junction devices, the J2 bias isn't independently controllable, making it difficult to deconvolve the effects of carrier transport through the depletion region from bulk material degradation.

Focusing on just the QD enhanced J2, EQE at three fluences along with the BOL characteristic curve are shown in Figure 4.26. The progression of the QE curve shape from a flat top to a negatively sloped top is characteristic of base degradation, while a positive

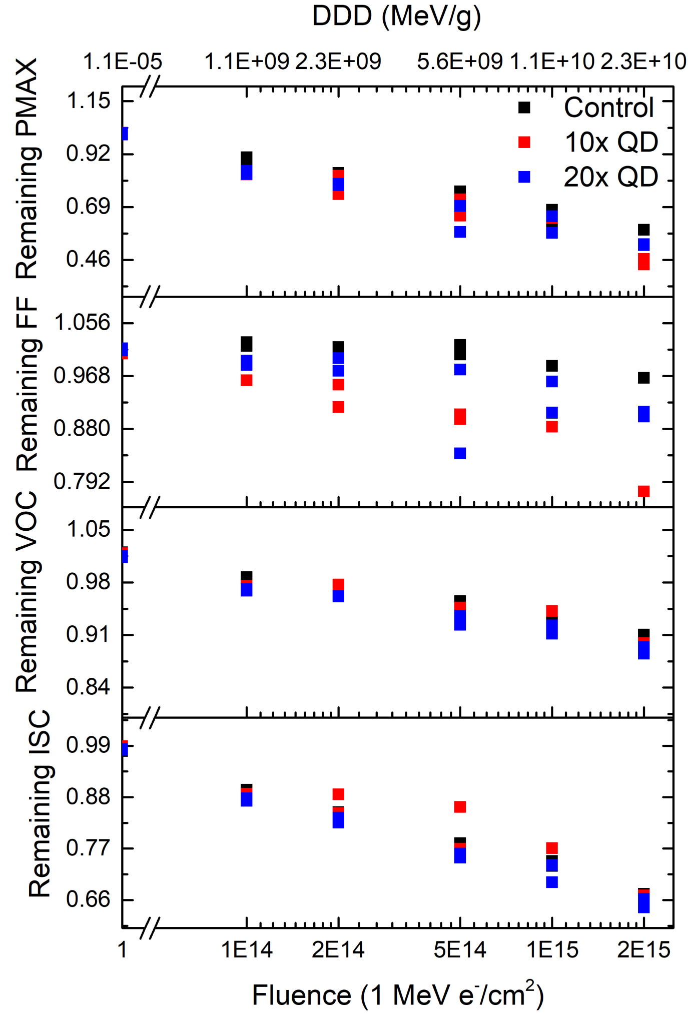

Figure 4.24: Remaining factors of Control, 10xQDSC, and 20xQDSC after irradiation with 1MeV electron beam.

slope is characteristic of emitter, or in a multijunction device where the subcell sees a filtered spectrum, depletion region degradation. Since, in an inverted cell architecture, the QDs are grown before the base, it's conceivable that the starting base material quality could be lower, but it is unlikely that the QDs are degrading the base of the cell because that would be seen at BoL in V_{OC}. The hypothesis that the QDs are causing a carrier transport problem after irradiation is supported by the degradation in fill factor seen in Figure 4.24.

In order to succinctly plot relative current retention of each device on a single plot, remaining EQE was extracted at three wavelengths, representing spatial absorption in

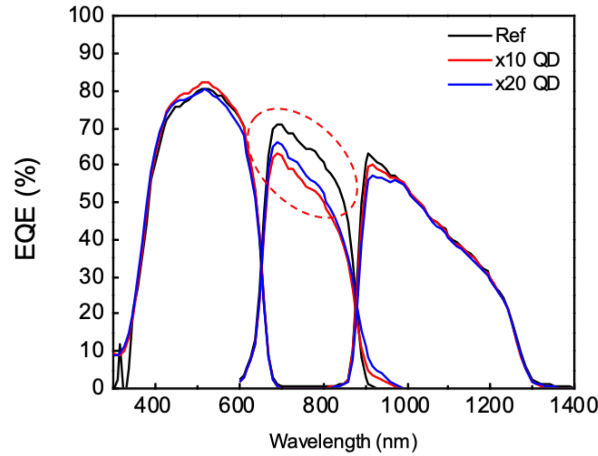

Figure 4.25: EQE of all 3 junctions at a 1MeV electron fluence of $2.2\text{x}10^{10}$ MeV/g

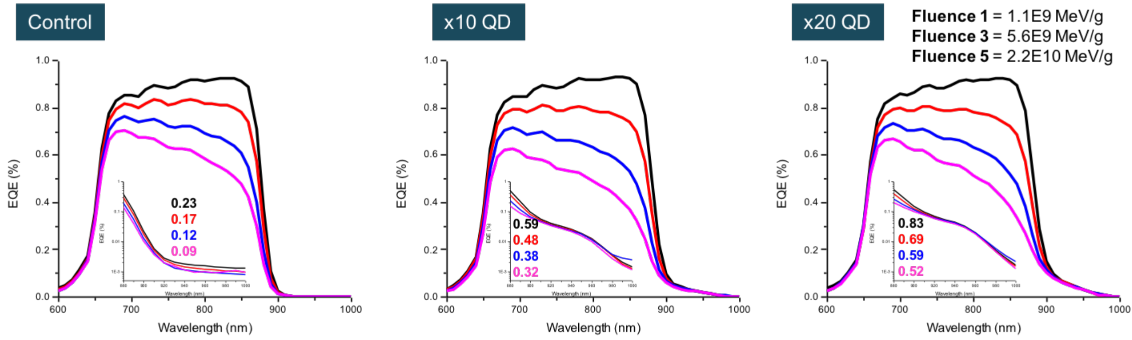

Figure 4.26: J2 EQE characteristics at BoL and at increasing particle fluences for control cell, 10x QDSC, and 20x QDSC.

the devices. 690 nm light is primarily absorbed in the emitter and depletion region as the absorption coefficient is high. 830 nm, being close to the GaAs band edge is absorbed primarily in the base of the device, and 940nm, being below the GaAs bandgap is primarily absorbed in the QD region. The resulting plot is shown in Figure 4.27. 690 nm remaining factor, shown in black show little spread, especially among the control and 20x QDSC. At 830nm, a gap is consistently seen in remaining EQE between the control and QD containing devices. Finally, little to no degradation is seen in the QD region at 940nm. In order to fully take advantage of the radiation tolerance of the QD region, carrier transport from base to emitter would need to be addressed, either through higher doping in the base, possibly doping of the barrier layers in the QD superlattice, or a

reduction in the electron barrier between base and emitter via use of heterojunctions.

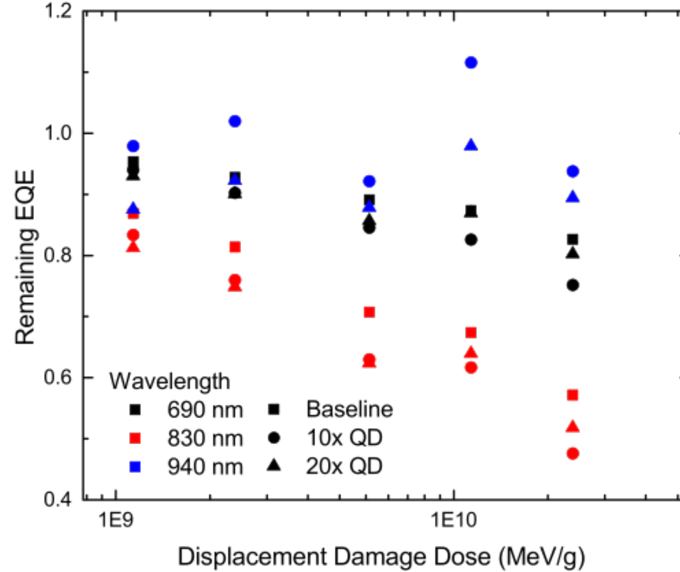

Figure 4.27: Remaining EQE vs DDD at 690nm (black), 830nm (red), and 940nm (blue) shown for control, 10xQDSC and 20xQDSC J2.

In summary, InAs/GaAs quantum dot superlattices were employed to increase current in J2 of an IMM triple junction solar cell. A current enhancement was measured with a 10X QD superlattice in light IV, and a further current enhancement was seen in EQE with a 20x QD superlattice, but further current enhancement in LIV was not measured because samples were J3 current limited under the calibration used. Minimal voltage reduction was measured because because the dominant recombination pathway remained as the GaAs band to band transition as seen in Figure 4.18. Overall J2 current retention improvement was not seen post irradiation due to reduction in collection of carriers generated in the base of the devices, but no degradation in current collection from the QDs was seen out to a 1 MeV electron exposure of 2x10^{15} 1 MeV e^{-}/cm^{2}. Since in some cases the devices in this section were current limited by the InGaAs subcell the next section is an investigation of bandgap engineering of a 1eV subcell.

4.6 Nanostructure Enhanced 1eV Subcell

4.6.1 Characterization of Test Structures and Simulation of Triple Junction Solar cells with MQW Enhanced 1 eV Subcell

In this section, the inclusion of quantum wells and quantum dots in a 1eV InGaAs IMM subcell is simulated and experimental single junction isotypes and triple junction devices. Characterization of InAs QD test structures grown on an InGaAs metamorphic template were presented by Slocum et al. [60] Optical parameters from an 8-band k·p simulation were used and will be presented in the device modeling section. Because the predicted absorption coefficient of InAs QDs on InGaAs is so low, QWs were downselected as the focus of this work. The first growth challenge in incorporating superlattices into a metamorphic subcell is in characterization of change in strain. Surface roughness increases when growing metamorphic subcells. Strain balanced superlattices are generally characterized via HRXRD by fitting interface interference fringes. As surface roughness increases, these interference fringes are dampened. In the case of the metamorphic subcell, no interference fringes were seen in a $< 224 >$ RSM, so instead in-situ curvature measurements in growth were used to strain balance the subcell on the assumption that as long as strain wasn't accumulating in the superlattice, substrate bow wouldn't change during the growth of the superlattice.

Growth was again performed at RIT on metamorphic templates provided by Microlink Devices. A strain-balanced InGaAs superlattice was grown by modulating the indium partial pressure in the growth chamber to form compressive wells and tensile barrier layers. Figure 4.28 shows readbacks from Aixtron's reflectance and pyrometry system. In black is sample curvature, red, the temperature readback, and in blue is reflectance, with oscillations due to thin film interference during growth. The top plot in 4.28 is from a tensile superlattice sample grown on the compressive InGaAs grade, resulting in a positive change in curvature from an average In partial pressure of $3.6x10^{-3}$mbar. The bottom plot shows a compressive superlattice resulting in a negative change in curvature with an average In partial pressure of $3.8x10^{-3}$mbar. Interpolating between these two

points gives a target average In partial pressure of $3.7x10^{-3}$mbar for a strain-balanced superlattice. Also important to note is that the reflectance off the surface did not degrade during the growth of the superlattice suggesting that material quality is being maintained and that the surface isn't hazing during growth due to strain.

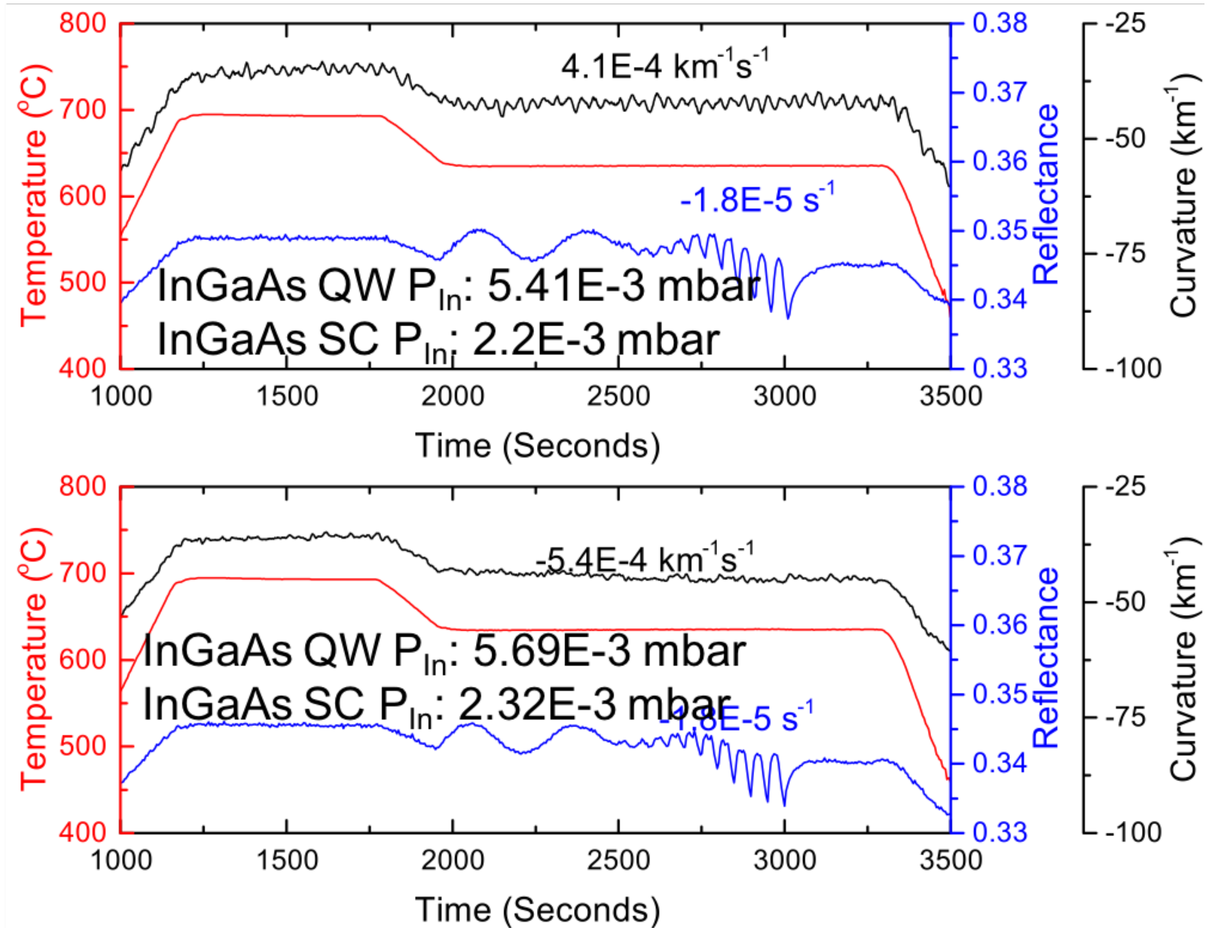

Figure 4.28: Reflectance, temperature, and curvature readbacks from growth of metamorphic QW superlattices.

NextNano++, a commercial Schrodinger-poisson solver that employs an 8-band k·p model, was used to calculate band structure and absorption coefficient of InGaAs quantum wells. Thicknesses and compositions of 7nm $In_{0.4}Ga_{0.6}As$ QWs in 9nm $In_{0.2}Ga_{0.8}As$ barriers were selected via photoluminescence (PL) characterization with conditions that minimize wafer curvature measured with in-situ reflectance monitoring. Figure 4.29 shows experimental PL from grown test structures along with calculated absorption. QW ground state absorption strength is predicted to be around 5000 cm^{-1}, nearly 250

times the predicted absorption strength of InAs QDs on InGaAs.

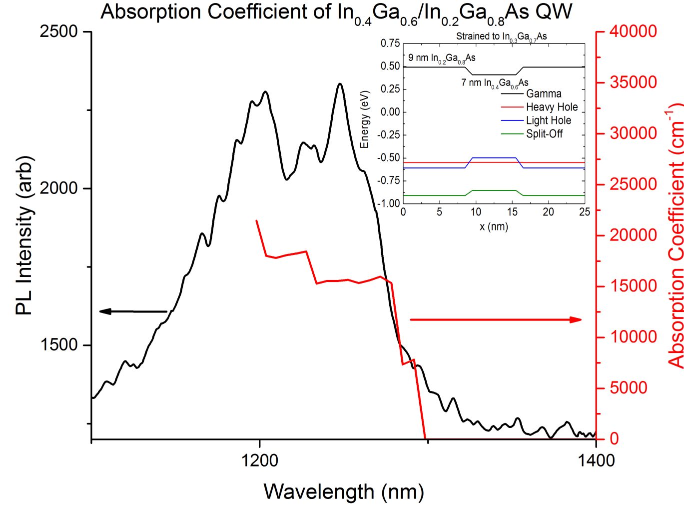

Figure 4.29: Experimental photolumeniscence of 7nm $In_{0.4}Ga_{0.6}As$ QW in 9nm $In_{0.2}Ga_{0.8}As$ barrier grown on relaxed $In_{0.3}Ga_{0.7}As$ plotted along with absorption coefficient of QW calculated in NextNano. The inset shows the calculated band structure.

Test structures were grown in an Aixtron 3x2" close-coupled showerhead metallorganic chemical vapor deposition (MOCVD) reactor with standard metallorganic precursors and AsH_3.

InAs and InGaAs 40x multi-quantum well structures were added to an i-region in an InGaAs subcell in the Sentaurus TCAD 3J model with layer and barrier thicknesses consistent with [60] for QDs and the QW simulation presented above along with calculated absorption coefficients. Layer thicknesses were then optimized to closely current-matched EoL conditions. The EoL optimized control device had a 300 nm In(Al)GaP top cell, a 1200 nm GaAs subcell, and a 1200nm InGaAs subcell. The top cell thickness was increased to 350 nm for the EoL optimized devices with QWs and QDs and both designs employed a 100nm InGaAs emitter and a 1100 nm InGaAs base cladding the QD/QW region. Structures are shown in Figure 4.30

Figure 4.31 shows resulting current-voltage characteristics. A V_{OC} reduction from nearly 2.5 V to 2.4 V from the addition of interfaces and an i-region into the InGaAs subcell, which represents a significant portion of the EoL V_{OC} of a 1 eV subcell, however the reduction of the V_{OC} is compensated for via J_{SC} enhancement. The predicted EoL

Figure 4.30: Optimized Control Cell, cell with QDs in J3, and cell with QWs in J3 resulting in best performance at a simulated 2x10^{1}5 e^{-}/cm^{2} fluence.

efficiency for the three devices is 17.24%, 18.31%, and 17.85% for control, QW, and QD respectively. The increase in EoL efficiency for the QW device represents a 6% relative efficiency enhancement.

End of life EQE for QD and QW containing subcells are shown in Figure 4.32 with J1 in black, J2 in red, and J3 in blue. For this design, both J1 and J2 are optically thin, transmitting in-band light to the subcell below. The control cell, shown in dotted lines requires the thinnest J2 in order to transmit light that is collected in the front of J3, closer to the junction where collection is maintained at EoL. In both designs including QDs and QWs in J3, the optimized base thickness is reduced to account for collection in the QD and QW regions respectively which provides an ancillary benefit of improving the overall radiation tolerance of J3 beyond the benefit of sub-band absorption and collection.

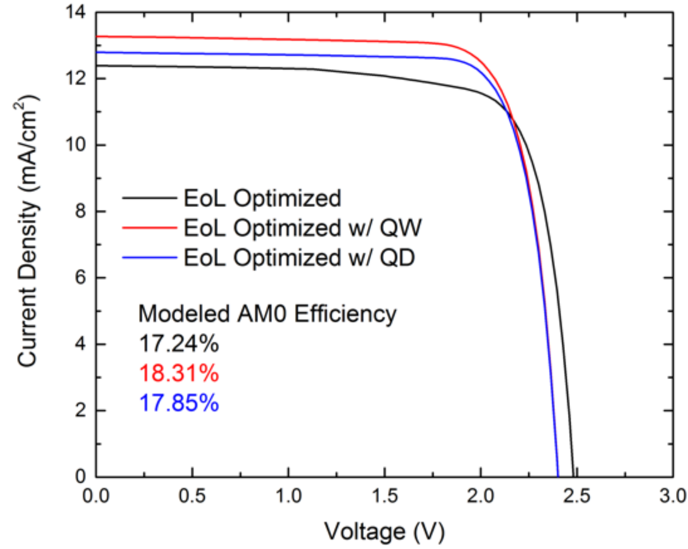

Figure 4.31: Simulated JV characteristics of 3J IMM solar cells with a modeled irradiation of 2x10^{1}5 e$^-$/cm^2. The control design is shown in black, a device containing QWs in the InGaAs subcell in red, and a device containing QDs in the InGaAs subcell in blue.

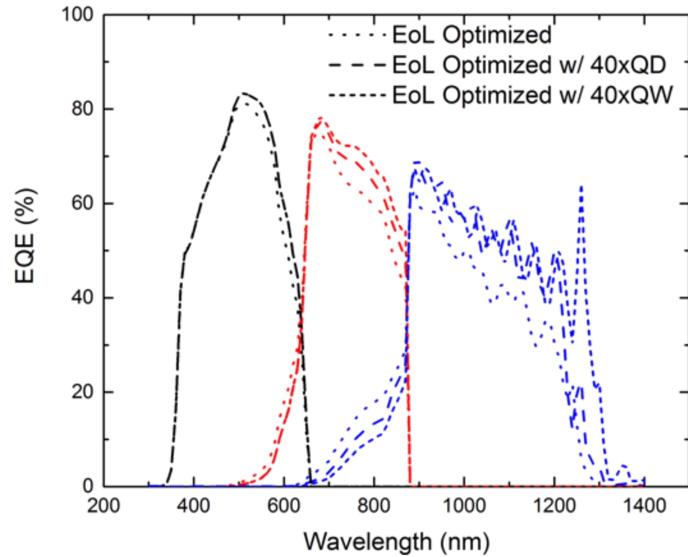

Figure 4.32: Simulated EoL EQE of 3J IMM solar cells with a modeled irradiation of 2x10^{1}5 e$^-$/cm^2. J1 is shown in black, J2 in red, and J3 in blue with dotted lines representing the control, long dashes representing the structure optimized for 40x QD layers in J3 and short dashes representing the structure optimized for 40x QW layers.

Finally, the J3 structure from above showing the best performance, the MQW superlattice structure was combined with a QD bandgap engineered J2 and a reflective back contact which allows for further current enhancement from inclusion of the MQWs as well as a thinning to half the original J3 base thickness with the doubling of the optical

path length through the cell. As a result of the improved current retention from thinning J3, the optimum base thickness in the GaAs J2 increases from 900 nm, as in Figure 4.30 to 1200 nm, shown in Figure 4.33 and the optimized InGaP subcell thickness increases from 300nm to 350nm. Because of the optical path length enhancement from the rear reflector, the number of QW layers in J3 was reduced to 10x.

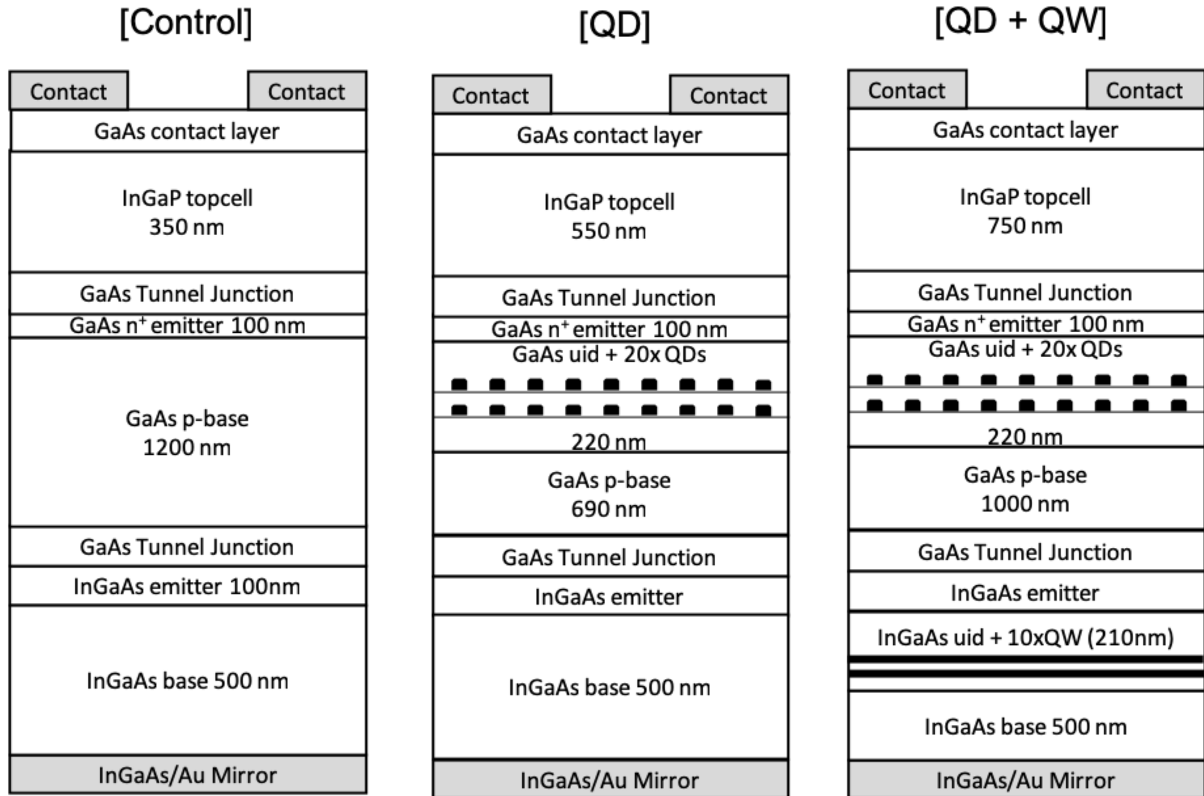

Figure 4.33: Optimized Control Cell, cell with QDs in J2, and cell with QDs in J2 and QWs in J3 resulting in best performance at a simulated $2x10^15$ e^-/cm^2 fluence.

Figure 4.34 shows beginning and end of life EQE for the three structures shown in Figure 4.33. The most noticeable change from Figure 4.32 is how much more square the J3 QE is at EoL, which is driven by the aggressive thinning enabled by a reflective back contact. A second characteristic of note is the lack of J2 degradation in the case where QDs are included by J2 but no QWs are included in J3 because the modeled QD absorption allows for a thin J2 as well. Enhancing the current in J3 through the inclusion of QWs necessitates an increase in J2 base thickness from 690nm to 1000nm which drives a slight reduction in the subcell radiation tolerance.

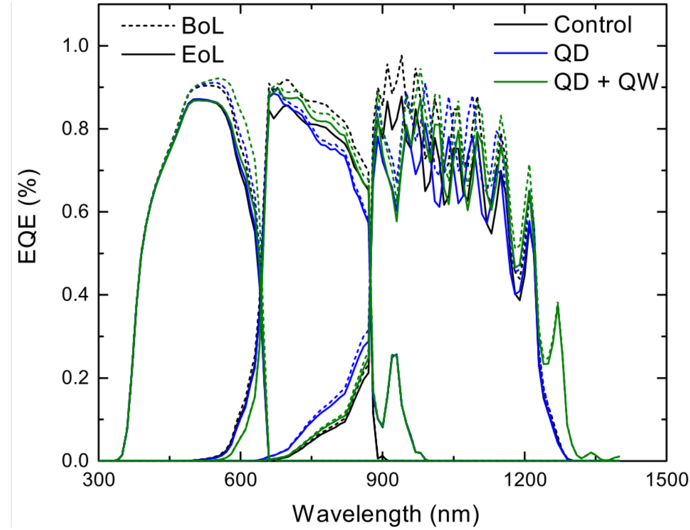

Figure 4.34: EQE of Control cell design (black), optimized cell including 20x QD superlattice in J2 (blue), and optimized cell including 20xQD superlattice in J2 and 10 QW superlattice in J3 (green). BoL EQE is shown with dotted lines and EoL with solid lines.

Simulations with structures shown in Figure 4.33 were run at increasing simulated 1MeV electron fluences to generate J_{SC} curves vs DDD for the three structures, which is shown in Figure 4.35. Because J3 is thinned to take advantage of the rear reflector, it is the most radiation hard subcell so the optimized structure was to be J3 current limited at BoL. Because of this, the structure containing QWs in J3 had the highest BoL J_{SC}, and the structure containing QDs in J2 had the lowest BoL J_{SC}. Around 2×10^9 MeV/g, J2 in the control cell has lost enough current to become current limiting and the control cell shows the sharpest knee as it has the most radiation soft J2. At increasing fluences, J_{SC} in the sample containing only QDs in J2 and the sample containing QDs in J2 and QWs in J3 begin to converge as the structures become more J2 limited. At extremely high fluences, like those required for Jupiter missions, it might be advantageous to forgo the inclusion of MQWs in J3 or to employ a thinner base in J2 in order to maintain a higher J_{SC} at DDDs greater than 2×10^9 MeV/g.

With the modeled benefits of including nanostructures in both J2 and J3, the next section focuses on testing of bandgap engineered 1eV cells in both single and multi-junction platforms. Developing the reflective back contact is outside the scope of this work so is not included in the upcoming section.

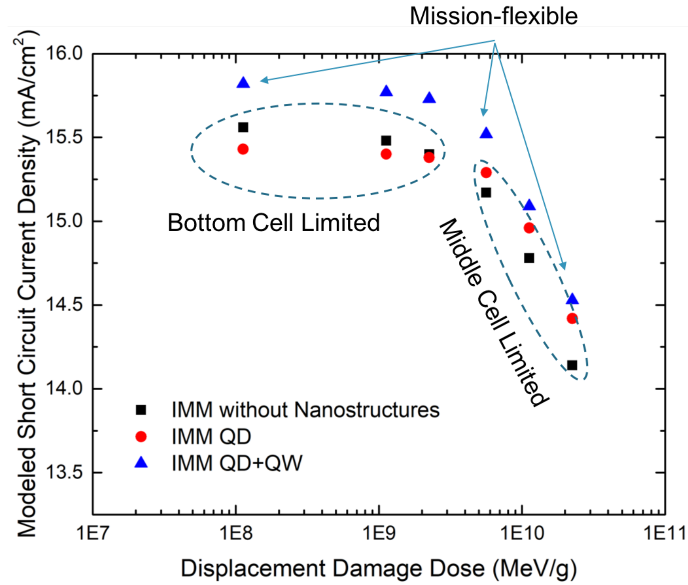

Figure 4.35: Simulated triple junction J_{SC} for optimized control cell design, optimized design employing QDs in J2 only, and an optimized design employing QDs in J2 and QWs in J3.

4.6.2 Characterization of Nanostructure Enhanced 1eV Subcells

Optimized superlattice growth parameters from subsection 4.6.1 were used to grow a 1eV isotype with quantum wells. Readbacks from the growth are shown in Figure 4.36. A 40x strain balanced quantum well superlattice was grown in order to maximize current enhancement along with a 600 nm undoped layer in the control cell to match the *uid* region thickness of the QWSC. Curvature is relatively unchanged throughout the growth of the QW superlattice, however reflectance did degrade during growth. Samples were sent back to Microlink for base, back surface field, and contact growth and for fabrication. In tandem, a full triple junction with a 10x MQW superlattice was grown. The lower well count is expected to generate less current, but is considered a more conservative approach in case the inclusion of strain balanced superlattice is unsuccessful and degrades material quality.

After process, samples were returned to RIT for test. No ARC was deposited. Starting with the single junction devices, 1-sun AM0 current-voltage characteristics can be seen in Figure 4.37. The control sample had a V_{OC} of 0.445 V, leading to a W_{OC} of 0.555, which is high, but in line with what is expected for a triple junction cell with a 2.9V

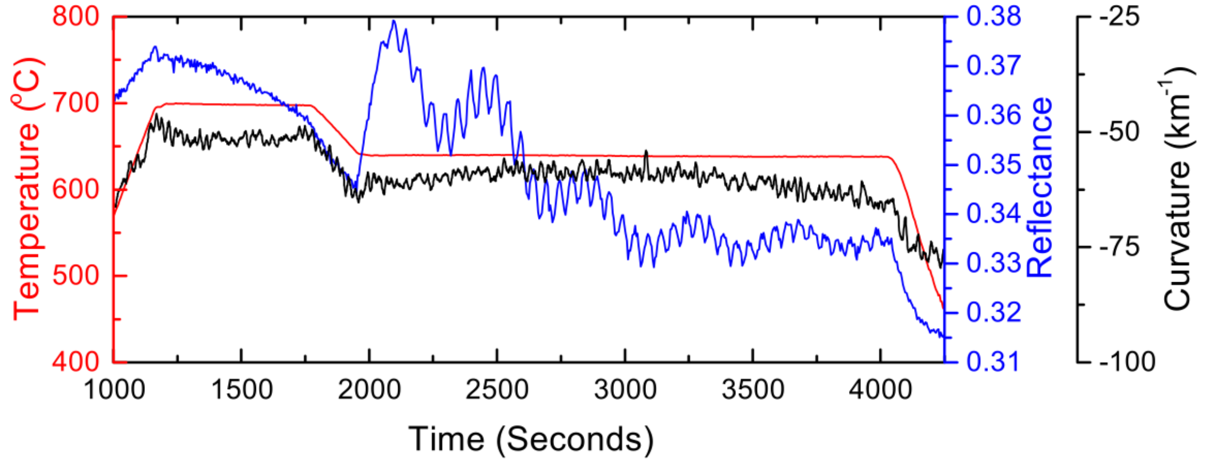

Figure 4.36: Curvature, reflectance, and temperature readbacks from the growth of J3 isotypes showing minimal deflection changes during growth. Curvature is shown in black, reflectance in blue, and temperature in red.

V_{OC}, verifying that the overgrowth in J3 at RIT was closely lattice matched with the endpoint of the metamorphic buffer grown at Microlink. However, the inclusion of the MQW superlattice results in a V_{OC} reduction to 0.205 V and a J_{SC} reduction from 16.1 to 12.9 mA/cm^2 along with what appears to be shunting of the subcell.

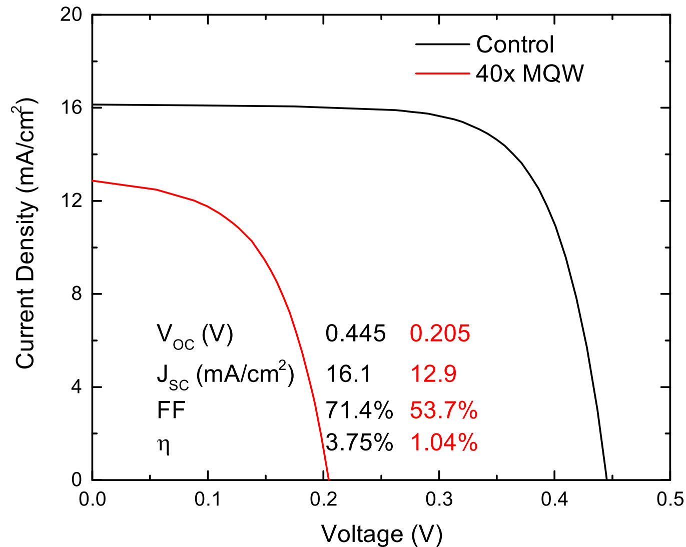

Figure 4.37: Comparison of Light IV of Control and 40x MQW 1 eV inverted single junctions.

Spectral responsivity was measured and EQE is shown in Figure 4.38. Solid lines are measured EQE and dotted lines are modeled. The negative slope in EQE is indicative of degradation in the base of the device, and the required change in base minority carrier

lifetime to achieve a good fit of the shape of the QE curve is a factor of 10 from 100 ps to 10 ps, but the model does not take into account the effects of heterointerfaces and carrier scattering from the wider bandgap barrier layers required to strain balance the superlattice. In order to assess the effects of energy barriers on collection, a carrier collection efficiency measurement can be performed where the device is reverse biased for the QE measurement to increase the electric field through the depletion region.

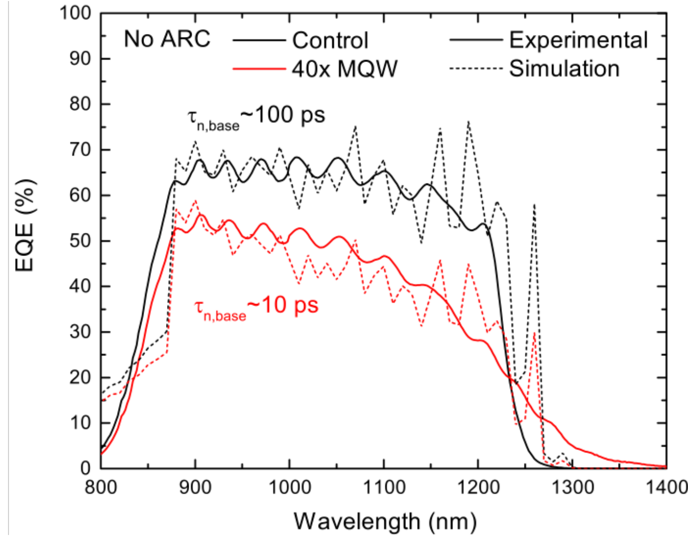

Figure 4.38: Measured and modeled EQE of 1eV inverted single junction with extracted minority carrier electron lifetime

Figure 4.39 shows measured EQE with increasing reverse bias across the MQW device. at -1V reverse bias, there is an 8% increase in base-side collection and an 11% increase in emitter-side collection, however the EQE curve isn't 'squared up' to more closely match the shape of the EQE curve measured on the control device, suggesting that there is a recombination center, either due to bulk material degradation or a problematic interface. Since triple junction devices were grown with fewer QWs, LIV and EQE from that sample set can be used to determine whether or not degradation of J3 tracks with the amount of strain-balanced material included in the structure.

Since the full triple junction only contained a 10x MQW superlattice instead of the 40x MQW superlattice, bulk degradation induced by the growth of the QWs should be suppressed. Figure 4.40 is a comparison in LIV characteristics between the IMM 3J

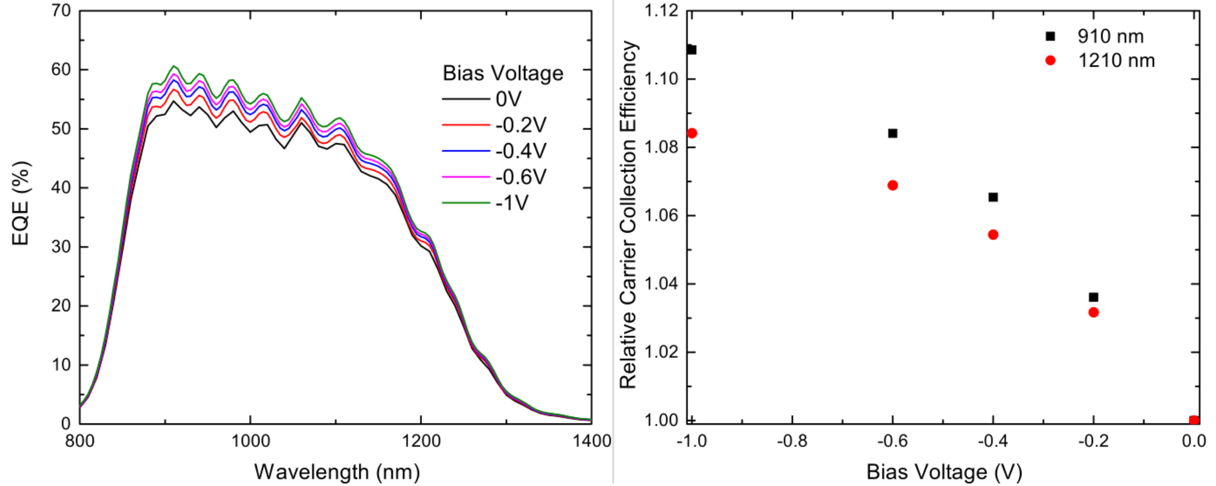

Figure 4.39: EQE measured with a reverse bias in order to enhance electric field through MQW region of device (left) and relative CCE at 910 nm (emitter side) and 1210nm (base side) with varying applied reverse bias.

containing the 10X QW superlattice in J3 and the corresponding control cell with a *uid* region in J3 grown at RIT. The control cell had a V_{OC} of 2.87V, which is a slight reduction compared to the control cell shown in Figure 4.22 where the entirety of J3 was grown at Microlink, but is in-line with expected performance. The sample with a 10X MQW superlattice, however, had a V_{OC} of 2.64 V, a 230 mV reduction compared to the corresponding control cell. This compares closely to the results in Figure 4.37 which showed a 240mV degradation in V_{OC} as compared to its corresponding control cell. The nearly 10-point reduction in fill factor and soft knee in the LIV curve around 2V suggests that J3 is shunted and the measured current increase probably is not coming from the quantum wells in J3.

Figure 4.41 shows EQE of the control and QW containing devices. Neither J1 nor J2 show any degradation which rules out effects from annealing during the growth of J3, and J3 again shows a negative slope characteristic of base degradation. Spectral response integrated across the AM0 spectrum results in an integrated J_{SC} reduction in the MQW containing sample to 69% of that of the control J3 and if J3 was not shunted, a reduction in the triple junction J_{SC} would be expected as J3 would be the current limiting subcell.

Figure 4.42 is a comparison of the J3 subcell QE in Figure 4.41 with the single junction results in Figure 4.38. The single junction QE results are shown in solid lines, and the

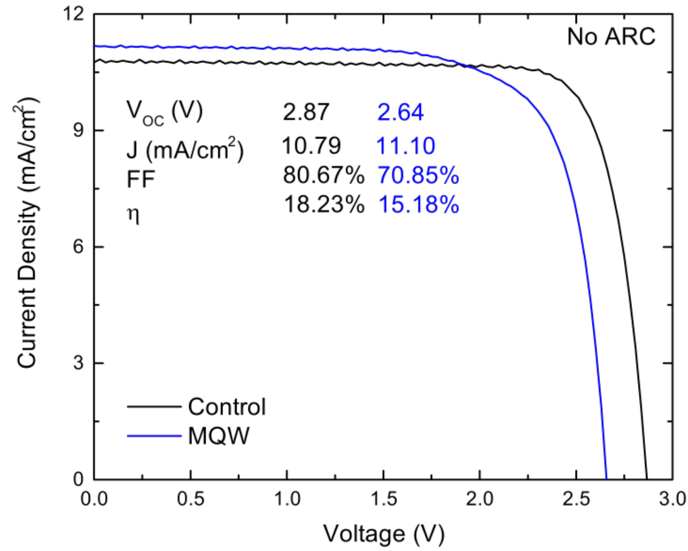

Figure 4.40: IV characteristics of full triple junction solar cell with 40x InGaAs QW enhanced 1eV subcell.

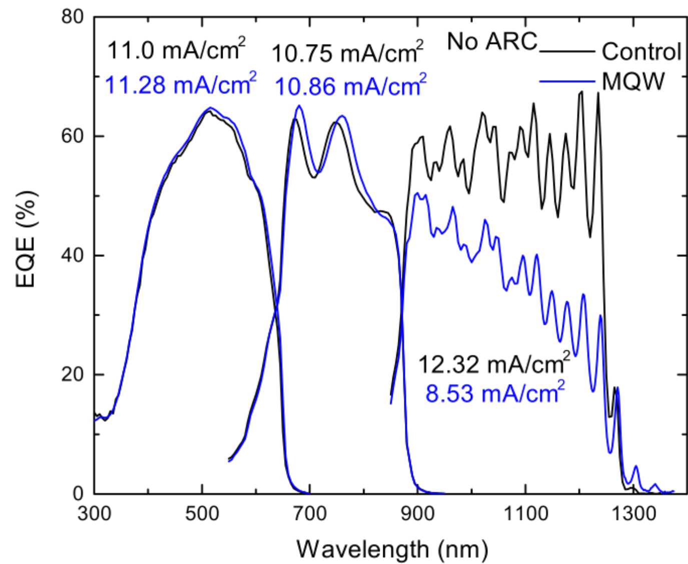

Figure 4.41: EQE of IMM triple junction solar cells. The black curve is the control device and blue is from the sample containing a 10X MQW superlattice in J3. Integrated subcell J_{SC} is labeled for each corresponding subcell.

triple junction subcell measurements are in dotted lines. Starting with the control cell, the slight reduction in EQE and the change in fringe spacing and intensity is due to cavity effects and increased reflection from the inclusion of the full triple junction layer stack. Fringes in both sample sets would be suppressed with inclusion of an ARC. Importantly, both sets of control cells have a flat, square EQE curve shape indicative of a maintenance

of base material quality. Interestingly, the 40x MQW single junction shows no more EQE degradation than the subcell containing the 10x MQW superlattice.

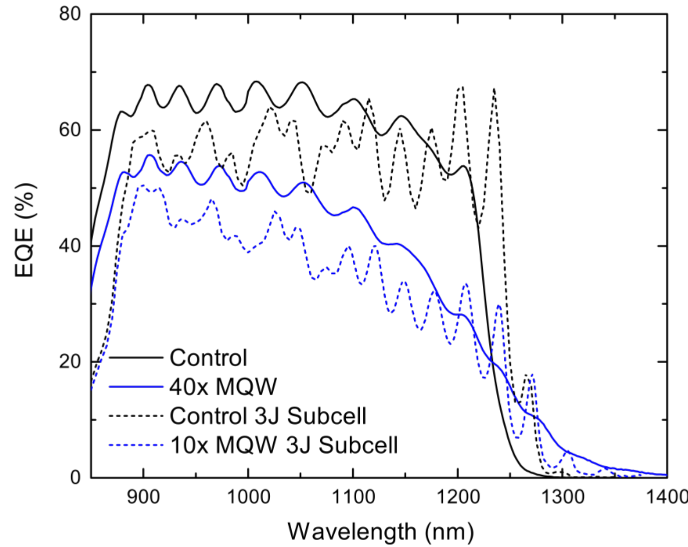

Figure 4.42: Comparison between triple junction subcell and single junction 1 eV solar cell EQE. Control cells are in black and QW containing cells are in blue. Solid lines are single junction results and dotted lines are multijunction results.

While not ideal, this is a promising result because it demonstrates that MQW stacking isn't driving a degradation in material quality since a 40x MQW superlattice resulted in the same degradation of a 10x MQW superlattice. Reducing barrier height by removing the strain compensation layers in a low-periodicity (<10 layer) superlattice or switching the polarity of the single junction n-p to a p-n cell would assist in determining the mechanism causing the reduction in base collection.

4.7 Conclusions

In this chapter, a BoL efficiency enhancement was measured from the inclusion of 10x and 20x InAs/GaAs strain compensated QD superlattices in the GaAs subcell of a triple junction IMM solar cell. Electrical results were used to calibrate a Sentaurus TCAD triple junction model in order to develop radiation hard device designs and to model potential benefits from adding QDs to the GaAs J2 in an IMM structure and from adding QWs to the 1 eV InGaAs J3 in an IMM structure. Lastly single and triple junction devices were

demonstrated with InGaAs QWs in the InGaAs subcell resulting in sub-band current collection, however an apparent minority carrier electron injection problem limited base collection and resulted in an approximate 200meV reduction in V_{OC}.

Figure 4.11 shows the results of an approach at developing an accurate Sentaurus TCAD simulation of a triple junction solar cell. Later in this chapter, experimental results were presented for the two device designs shown in Figure 4.10 and subcell internal voltages were extracted as shown in Figure 4.17. These results need to be incorporated into the device model so it can be used as a tool to further improve the design and in order to assess the impact that transitioning to either a front heterojunction will have on the conventional design or a rear heterojunction on the thick-emitter design.

Chapter 5

Modeling of Effects of Using Polycrystalline Substrates for Low Cost III-V Photovoltaics

5.1 Introduction

Current high-efficiency state-of-the-art photovoltaic (PV) technology depends upon crystalline semiconductor substrates such as gallium arsenide, indium phosphide, or germanium. Such substrates contribute to the bulk of the semiconductor material in current high efficiency photovoltaics as the active layers need only be a few μm thick, which is detrimental to the primary figures of merit for both terrestrial and space PV; cost specific power, and mass specific power respectively. Techniques such as epitaxial lift-off and substrate recycling have been proposed to make lighter and cheaper PV, but do not completely eliminate the need for expensive substrates, and still limit the starting lattice constant for epitaxy to that of a material where a crystalline substrate is available. A recrystallized virtual substrate also has the potential benefit of posessing an arbitrary lattice constant, not constrained to the common Si, GaAs, Ge, or InP.

Molybdenum foil substrates offer a compelling alternative to conventional substrates because the coefficient of thermal expansion is comparable to that of conventional semiconductor materials [61], but the material grown on such a substrate will be polycrystalline with arbitrary crystal orientations and grain sizes. It has been demonstrated that large ($\sim$1 mm) Ge grains can form on metallic or ceramic substrates. [62][63] As such, it is important to understand the effects of crystallinity and of nucleation properties of epitaxy on substrate material. One specific challenge to nucleating GaAs on Ge is the formation of antiphase domains (APDs), or regions of antisite defects in nucleation of

of a contiguous film on the host substrate. As evidenced by the adoption of Ge based multijunction PV for space, this problem has been solved for growth of GaAs on c-Ge substrates.

Venkatasubramanian *et al.* have demonstrated that APD formation is not an insurmountable problem on polycrystalline substrates by growing and fabricating a 20% efficient (AM1.5G) GaAs solar cell on a Ge substrate[64]. However, an enhanced undetstanding of the impact of nucleation defects can assist in understanding degradation mechanisms between monocrystalline c-Ge and c-GaAs substrates, and between c-Ge and polycrystalline poly-Ge substrates [61]. Looking forward, it is even more critical to understand material nuclation problems in diagnosis of degration mechanisms in situations involving fully virtual substrates, such as micro/nanocrystalline Ge formed on mismatched materials, such as molybdinum wafers [65] or on vapor-liquid-solid phase semiconductor growth on virtual substrates[66].

The focus of this work is to develop a comprehensive spectral responsivity (SR) and current-voltage (IV) model for crystalline and polycrystalline GaAs solar cells grown on arbitrary substrates, accounting for intragrain material quality as well as the effects of grain size, boundary recombination velocities, and nucleation induced defects. This work looks at a comparison of samples grown on (100) c-GaAs substrates and poly-Ge substrates. The final work presented at the PVSC will include samples grown on c-GaAs/Ge and poly-GaAs/Ge with a variety of buffer thicknesses to specifically look at APD suppression and nucleation characteristics.

5.2 Experimental

In order to better assess the impacts of polycrystallinity and nucleation on Ge, a total of four *pin* $In_.01Ga_.99As$ solar cells were grown via MOCVD in a Veeco D125 on a selection of crystalline and polycrystalline GaAs and Ge substrates. The first set, GaAs grown on single and poly-crystalline GaAs provided a baseline for comparing only the effects of the presence of grain boundaries on electrical performance. The second set, (In)GaAs, with

around one percent In in order to lattice match to Ge, grown on single and poly-crystalline Ge provided a baseline for comparing only the effects of APDs through comparison of c-GaAs and c-Ge devices as well as a final device grown on polycrystalline Ge, used to verify model accuracy when both extended defect types are present.

An AXT (100) c-GaAs substrate with a 2° offcut to [110], a poly-GaAs substrate from CMK, and a (100) c-Ge subsrtate with a 6° offcut to [111] from Umicore, and finally a poly-Ge substrate from Umicore were used in this study. Both polycrystalline substrates had a primary grain orientation of (111), verified via XRD. The Germanium substrates were annealed at 700^oC under hydrogen ambient before a low-temperature GaAs nucleation layer and 1μ m (In)GaAs buffer in an attempt to suppress APD formation on arbitrary grain orientations[67] in order to promote double-step nucleation and prevent the formation of APDs. Samples were grown with a p-on-n polarity with a 500 nm emitter with a doping of $1x10^{18}$ cm^{-3}, 2 μm base with a doping of $1x10^{17}$ cm^{-3}, and 300 nm uid region. The crystalline and poly-GaAs solar cells were grown simultaneously with no surface treatment beyond a 200 nm GaAs nucleation layer.

Spectral responsivity (SR) was measured in order to calculate an external quantum efficiency (EQE), and IV characteristics were measured under 1-sun AM0 conditions. A minority carrier drift-diffusion model, based on work by Hovel & Woodall [6], was developed and used to fit EQE and AM1.5G IV of these devices. Specific inclusions in the model will be discussed in the next section.

5.3 Device Modeling

The basis for the model is a series of carrier transport equations that can be used along with absorption data to model current collection, first presented by Hovel[6] and shown in Section 2.2. The value of such a model is that it allows for extraction of material quality parameters such as surface recombination velocities, minority carrier diffusion lengths, and minority carrier lifetimes when fitting to measured data.

A minority carrier drift-diffusion model was calibrated by fitting minority carrier diffusion lengths in a crystalline GaAs control cell, and used to predict grain boundary induced degradation in poly-GaAs solar cells. The polycrystalline minority carrier diffusion lengths are predicted by combining the bulk minority carrier diffusion length with the grain boundary influenced minority carrier diffusion length calculated using equation (5.1) below.

$$L_g = \sqrt{\frac{Dd_g}{4S_g}} \tag{5.1}$$

Where D is the minority carrier diffusion constant, (S_g) is the interface recombination velocity (assumed to be $5x10^6$ cm^2/s), and d_g is the grain size. The total minority carrier diffusion length (MCDL) in each layer were calculated from the summation of the inverse of the partial minority carrier diffusion lengths. Minority carrier diffusion lengths were also used to calculate reverse saturation currents of a ideal $n = 1$ diode (I_{01}) in order to generate current-voltage (IV) curves. The V_{OC} of the GaAs control cell was used to fit a nonradiative $n = 2$ term and to determine the grain boundary space-charge region reverse saturation current component (I_{02}). Grain boundary dependent nonradiative recombination in the quasi-neutral regions was calculated with the following system of equations [68]:

$$J_s = \begin{cases} \frac{qn_iS_gW_g}{d_g/4}, & d_g >> W_g \\ \frac{qn_iS_gW_g(d_g-W_g)}{d_g^2/4}, & d_g > 2W_g \\ qn_iS_g, & d_g < 2W_g \end{cases} \tag{5.2}$$

where n_i is the intrinsic carrier concentration of GaAs and W_g is the depletion width between grains and is a function of the barrier height from grain boundary traps and background doping so W_g can is calculated as

$$Wg = \frac{2\epsilon V_d}{qN} \tag{5.3}$$

where N is the region doping and V_d is the barrier between grains which is assumed to

be 0.2 V [68]. The system of equations in Equation 5.2 is essentially a geometric factor for how much of the grain is depleted from band bending at the boundary.

One challenge with growing devices even on c-Ge is the formation of APDs, a defect nucleating at the interface where epitaxy nucleates with the wrong ion, leading to ordering faults in the subsequent GaAs. Since APDs act as extended one-dimensional scattering centers that propagate out-of-plane, they can be treated similarly to threading disloactions, degrading lifetime in a material as a function of the aerial density using the following equation[69]:

$$\tau_{APD} = \frac{4}{\pi^3 D \rho_{APD}} \tag{5.4}$$

which is effective because it is a geometric factor based on minority carrier diffusivity and takes a sheet density of carrier scattering centers that propagate out-of-plane. This is fed back into the total MCDL of the drift-diffusion model as lifetime is related to MCDL through the diffusion coefficient of the carrier in the material in question.

Minority carrier diffusion equations can also be used to more precisely estimate electrical characteristics of a solar cell. The diode reverse saturation current due to recombination in the quasi-neutral regions of the emitter and base:

$$J_{p/n} = q\frac{D_{p/n} n_i^2}{N_{doping} L_{p/n}} \frac{sinh\frac{t-w_i}{L_{p/n}} + \frac{S*L_{p/n}}{D} * cosh\frac{t-w_i}{L_{p/n}}}{cosh\frac{t-w_i}{L_{p/n}} + \frac{S*L_{p/n}}{D_{p/n}} * sinh\frac{t-w_i}{L}} \tag{5.5}$$

Where $D_{p/n}$ is the diffusiton constant for the minority carrier in the layer, S is the surface recombination velocity between the layer and corresponding window layer, $L_{p/n}$ is the minority carrier diffusion length, t is the film thickness, and w_i is the depletion width into the film. $J_{0,Diff}$ is the sum of J_p and J_n.

Reverse saturation current due to recombination in the space-charge region, which is also impacted from APDs[69] can be modeled as

$$J_{0,SCR} = q\frac{n_i w_{i,emitter+base}}{(\tau_p \tau_n)^{1/2}} \tag{5.6}$$

where τ are the final minority carrier lifetimes, including all recombination mechanisms, and w is the depletion width calculated from the built-in potential and growth

structure in the case of inclusion of a *uid* region. Finally, the total diode current in the solar cell is given by

$$\begin{aligned} J = -J_{SC} + J_{0,Diff}(e^{q\frac{V-JR_s}{k_B T}} - 1) \\ +(J_{0,SCR} + J_S)(e^{q\frac{V-JR_s}{2k_B T}} - 1) + \frac{V + JR_S}{R_{SH}} \end{aligned} \tag{5.7}$$

which includes reverse saturation currents from all recombination pathways outlined above as well as parasitic series and shunt resistances that can be either estimated or extracted from experimental devices.

5.4 Results

An IR camera was used to take EL images of the two devices grown on polycrystalline substrates and representative images are shown in Figure 5.1. Grain boundaries, acting as nonradiative recombination centers are dark. The spacing between grid fingers is approximately 400 μm. A rough estimate of the average grain size for the two samples is 400 μm for the poly-GaAs substrate and 200 μm for the poly-Ge substrate which isn't a major difference other variables such as minority carrier lifetime, doping or diffusivity can vary across orders of magnitude. Furthermore, these grain sizes put both samples in the regime where grain size is significantly larger than grain boundary depletion region.

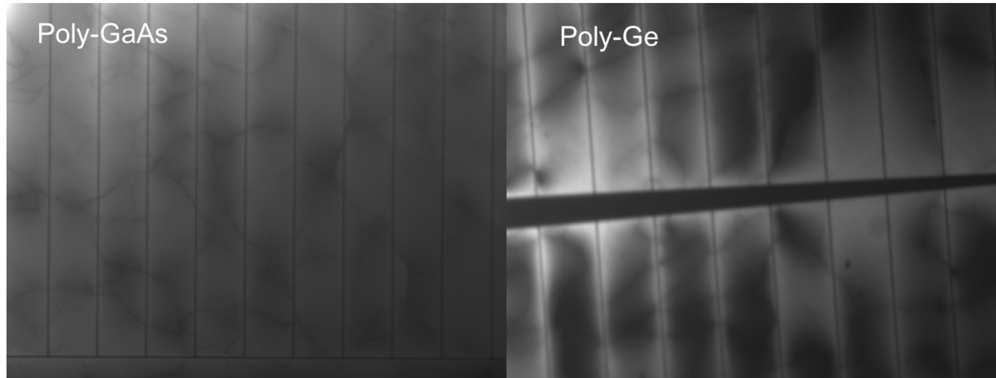

Figure 5.1: Electroluminescence Images of GaAs solar cells grown on poly-GaAs substrates (left) and poly-Ge substrates (right)

While minority carrier lifetime can be estimated via IV curves, the first step was to fit

the EQE because the shape of the EQE curve provides information on emitter and base lifetimes separately. High short wavelength collection with a tapered tail near the band edge indicates poor base collection but strong emitter collection, while a decrease at short wavelengths with a square-like tail near the band edge indicates that the base material is good, but the emitter is degraded. Figure 5.2 is the collection of EQE curves for the four devices grown on crystalline and polycrystalline substrates. There was virtually no change in EQE between the cells grown on c-GaAs and poly-GaAs (black and green curve respectively), consistent with expectations for devices with near half-millimeter grain sizes and reflected in the modeled curves (dotted lines). the cell grown on the c-Ge substrate however, showed severe degradation across the entire spectrum. A defect density, which we're assuming nucleates from an APD, of $4x10^8$ cm^{-2} in the base is required to match the level of degradation seen in the EQE. Finally, the EQE of the solar cell grown on the poly-Ge substrate had a EQE that was much closer to that of the cells grown on GaAs, suggesting APD formation and propagation of defects was greatly suppressed. A density of $3x10^7$ cm^{-2} in the base was required to fit the experimental results which is well below the detection threshold of TEM.

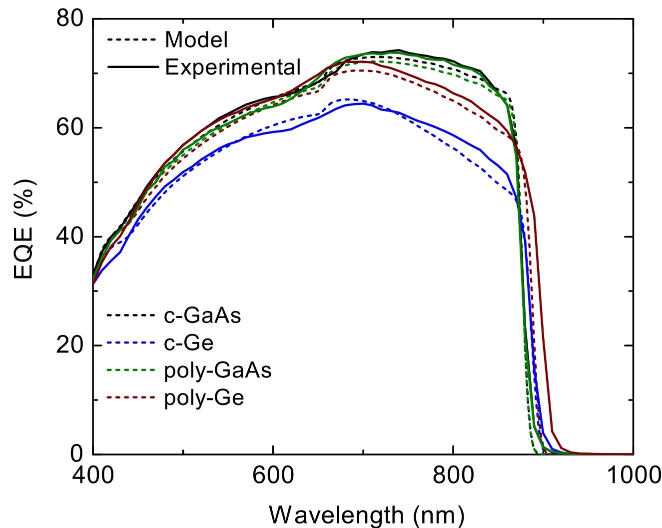

Figure 5.2: Plot of experimental and modeled EQE of the solar cells grown on crystalline and polycrystalline GaAs and Ge substrates without an ARC.

The fit parameters determined by EQE were used to fit the IV curves. Figure 5.3

plots measured and modeled AM1.5G IVs of the two sets of devices included in this study and is included to show both the one-sun experimental results and the relative closeness of each device fit. Device parameters are included in Table 5.1. The device grown on the c-GaAs substrate had a J_{SC} of 19.3 mA/cm^2 and Voc of 1.04 V, in line with historic baseline GaAs solar cells under AM1.5G. The solar cell grown on the poly-GaAs substrate, shown in green had a comparable J_{SC} of 18.9 mA/cm^2, but exhibited a 100 mV drop in V_{OC} and an 8.2 point (absolute) drop in fill factor.

Material fit parameters are included in Table 5.2. Keeping the intragrain lifetimes constant and applying a 400 μm grain size, consistent with grain sizes measured via microscope, drops the open circuit voltage by the predicted amount between crystalline and poly-GaAs devices. The result of scattering at the grain boundaries is reduces the emitter and base MCDL from 1.6 μm to 1.4 μm. A significantly longer base MCDL is predicted for a GaAs solar cell grown on c-GaAs which suggests that material quality could be improved slightly for all devices.

Table 5.1: AM1.5G IV Characteristics of Devices Included in Study

Device	J_{SC} (mA/cm^2)	V_{OC} (V)	FF	η (exp)	η (model)	η (ARC)
c-GaAs	19.3	1.04	77.9%	15.6%	15.8%	21.5%
poly-GaAs	18.9	0.94	69.7%	12.4%	12.5%	16.5%
c-Ge	17.3	0.86	74.1%	11.0%	11.0%	14.8%
poly-Ge	19.4	0.89	68.8%	11.9%	12.5%	16.6%

Table 5.2: Fit Material Parameters and Diode Characteristics of Devices Included in Study

Device	Grain Size (μm)	Effective Emitter/Base MCDL(μm)	J$_{01}$ (mA/cm^2)	J$_{S,SCR,APD}$ (mA/cm^2)	R_S (Ω-cm^2)	R_{SH} (Ω-cm^2)
c-GaAs	-	1.6/1.6	9.5×10^{-21}	2.7×10^{-11}	3	4×10^6
poly-GaAs	400	1.4/1.4	1.2×10^{-20}	2.4×10^{-10}	4	6×10^3
c-Ge	-	0.9/0.1	8.2×10^{-20}	6.8×10^{-10}	3	4×10^6
poly-Ge	200	1.3/0.6	2.2×10^{-20}	5×10^{-10}	4	8×10^3

The solar cell grown on crystalline Ge exhibited the lowest J_{SC} and V_{OC}. While the

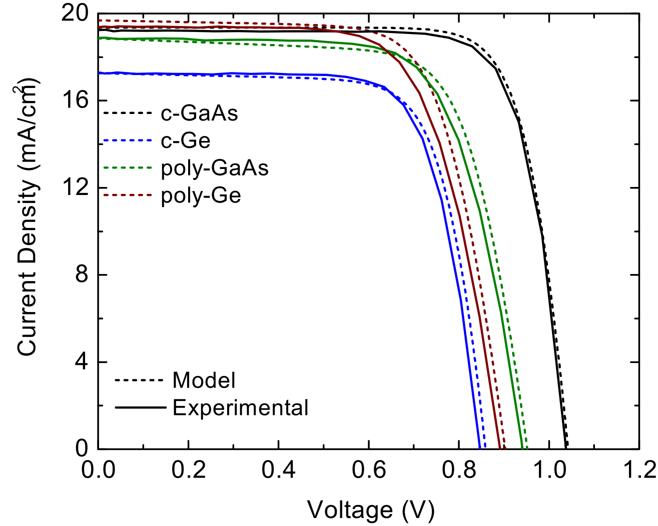

Figure 5.3: Plot showing experimental one sun AM1.5G IV measurements (solid lines) and modeled results (dotted lines) for solar cells grown on crystalline and polycrystalline GaAs and Ge substrates. No ARC has been applied.

low temperature GaAs buffer layer is supposed to provide good nucleation on arbitrary grain orientations, it did not work well on the (100) surface of the crystalline Ge substrate, resulting in a high APD density. Setting the APD density in the base at $4x10^8$ cm^{-2} resulted in a good fit for both J_{SC} and V_{OC}. The result of an APD density this high is emitter and base MCDLs of 0.9 μm and 0.1 μm respectively. Finally the device grown on the poly-Ge substrate outperformed the device grown on c-Ge because the primarily (111) oriented surface with arbitrary tilt had the effect of suppressing APD formation. While the grain size was around half the size of that from the poly-GaAs substrate. The predicted APD density in the base based on the drop in open circuit voltage and slight drop in base collection after taking grain size into account was in the low 10^7 cm^{-2}. The result of the reduction in APDs was restored carrier collection in the emitter to near that of the c-GaAs device, however collection in the base was still reduced as compared to the samples grown on GaAs due to the smaller grain size. The Poly-GaAs substrate provided a promising result because it suggested that APD formation is a problem specific to (100) substrates.

Another interesting trend that the model does not currently account for is the impact of polycrystallinity on shunt resistance. Both samples grown on polycrystalline substrates

had shunt resistances three orders of magnitude lower than the counterparts grown on crystalline substrates suggesting that the grain boundaries may act as localized shunt pathways. The reduction in shunt resistance was enough to decrease the fill factor, shown in Table 5.1 but not decrease the V_{OC}.

In order to try to extract an APD density to compare against the estimates in the model, a (220) bright field TEM was taken on devices grown on crystalline and polycrystalline Ge substrates. Figure 5.4 is an (220) TEM micrograph of the GaAs buffer grown on Ge. From the TEM image, an APD density of 1.3-$3x10^9$ cm^{-2} was measured. This is a little under an order of magnitude higher than the modeled result, but we think this is because the 1 $/mum$ buffer layer between the interface and the cell has the result of burying the defects, reducing the impact on the device layers. Electron channeling contrast imaging (ECCI) via SEM may be a better method of measuring the actual defect density in device layers.

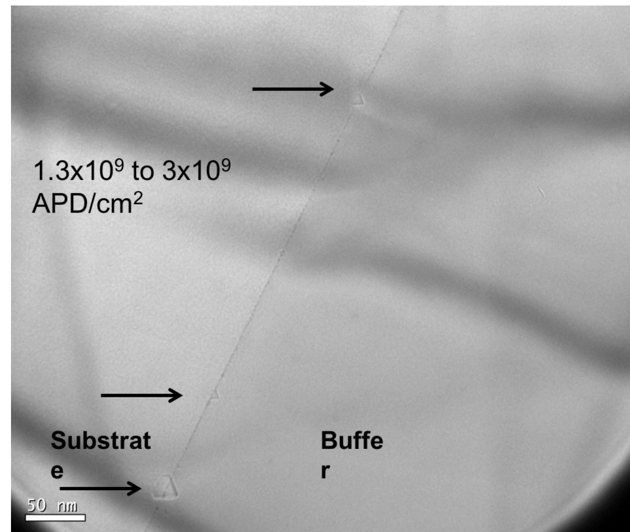

Figure 5.4: <220> TEM of GaAs nucleation layer on c-Ge substrate showing the presence of APDs. The linear density shown results in an aerial density of 1.3-$3x10^9$ cm^{-2}.

Finally, all the results were assembled together into a contour plot predicting achievable efficiency of a GaAs solar cell grown on recrystallized Ge. Figure 5.5 shows the range of efficiencies predicted for a GaAs solar cell grown on Ge with an APD density of 10^7 cm^{-2}. Grain boundary recombination velocity is shown on the y-axis and grain

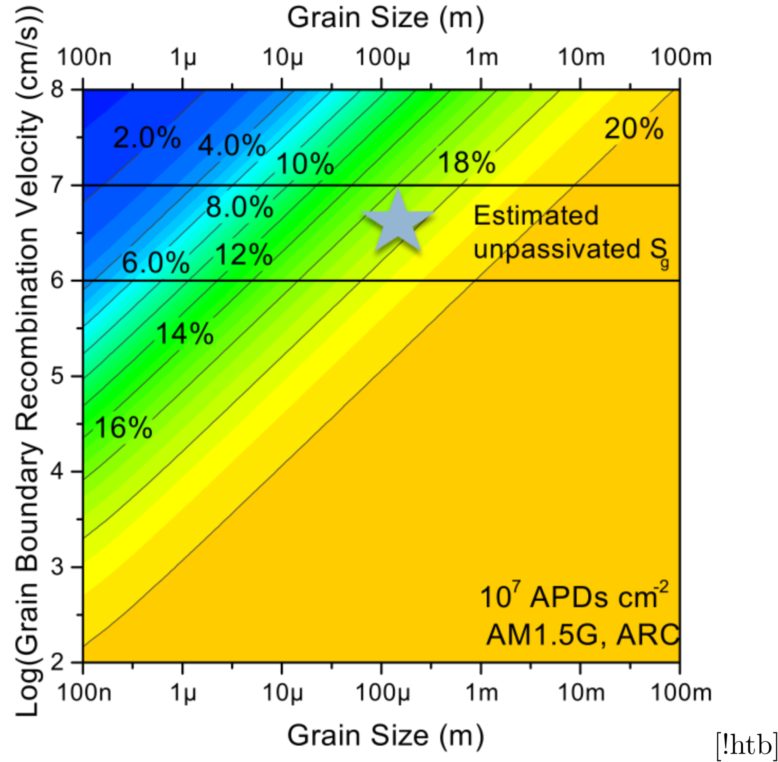

[!htb]

Figure 5.5: One-sun AM1.5G efficiency contour plot showing expected device efficiency across a range of grain sizes and grain boundary recombination velocities with an APD density of 10^7. The two horizontal bands in the plot are the expected unpassivated grain boundary recombination velocities for GaAs. The star in the plot is placed at the predicted efficiency of the GaAs cell grown on poly-Ge if an ARC was applied. The slight difference from experimental was due to the lower than expected shunt resistance seen in the cell grown on poly-Ge.

size shown on the x-axis. The device grown on poly-Ge in this work had a one-sun AM1.5G efficiency of 12.5% with a predicted efficiency of 16.6% with an ARC. The star on Figure 5.5 shows the results achieved in this study. Passivating the grain boundaries could enhance the efficiency to around 20%, for a 10% relative increase but not much more. Attempting to grow on templates with significantly smaller grains, such as 10 μm will require some sort of grain boundary passivation in order to achieve near-crystalline like device efficiencies providing us with with target parameters for recrystallized Ge templates.

5.5 Conclusions

In this chapter, a comprehensive device model for GaAs solar cells grown on polycrystalline substrates was demonstrated using a series of devices grown on single-crystalline GaAs, single-crystalline Ge, polycrystalline GaAs, and polycrystalline Ge in order to deconvolve the effects of antiphase boundaries and of crystalline grain boundaries. The benefit of this work is that the resulting contour plot shows that with grain boundary passivation, large-grain ($>100\mu m$)polycrystalline films are not needed to achieve single-crystalline like device performance. Also of note is that a (111) oriented Ge grain appears to suppress formation of APDs where polycrystalline Ge and polycrytalline GaAs grown devices had similar performance, where nuclation on single-crystalline Ge caused a performance degradation as compared to nucleation on single crystalline GaAs, a phenomenon which may be beneficial when transferring the process to sputtered or evaporated Ge films.

Chapter 6

Conclusions & Future Work

6.1 Development of Quantum Dot Intermediate Band Solar Cells

Having performed the background experiment that appears to somewhat validates the *pin* heterojunction design as shown via recovered fill factor and reduced parasitic resistances, the next step is to grow and fabricate QDSCs for a full characterisation of optical and electrical characteristics. The current heritage with QD growth via MBE is being leveraged to grow improved samples, however there are some present concerns about material quality. Feasibility of growth via MOCVD is currently being assessed, and the final work may include chatacterization of devices grown via either growth method.

While investigation of sequential absorption was performed via pump-probe spectral response measurements, electronic properties have not been fully characterized due to the poor quality of the surrounding diode. More information can be gleaned with temperature dependent IV analysis under a variety of monochromatic, dichromatic, and broadband light conditions in order to generate and characterize the effects of state filling in QDs. Without modifying the electronic structure around the QDs, the most straightforward way to look for sequential absorption or state-filling effects under broad spectrum illumination is looking at a change in light concentration.

One major question in prototype IBSC systems are the effects of carrier occupation in QDs on band structure and electrical properties of a device. Linares *et al.* [70] suggest that at low light intensities, recombination in the cell is dominated by recombination into or out of the IB. It isn't until the onset of full or near full QD occupation where cell

voltage recovery is expected to be seen. There are a few different methods of establishing a population discussed in literature. Forward biasing a diode leads to carrier injection across the junction, increasing the probability of carrier capture from a QD. The second method is by optically pumping the material, either with a broadband source, or resonantly pumping specific states with monochromatic sources. The third method is to change the fermi level around the dot via delta doping. Starting with the first method, Lu *et al.*[54] suggest that carrier occupation in QDs occuring from suppressed carrier escape from QD to CB at low temperatures results in a dark current suppression starting around 30K in the $In_{0.5}Ga_{0.5}As$/GaAs material system. The suppression reported was beyond the dark currents achievable with the GaAs control cell, presenting some interesting possibilities for the QD material system. Using the second method of generating a carrier population in QDs, Jolley *et al.* [71] demonstrated a similar phonomenon via a slightly different machanism. Instead of taking dark IV Measurements, cells were irradiated with a broadband longpass filtered IR lightsource at two different intensities, a baseline intensity, and a 1000X concentrated intensity. Photocurrent (uncalibrated spectral responsivity) was measured as a function of applied bias and scaled by relative light intensity. At high temperatures (>90K), no change in scaled photocurrent response is seen between low and high illumination conditions because carriers are able to thermally escape at a rate much greater than the capture lifetime. However, at 90K, an increase in intensity normalized photocurrent is measured under high concentration. In spite of the positive change in photocurrent, Jolley argues that the high carrier occupation leads to exciton formations which reduces the recombination lifetime, increasing interband recombination in spite of the photocurrent enhancement, which doesn't seem to agree with the results shown in the article.

The InAs/AlAsSb material system present in this chapter is unique due to the fact that there is a type-II band alignment along with significantly deeper carrier confinement. Due to the deeper confinement in QD states, the onset of carrier occupation should occur at higher temperatures than those reported for In(Ga)As/GaAs material systems. A major concern with the previous results was the relative weakness of the measured ΔSR.

A weak result is expected in the InAs/GaAs material system because the confinement depths are on the order of 200 meV, but the primary motivation to switching to the InAs/AlAsSb system was to push towards a much greater confinement depth in order to thermally separate the QD states and the conduction band. Investigating carrier occupation effects presents another opportunity to verify that the InAs/AlAsSb material system exhibits expected IBSC-like properties via a second method, and slight modifications of the optical setup may provide more evidence of sequential or two-photon absorption. An experiment similar to that in Jolley *et al.* [71] will be constructed using a broadband light source and longpass filters to look at the effects temperature and relative concentration have on bias dependent photocurrent. While Jolley *et al.* selected to illuminate the samples with a wavelength capable of pumping both interband and intraband transitions within the QDs, the material system in this study allows for more precise selection. Using a 1500 nm longpass filter, used for the ΔSR measurement allows for excitation of only the VB to QD transitions, while a 900 nm longpass filter allows for excitation both into and out of the QDs, and performing the measurement at two light concentrations can allow for investigation of carrier occupation effects.

The ΔSR measurement has been a major focus in demonstrating the IBSC concept. Two points need to be considered critically. The first is whether or not sequential absorption should be seen, and the second is whether or not what is seen is indeed sequential absorption. Okada et al.[17] suggested that they measured a ΔSR at room temperature in an InAs/GaNAs QD at room temperature, but that is not theoretically possible because the carrier escape time from InAs QDs is nearly instantaneous. It is possible to incease carrier occupation with high light concentrations, but the optical setups required to get to 1000X 1-Sun light concentration isn't compatible with the SR measurement, and generally isn't performed as a CW measurement due to the electrical power and thermal loads involved. The results presented by Antolin *et al.*[21] suggests that a two-photon effect is seen in InAs/GaAs at 6K, but the effects are dramatically reduced to near the noise floor of the measurement at 80K. The change in SR is also constantly positive throughout the entire range of the measurement, which makes me question if

it is truly sequential absorption, or if it is an effect of improving carrier collection by reducing carrier capture by the QDs. The results presented in this work look similar to Antolin's results since the SR enhancement is seen across the entire range of carrier collection.

While photoreflectance allows for location of critical points in the band structure of a material, it does not offer much assistance in extracting absorption strength. Ellipsometry, however, can assist in extracting optical properties, but requires modeling the band structure of the material which can be difficult due to ambiguity in non-luminescent critical points, such as higher energy band-to-band transitions, or nonradiative intraband transitions, such as the one that exists from conduction band to QD in the InAs/AlAsSb system. As such, photoreflectance and ellipsometry are complementary techniques for full modeling of optical properties of materials. Ellipsometry data of an InAs/AlAsSb quantum dot stack will be taken and modeled. Photoreflectance and ellipsometry are complementary techniques, which, when taken together, may provide an experimental absorption model for the QD material.

With regards to material selection, the large energy difference between X and Γ valleys in the bandgap of AlAsSb may weaken the QD to E_C intraband transition strength. The quaternary $In_xAl_{1-x}As_ySb_{1-y}$ is lattice matched to InP when alloying between the two lattice matched alloys of InAlAs and AlAsSb leading to the notation $(In_{0.52}Al_{0.48}As)_x(AlAs_{0.56}Sb_{0.44})_{1-x}$ for a series of lattice matched InAlAsSb alloys. These quaternary alloys are difficult to grow, but can be used to increase the difference in energy between direct and indirect bandgaps, or at high enough $In_{0.52}Al_{0.48}As$, select a direct bandgap host material for InAs QDs [72][73]. MOCVD growth of InAlAsSb has been demonstrated [74] by our research group, but much more work needs to go into developing finer control over composition and doping before it is ready for incorporation into a solar cell.

6.2 Development of optimized QDSCs for multijunction PV

While the GaAs subcell in the Ge-based design was the EoL J_{SC} limiting subcell in the upright 3J device, the InGaAs subcell strongly limits J_{SC} at EoL in IMM devices[28] which presents the potential for an ancillary benefit to adding QDs to the GaAs subcell. QDs behave as strong radiative recombination centers and Chapter 2.6 shows demonstration of previous work on radiation tolerance of QDSCs. InAs/GaAs QDs have also been utilized as a laser material grown on Si, where lasing can occur in spite of high threading dislocation densities. We posit that QDs may enable the possibility of enhancing luminescent coupling between middle and bottom subcells both at beginning and end of life after radiation exposure without causing a significant degradation in electrical properties in the GaAs subcell at beginning of life. Since the bottom subcell in the IMM becomes heavily current limiting after exposure to high energy radiation, a first-order measurement can be performed by comparing pre and post-exposure AM0 IV measurements and comparing the resulting measured J_{SC}. However, there are some potential sources for error in this method because the RIT solar simulator has two independently controllable zones and the spectrum is IR rich, which could mask some of the InGaAs subcell degradation at standard EoL particle fluences. More precise calibration can be achieved by using three distinct color LEDs to separately illuminate each junction.

By illuminating two junctions at a time via LEDs and taking an IV measurement, it is possible to measure the sum of the shunt current and photogenerated current from luminescent coupling through the third junction. Shunt resistance is often rejected because it is assumed to be high [22][75][76], but this assumption may not be accurate after radiation exposure. The slope of the IV curve around the origin should provide an approximation of the shunt resistance of the current limiting subcell while total device shunt resistance can be approximated with a dark IV measurement.

IV characterization via electroluminescence has previously been used to characterize subcell open circuit voltage degradation due to radiation exposure in triple junction solar cells in Hoheisel at el. [77], but never in QDSC containing IMM solar cells. Doing

so is necessary for complete characterization of the devices presented in this work for two reasons. First, both sets of QDSCs presented in this chapter exhibited a diode ideality factor closer to n=1 than the respective control cells suggesting that they suppress nonradiative SCR recombination.

6.3 Modeling of Effects of Using Polycrystalline Substrates for Low Cost III-V Photovoltaics

This work focused on nucleation and growth on large-grain, highly polished polycrystalline wafers which had comparable RMS roughness to the crystalline wafers. A second thrust of this project, which is not included in my thesis is to recrystallize Ge substrates using various thermal processes, some of which involve alloying Ge with metals and may not result in atomically smooth surfaces. Substrate preparation is a major cost in processes like ELO mentioned in the Introduction and would ideally be omitted in the process of growing a solar cell on a recrystallized Ge template. I would like to assess the impact of surface roughness by chemically roughening GaAs substrates prior to growth. Taking Figure 5.5, substrate roughness could be seen as a third dimension to the contour plot and it is an area where little work has been done previously.

This study also contains very few data points on the impact of grain size on device performance due to the dearth of commercially available polycrystalline substrates. I have two proposed methods of rectifying this shortcoming. First, Elisabeth McClure, a colleague at RIT is working to recrystallize Ge on arbitrary substrates. Once we have achieved some degree of crystallinity, we will polish and grow a solar cell on one of those virtual substrates in order to add further datapoints to the contour plot. Second, other polycrystalline material systems have been studied for photovoltaics, particularly II-VI materials such as CdTe as well as the group IV poly-Si. I would like to reach out to potential collaboration partners and extend this modeling work across multiple material systems.

Bibliography

[1] John Perlin. *From Space to Earth: The Story of Solar Electricity*. EarthScan, 1999.

[2] B. Brar, G.J. Sullivan, and P.M. Asbeck. Herb's bipolar transistors. *IEEE Transactions on Electron Devices*, 48(11):2473–2476, November 2001.

[3] Z.S. Bittner, R.B. Laghumavarapu, S Hellstroem, D.L. Huffaker, B Liang, and S.M. Hubbard. Experimental examination of an InAs/GaAs(Sb)/AlAsSb quantum dot approach to the intermediate band solar cell. In *Proceedings of 40th IEEE Photovoltaic Specialists Conference*, Denver, CO, June 2014. IEEE.

[4] Hans J. Queisser and William Shockley. Detailed balance limit of efficiency of p-n junction solar cells. *J. Appl. Phys.*, 32(3):510–519, 1961.

[5] Louise Hirst and Nicholas Ekins-Daukes. Quantifying intrinsic loss mechanisms in solar cells: Why is power efficiency fundamentally limited? In *Next Generation (Nano) Photonic and Cell Technologies for Solar Energy Conversion*, 2010.

[6] H.J. Hovel and J.M. Woodall. Theoretical and experimental evaluations of gaalas - gaas solar cells. In *Proceedings of the IEEE Photovoltaic Specialists Conference*, 1973.

[7] Uwe Rau. Reciprocity relation between photovoltaic quantum efficiency and electroluminescent emission of solar cells. *Physical Review B*, 76(8):085303, August 2007.

[8] R. R. King, D. Bhusari, A. Boca, D. Larrabee, X.-Q. Liu, W. Hong, C. M. Fetzer, D. C. Law, and N. H. Karam. Band gap-voltage offset and energy production in next-generation multijunction solar cells. *Prog. Photovoltaics Res. Appl.*, 19(7):797–812, Nov 2011.

[9] R.E. Welser, O.A. Laboutin, M. Chaplin, and V Un. Reducing Non-Radiative and radiative recombination in InGaAs quantum well solar cells. In *Proceedings of the 37th IEEE PVSC*, Seattle, WA, 2011.

[10] M. Wolf. Limitations and Possibilities for Improvement of Photovoltaic Solar Energy Converters: Part I: Considerations for Earth's Surface Operation. *Proceedings of the IRE*, 48(7):1246–1263, July 1960.

[11] G Güttler and H. J Queisser. Impurity photovoltaic effect in silicon. *Energy Convers.*, 10(2):51–55, Apr 1970.

[12] Antonio Luque and Antonio Marti. Increasing the efficiency of ideal solar cells by photon induced transitions at intermediate levels. *Phys. Rev. Lett.*, 78(26):5014–5017, June 1997.

[13] Antonio Luque, Antonio Martí, Elisa Antolín, and César Tablero. Intermediate bands versus levels in non-radiative recombination. *Phys. B Condens. Matter*, 382(12):320–327, Jun 2006.

[14] A. P Alivisatos. Semiconductor Clusters, Nanocrystals, and Quantum Dots. *Science*, 271(5251):933–937, February 1996.

[15] A. Marti, L. Cuadra, and A. Luque. Quantum dot intermediate band solar cell. In *Conference Record of the Twenty-Eighth IEEE Photovoltaic Specialists Conference, 2000*, pages 940–943, 2000.

[16] J. M. Moison, F. Houzay, F. Barthe, L. Leprince, E. Andre, and O. Vatel. Selforganized growth of regular nanometerscale InAs dots on GaAs. *Applied Physics Letters*, 64(2):196–198, January 1994.

[17] Yoshitaka Okada, Takayuki Morioka, Katsuhisa Yoshida, Ryuji Oshima, Yasushi Shoji, Tomoya Inoue, and Takashi Kita. Increase in photocurrent by optical transitions via intermediate quantum states in direct-doped InAs/GaNAs strain-compensated quantum dot solar cell. *Journal of Applied Physics*, 109(2):024301, January 2011.

[18] S.J. Polly, D.V. Forbes, K. Driscoll, S. Hellstrom, and S.M. Hubbard. Delta-doping effects on quantum-dot solar cells. *IEEE Journal of Photovoltaics*, 4(4):1079–1085, July 2014.

[19] S.M. Hubbard et al. Effect of strain compensation on quantum dot enhanced gaas solar cells. *Applied Physics Letters*, 92, 2008.

[20] Christopher G. Bailey, David V. Forbes, Ryne P. Raffaelle, and Seth M. Hubbard. Near 1 v open circuit voltage InAs/GaAs quantum dot solar cells. *Applied Physics Letters*, 98:163105, 2011.

[21] E. Antolín, A. Marti, C. R. Stanley, C. D. Farmer, E. Cánovas, N. López, P. G. Linares, and A. Luque. Low temperature characterization of the photocurrent produced by two-photon transitions in a quantum dot intermediate band solar cell. *Thin Solid Films*, 516(20):6919–6923, August 2008.

[22] Myles A. Steiner and John F. Geisz. Non-linear luminescent coupling in series-connected multijunction solar cells. *Applied Physics Letters*, 100(25):251106, Jun 2012.

[23] J. F. Geisz, Sarah Kurtz, M. W. Wanlass, J. S. Ward, A. Duda, D. J. Friedman, J. M. Olson, W. E. McMahon, T. E. Moriarty, and J. T. Kiehl. High-efficiency GaInPGaAsInGaAs triple-junction solar cells grown inverted with a metamorphic bottom junction. *Applied Physics Letters*, 91(2):023502, July 2007.

[24] Rao Tatavarti, G. Hillier, A. Dzankovic, G. Martin, F. Tuminello, R. Navaratnarajah, G. Du, D.P. Vu, and N. Pan. Lightweight, low cost GaAs solar cells on 4 inch epitaxial liftoff (ELO) wafers. In *33rd IEEE Photovoltaic Specialists Conference, 2008. PVSC '08*, pages 1–4, May 2008.

[25] National Aeronautics and Space Administration, Washington, DC 20546. *Mitigating In-Spae Charging Effects-A Guideline*, March 2009.

[26] Shin-ichiro Sato, Takeshi Ohshima, and Mitsuru Imaizumi. Modeling of degradation behavior of InGaP/GaAs/Ge triple-junction space solar cell exposed to charged particles. *J. Appl. Phys.*, 105(4):044504, Feb 2009.

[27] Cory Cress. *Effects of Ionizing Radiation on Nanomaterials and III-V Semiconductor Devices*. PhD thesis, Rochester Institute of Technology, 2008.

[28] P. Patel, D. Aiken, A. Boca, B. Cho, D. Chumney, M. B. Clevenger, A. Cornfeld, N. Fatemi, Y. Lin, J. McCarty, F. Newman, P. Sharps, J. Spann, M. Stan, J. Steinfeldt, C. Strautin, and T. Varghese. Experimental Results From Performance Improvement and Radiation Hardening of Inverted Metamorphic Multijunction Solar Cells. *IEEE J. Photovoltaics*, 2(3):377–381, Jul 2012.

[29] Cory D. Cress, Seth M. Hubbard, Brian J. Landi, Ryne P. Raffaelle, and David M. Wilt. Quantum dot solar cell tolerance to alpha-particle irradiation. *Applied Physics Letters*, 91(18):183108, October 2007.

[30] S.M. Hubbard, S.-I. Sato, K. Schmieder, W. Strong, D. Forbes, C.G. Bailey, R. Hoheisel, and R.J. Walters. Impact of nanostructures and radiation environment on defect levels in III #x2013;v solar cells. In *Photovoltaic Specialist Conference (PVSC), 2014 IEEE 40th*, pages 1045–1050, June 2014.

[31] C. Kerestes, C.D. Cress, B.C. Richards, D.V. Forbes, Yong Lin, Z. Bittner, S.J. Polly, P. Sharps, and S.M. Hubbard. Strain effects on radiation tolerance of triple-junction solar cells with InAs quantum dots in the GaAs junction. *IEEE Journal of Photovoltaics*, 4(1):224–232, January 2014.

[32] Tingyi Gu, Mohamed A. El-Emawy, Kai Yang, Andreas Stintz, and Luke F. Lester. Resistance to edge recombination in GaAs-based dots-in-a-well solar cells. *Applied Physics Letters*, 95(26):261106, December 2009.

[33] Mathieu César, Youqi Ke, Wei Ji, Hong Guo, and Zetian Mi. Band gap of in$_x$ga$_{1x}$n: A first principles analysis. *Applied Physics Letters*, 98(20):202107, May 2011.

[34] Arlinda Hill. *Growth, Characterization, and Thermodynamics of III-Nitride Semiconductors*. PhD thesis, Arizona State University, 2011.

[35] Ting Wang, Huiyun Liu, Andrew Lee, Francesca Pozzi, and Alwyn Seeds. 1.3-m inas/gaas quantum-dot lasers monolithically grown on si substrates. *Optics Express*, 19(12):11381, June 2011.

[36] A. Marti, N. Lopez, E. Antolín, E. Cánovas, C. Stanley, C. Farmer, L. Cuadra, and A. Luque. Novel semiconductor solar cell structures: The quantum dot intermediate band solar cell. *Thin Solid Films*, 511–512:638–644, July 2006.

[37] Yushuai Dai, S.J. Polly, S Hellstroem, D.V. Forbes, and S.M. Hubbard. Electric field effect on carrier escape from InAs/GaAs quantum dots solar cells. In *Proceedings of 40th IEEE Photovoltaic Specialists Conference*, Denver, CO, June 2014. IEEE.

[38] S. Hellstroem and S.M. Hubbard. Drift-diffusion simulations of InAs/AlAsSb quantum dot intermediate band solar cells. In *Proceedings of 40th IEEE Photovoltaic Specialists Conference*, Denver, CO, June 2014. IEEE.

[39] Paul J. Simmonds, Ramesh Babu Laghumavarapu, Meng Sun, Andrew Lin, Charles J. Reyner, Baolai Liang, and Diana L. Huffaker. Structural and optical properties of InAs/AlAsSb quantum dots with GaAs(Sb) cladding layers. *Applied Physics Letters*, 100(24):243108, June 2012.

[40] Marina S. Leite, Robyn L. Woo, William D. Hong, Daniel C. Law, and Harry A. Atwater. Wide-band-gap InAlAs solar cell for an alternative multijunction approach. *Applied Physics Letters*, 98(9):093502, February 2011.

[41] H. Schneider and K. v. Klitzing. Thermionic emission and gaussian transport of holes in a GaAs/AlxGa1-xAs multiple-quantum-well structure. *Physical Review B*, 38(9):6160–6165, September 1988.

[42] D. Fuertes Marrón, E. Cánovas, I. Artacho, C. R. Stanley, M. Steer, T. Kaizu, Y. Shoji, N. Ahsan, Y. Okada, E. Barrigón, I. Rey-Stolle, C. Algora, A. Marti, and A. Luque. Application of photoreflectance to advanced multilayer structures for photovoltaics. *Materials Science and Engineering: B*, 178(9):599–608, May 2013.

[43] Y. S. Huang, H. Qiang, Fred H. Pollak, Johnson Lee, and B. Elman. Electroreflectance study of a symmetrically coupled GaAs/Ga0.77Al0.23As double quantum well system. *Journal of Applied Physics*, 70(7):3808, 1991.

[44] B.L. Smith, S.D. Hellstroem, G.T. Nelson, Z.S. Bittner, M.A. Slocum, D.V. Forbes, and S.M. Hubbard. Characterization of InAlAs solar cells grown by MOVPE. In *Photovoltaic Specialist Conference (PVSC), 2014 IEEE 40th*, pages 1180–1185, June 2014.

[45] J.M. Woodall and H.J. Hovel. Theoretical and experimental evaluation of GaAlAs-GaAs solar cells. In *Proceedings of the 10th IEEE PVSC*, 1973.

[46] S.M. Hubbard, C.G. Bailey, R. Aguinaldo, S. Polly, D.V. Forbes, and R.P. Raffaelle. Characterization of quantum dot enhanced solar cells for concentrator photovoltaics. In *Photovoltaic Specialists Conference (PVSC), 2009 34th IEEE*, pages 000090 – 000095, June 2009.

[47] Seth M Hubbard, Christopher Bailey, Stephen Polly, Cory Cress, John Andersen, David Forbes, and Ryne Raffaelle. Nanostructured photovoltaics for space power. *Journal of Nanophotonics*, 3(1):031880–031880–16, October 2009.

[48] A. Marti, N. Lopez, E. Antolin, E. Canovas, C. Stanley, C. Farmer, L. Cuadra, and A. Luque. Novel semiconductor solar cell structures: The quantum dot intermediate band solar cell. *Thin Solid Films*, 511–512(0):638–644, July 2006.

[49] Nasser H Karam, Richard R King, Moran Haddad, James H Ermer, Hojun Yoon, Hector L Cotal, Rengarajan Sudharsanan, Jack W Eldredge, Kenneth Edmondson, David E Joslin, Dimitri D Krut, Mark Takahashi, Warren Nishikawa, Mark Gillanders, Jennifer Granata, Peter Hebert, B.Terence Cavicchi, and David R Lillington. Recent developments in high-efficiency ga0.5in0.5p/gaas/ge dual- and triple-junction solar cells: steps to next-generation pv cells. *Solar Energy Materials and Solar Cells*, 66(1–4):453–466, February 2001.

[50] A.S Gudovskikh, K.S. Zelentsov, N.A. Kalyuzhnyy, V.M. Lantratov, and S.A. Mintairov. Anisotype GaAs based heterojunctions for III-V multijunction solar cells. In *Proceedings of the 25th European Photovoltaic Solar Energy Conference*, 2010.

[51] S. M Hubbard, C. D Cress, C. G Bailey, R. P Raffaelle, S. G Bailey, and D. M Wilt. Effect of strain compensation on quantum dot enhanced GaAs solar cells. *Applied Physics Letters*, 92(12):123512–123512–3, March 2008.

[52] Christopher G. Bailey, David V. Forbes, Ryne P. Raffaelle, and Seth M. Hubbard. Near 1 v open circuit voltage InAs/GaAs quantum dot solar cells. *Applied Physics Letters*, 98:163105, 2011.

[53] C Kerestes, S. J. Polly, D.V. Forbes, C.G. Bailey, and S.M. Hubbard. Investigation of quantum dot enhanced triple junction solar cells. In *Proceedings of the 37th IEEE PVSC*, 2011.

[54] Hao Feng Lu, Lan Fu, Greg Jolley, Hark Hoe Tan, Sudersena Rao Tatavarti, and Chennupati Jagadish. Temperature dependence of dark current properties of InGaAs/GaAs quantum dot solar cells. *Applied Physics Letters*, 98:183509, 2011.

[55] J. Novak, S. Hasenohrl, I. Vavra, and M. Kucera. Influence of surface strain on the MOVPE growth of InGaP epitaxial layers. *Applied Physics A*, 87:511–516, February 2007.

[56] Yu-Li Tsai, Ray-Hua Horng, Ming-Chun Tseng, Chia-hao Kuo, Po-Liang Liu, Dong-Sing Wuu, and Der-Yuh Lin. Phase separation phenomenon in MOCVD-grown GaInP epitaxial layers. *Journal of Crystal Growth*, 311(11):3220–3224, May 2009.

[57] Mitchell F. Bennett, Zachary S. Bittner, David V. Forbes, Sudersena Rao Tatavarti, S. Phillip Ahrenkiel, Andree Wibowo, Noren Pan, Kevin Chern, and Seth M. Hubbard. Epitaxial lift-off of quantum dot enhanced GaAs single junction solar cells. *Applied Physics Letters*, 103(21):213902, November 2013.

[58] Sebastian Roensch, Raymond Hoheisel, Frank Dimroth, and Andreas W. Bett. Subcell I-V characteristic analysis of GaInP/GaInAs/Ge solar cells using electroluminescence measurements. *Applied Physics Letters*, 98(25):251113, June 2011.

[59] Roger E Welser, Ashok Sood, Jay S Lewis, Nibir K Dhar, and Roy L Peters. Development of iii-v quantum well and quantum dot solar cells. 9:29–44, Jan 2016.

[60] M. A. Slocum, G. Nelson, S. Hellstroem, B. Smith, A. Wibowo, R. Tatavarti, and S. M. Hubbard. Growth of inas quantum dots in a metamorphic ingaas bottom cell of an inverse metamorphic solar cell. In *2016 IEEE 43rd Photovoltaic Specialists Conference (PVSC)*, pages 2111–2114, Jun 2016.

[61] S.J. Polly, C.R. Plourde, Christopher G. Bailey, C. Leitz, C. Vineis, M.P. Brindak, D.V. Forbes, J.S. McNatt, S.M. Hubbard, and R.P. Raffaelle. Thin film III-v solar cells on mo foil. In *2009 34th IEEE Photovoltaic Specialists Conference (PVSC)*, pages 001377–001380, June 2009.

[62] Yoshiro Ohmachi, Takashi Nishioka, and Yukinobu Shinoda. Zonemelting germanium film crystallization with tungsten encapsulation. *Applied Physics Letters*, 43(10):971–973, November 1983.

[63] Michael G. Mauk, Jeremy R. Balliet, and Bryan W. Feyock. Large-grain (>1-mm), recrystallized germanium films on alumina, fused silica, oxide-coated silicon substrates for IIIv solar cell applications. *Journal of Crystal Growth*, 250(12):50–56, March 2003.

[64] R. Venkatasubramanian, B.C. O'Quinn, E. Siivola, B. Keyes, and R. Ahrenkiel. 20 (AM1.5) efficiency GaAs solar cells on sub-mm grain-size poly-ge and its transition to low-cost substrates. In *, Conference Record of the Twenty-Sixth IEEE Photovoltaic Specialists Conference, 1997*, pages 811–814, September 1997.

[65] Sheila G. Bailey, D.M. Wilt, J.S. McNatt, Les Fritzenmeier, S.M. Hubbard, Christopher G. Bailey, and Ryne P. Raffaelle. Thin film poly III-v space solar cells. In *33rd IEEE Photovoltaic Specialists Conference, 2008. PVSC '08*, pages 1–5, May 2008.

[66] Rehan Kapadia, Zhibin Yu, Mark Hettick, Jingsan Xu, Maxwell S. Zheng, Cheng-Ying Chen, Arunima D. Balan, Daryl C. Chrzan, and Ali Javey. Deterministic nucleation of InP on metal foils with the thin-film vaporliquidsolid growth mode. *Chemistry of Materials*, 26(3):1340–1344, February 2014.

[67] D. M. Wilt, M. A. Smith, W. Maurer, D. Scheiman, and P. P. Jenkins. GaAs Photovoltaics on Polycrystalline Ge Substrates. volume 2, pages 1891–1894, May 2006.

[68] Masafumi Yamaguchi and Yoshio Itoh. Efficiency considerations for polycrystalline GaAs thinfilm solar cells. *Journal of Applied Physics*, 60(1):413–417, July 1986.

[69] C.L. Andre, A. Khan, M. Gonzalez, M.K. Hudait, E.A. Fitzgerald, J.A. Carlin, M.T. Currie, C.W. Leitz, T.A. Langdo, E.B. Clark, D.M. Wilt, and S.A. Ringel. Impact of threading dislocations on both n/p and p/n single junction GaAs cells grown on Ge/SiGe/Si substrates. In *Conference Record of the Twenty-Ninth IEEE Photovoltaic Specialists Conference, 2002*, pages 1043–1046, May 2002.

[70] Pablo G. Linares, Antonio Martí, Elisa Antolín, Corrie D. Farmer, Íñigo Ramiro, Colin R. Stanley, and Antonio Luque. Voltage recovery in intermediate band solar cells. *Solar Energy Materials and Solar Cells*, 98:240–244, March 2012.

[71] Greg Jolley, Lan Fu, Hao Feng Lu, Hark Hoe Tan, and Chennupati Jagadish. The role of intersubband optical transitions on the electrical properties of InGaAs/GaAs quantum dot solar cells. *Progress in Photovoltaics: Research and Applications*, 21(4):736–746, June 2013.

[72] M. P. Lumb, M. González, J. Abell, K. J. Schmieder, J. G. Tischler, D. A. Scheiman, M. K. Yakes, I. Vurgaftman, J. R. Meyer, and R. J. Walters. Characterization, modeling and analysis of InAlAsSb Schottky barrier solar cells grown on InP. pages 0243–0246, Jun 2014.

[73] Louise C. Hirst, Matthew P. Lumb, Josh Abell, Chase T. Ellis, Joseph G. Tischler,

Igor Vurgaftman, Jerry R. Meyer, Robert J. Walters, and María González. Spatially indirect radiative recombination in InAlAsSb grown lattice-matched to InP by molecular beam epitaxy. *J. Appl. Phys.*, 117(21):215704, Jun 2015.

[74] G.T. Nelson, Z.S. Bittner, B. Smith, D.V. Forbes, and S.M. Hubbard. Study of deep levels in InAlAsSb grown via organometallic vapor phase epitaxy. pages 1168–1173, Jun 2014.

[75] D. J. Friedman, J. F. Geisz, and M. A. Steiner. Analysis of Multijunction Solar Cell Current-Voltage Characteristics in the Presence of Luminescent Coupling. *IEEE Journal of Photovoltaics*, 3(4):1429–1436, October 2013.

[76] Matthew P. Lumb, Myles A. Steiner, John F. Geisz, and Robert J. Walters. Incorporating photon recycling into the analytical drift-diffusion model of high efficiency solar cells. *J. Appl. Phys.*, 116(19):194504, Nov 2014.

[77] R. Hoheisel, D. Scheiman, S. Messenger, P. Jenkins, and R. Walters. Detailed Characterization of the Radiation Response of Multijunction Solar Cells Using Electroluminescence Measurements. *IEEE Trans. Nucl. Sci.*, 62(6):2894–2898, Dec 2015.